Terms and Conditions of Use of Digitised Theses from Trinity College Library Dublin

Copyright statement

All material supplied by Trinity College Library is protected by copyright (under the Copyright and Related Rights Act, 2000 as amended) and other relevant Intellectual Property Rights. By accessing and using a Digitised Thesis from Trinity College Library you acknowledge that all Intellectual Property Rights in any Works supplied are the sole and exclusive property of the copyright and/or other IPR holder. Specific copyright holders may not be explicitly identified. Use of materials from other sources within a thesis should not be construed as a claim over them.

A non-exclusive, non-transferable licence is hereby granted to those using or reproducing, in whole or in part, the material for valid purposes, providing the copyright owners are acknowledged using the normal conventions. Where specific permission to use material is required, this is identified and such permission must be sought from the copyright holder or agency cited.

Liability statement

By using a Digitised Thesis, I accept that Trinity College Dublin bears no legal responsibility for the accuracy, legality or comprehensiveness of materials contained within the thesis, and that Trinity College Dublin accepts no liability for indirect, consequential, or incidental, damages or losses arising from use of the thesis for whatever reason. Information located in a thesis may be subject to specific use constraints, details of which may not be explicitly described. It is the responsibility of potential and actual users to be aware of such constraints and to abide by them. By making use of material from a digitised thesis, you accept these copyright and disclaimer provisions. Where it is brought to the attention of Trinity College Library that there may be a breach of copyright or other restraint, it is the policy to withdraw or take down access to a thesis while the issue is being resolved.

Access Agreement

By using a Digitised Thesis from Trinity College Library you are bound by the following Terms & Conditions. Please read them carefully.

I have read and I understand the following statement: All material supplied via a Digitised Thesis from Trinity College Library is protected by copyright and other intellectual property rights, and duplication or sale of all or part of any of a thesis is not permitted, except that material may be duplicated by you for your research use or for educational purposes in electronic or print form providing the copyright owners are acknowledged using the normal conventions. You must obtain permission for any other use. Electronic or print copies may not be offered, whether for sale or otherwise to anyone. This copy has been supplied on the understanding that it is copyright material and that no quotation from the thesis may be published without proper acknowledgement.

The physico-chemical properties of fullerenes and porphyrin derivatives deposited on conducting surfaces
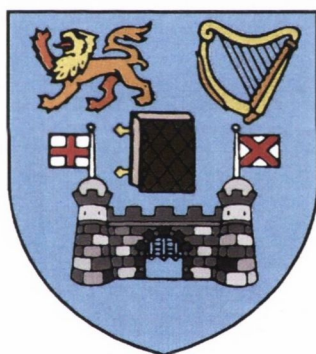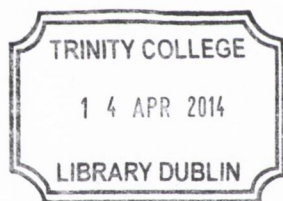
Barry E Murphy

School of Physics

Trinity College Dublin

A thesis submitted for the degree of

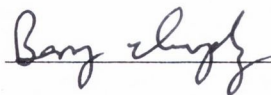*Doctor of Philosophy*

February 2014

Declaration

I declare that this thesis has not been submitted as an exercise for a degree at this or any other university and apart from the advice, assistance and joint effort acknowledged and mentioned in the text, it is entirely my own work.

I agree to deposit this thesis in the University's open access institutional repository or allow the library to do so on my behalf, subject to Irish Copyright Legislation and Trinity College Library conditions of use and acknowledgement.

Barry Murphy

February 24, 2014

Summary

In this thesis, three organic molecules are examined on three distinct surfaces by a variety of surface science techniques, foremost among them being scanning tunneling microscopy (STM).

When deposited on the $WO_2/W(110)$ surface, C_{60} fullerenes self-assemble into islands which grow from the substrate's inner step edges, forming a close-packed monolayer.

At some bias voltages, chains of molecules sit topologically lower in height than others, because they lie in the grooves between the WO_2 nanorows. When the sample is imaged at room temperature, all C_{60} are spinning too fast for the STM to resolve, and so appear as featureless spheres. However, when cooled to $78\,K$, the molecules' motion is frozen and their inner orbital structure can be seen.

Depending on the rate of cooling, an orbital-ordered monolayer (slow cooling), or a glassy monolayer with random molecular orientations (fast quenching) can be achieved.

During cooling, two phase transitions are observed. As the temperature is decreased, a structural transition occurs at $259\,K$ when some molecules begin to freeze, and a kinetic transition is observed at $220\,K$ when all molecular motion has stopped.

Between the two transitions, several dynamic behaviours are observed. Some molecules which spin like a top appear as a ring with either a dark centre or a protrusion. Others change their apparent height over time, which is attributed to them gaining and losing an electron, and thus changing their density of states and hence their conductance, as measured by STM. This charging and discharging is accompanied by the molecules' rotation on the

surface, as they interact with their neighbours and the underlying oxide substrate. The observations obtained by STM are supported by DFT calculations.

The second molecule examined was nickel diphenyl-porphyrin (NiDPP) deposited on the Ag(111) and Ag/Si(111)-$\sqrt{3} \times \sqrt{3}$ R30° surfaces. On the inert Ag(111) surface, NiDPP self-assembles into a single close-packed domain, as shown by STM and low energy electron diffraction (LEED). The molecules exhibit a tilted-row structure with a slightly oblique unit cell, with one diagonal of the unit cell aligned with the step edges of the underlying substrate.

In contrast, on the Ag/Si(111)-$\sqrt{3} \times \sqrt{3}$ R30° surface the NiDPP molecules adopt one of three equivalent orientations, dictated by the surface symmetry. The molecules pack closer together, and this strain is accommodated by a stronger interaction with the more-reactive surface. Three domains rotated by 120° to one another are observed to be randomly distributed over the surface due to nucleation from molecules adopting one of the three orientations upon contact with the surface.

Finally, another porphyrin, manganese-chloride tetraphenyl-porphyrin, or MnClTPP, has also been studied on the Ag(111) surface. Upon deposition, the molecule adopts a saddle conformation and the axial chloride ligand points out into the vacuum. The monolayer assembles into the typical square close-packed geometry commonly observed for tetraphenyl-porphyrins.

When it is annealed up to 510 K, the Cl-ligand is removed, but the Mn(III) oxidation state is stabilised through interaction with the substrate, as observed by X-ray absorption spectroscopy (XAS).

Exposure to molecular oxygen oxidises the central Mn ion to the Mn(IV) state and the oxygen molecule binds to the centre as a bidentate peroxide ligand. This MnO_2TPP state is stable up to 445 K, whereupon the O_2 is lost from the molecule, and the Mn ion is reduced back to the Mn(III) state. From core-level X-ray photoelectron spectra (XPS) taken from the Cl 2p and O 1s levels, the activation energies for Cl and O_2 removal were found to be $\Delta E_{Cl} = 0.35 \pm 0.02\,\text{eV}$ and $\Delta E_{O_2} = 0.26 \pm 0.03\,\text{eV}$, respectively.

Acknowledgements

As with any undertaking that takes four years to complete, there are many people I would like to thank for their help during my studies. Firstly, I would like to acknowledge my supervisor, Prof Igor Shvets, for giving me the opportunity to join his group and allowing me to investigate these molecules despite their relative distance from his core topic. I have learned a lot from him, and I hope that he has learned something from me in return.

I would especially like to thank my Postdoc "mentor," Dr Sergey Kransikov. Sergey basically taught me everything I know about surface science and organic macromolecules, and I would have been lost without his expertise. I wish him well in the UK and hope we can collaborate in the future. Another Sergey who was key to my studies was Dr Sergey Bozhko, whose tireless work and stimulating discussions were most illuminating.

Thank you to Dr Olaf Lübben, both for his time and effort in the lab, maintaining our cluster, and performing DFT simulations, and also for his company at lunchtimes in the Buttery. Although Dr Alexander Chaika has only been a member of the team for a short time, his input and advice have been invaluable, and I am very grateful to him. I am also grateful to Dr Tony Cafolla, both for his many insights into organic molecules, and for his experimental work in measuring the X-ray spectra of MnClTPP with Dr Krasnikov. Thanks also to the rest of the Applied Physics Group, both past and present members.

Without my other "physics" friends, Steve, Tom, Mike, Cathal and Brendan, to nerd out with and keep me sane, I don't think I would have made it to the end. When I needed a dose of "normality" my friends from my home town of Wexford were always there for a coffee or a drink, and if I needed to

be brought right back to reality, my Scouts and the other Leaders of the 13th would make sure I didn't get too big for my boots, which we all need now and again! Thanks also to my long-suffering flatmate Dr Eric Lucking for putting up with my messiness for the past four years, and to Dr Genevieve Murray, for her advice, support and many games of Rummikub!

One of the most important people in my life for the last (almost) 3 years has been my girlfriend, Louise. She has always listened to my complaints and been the voice of reason when everything got too much for me. I'm not sure I can pay you back, but I'd like to try.

At last I get to my family. My brother Brian and his lovely wife Rhatia have been so good to me, taking me into their home, letting my play with their dog, introducing me to their friends; I don't know where I would be without them but I know I wouldn't be as happy.

Unfortunately my Mum didn't get to see me complete my PhD, but I know how proud she was of me, and that she would be telling everyone she met about it.

Finally, I am so grateful to my Dad. Without his unfailing support, belief and wisdom throughout my life, I would not be the man I am today.

I dedicate this thesis to my late mother, Bernadette, and my father, Nick. Without their support, pride and belief I would never have gotten this far.

List of publications

1. *Growth and ordering of Ni(II) diphenylporphyrin monolayers on Ag(111) and Ag/Si(111) studied by STM and LEED*

   Barry E. Murphy, Sergey A. Krasnikov, Attilio A. Cafolla, Natalia N. Sergeeva, Nikolai A. Vinogradov, John P. Beggan, Olaf Lübben, Mathias O. Senge, and Igor V. Shvets

   Journal of Physics: Condensed Matter **24** (2012) 045005

2. *Self-assembly and ordering of C_{60} on the $WO_2/W(110)$ surface*

   Sergey A. Krasnikov, Sergey I. Bozhko, Kevin Radican, Olaf Lübben, **Barry E. Murphy**, Sundar-Raja Vadapoo, Han-Chun Wu, Mohamed Abid, Valery N. Semenov, and Igor V. Shvets

   Nano Research **4** (2011) 194–203

3. *Rotational transitions in a C_{60} monolayer on the $WO_2/W(110)$ surface*

   Sergey I. Bozhko, Sergey A. Krasnikov, Olaf Lübben, **Barry E. Murphy**, Kevin Radican, Valery N. Semenov, Han Chun Wu, Brendan Bulfin, and Igor V. Shvets

   Physical Review B **84** (2011) 195412

4. *Correlation between charge-transfer and rotation of C_{60} on $WO_2/W(110)$*

   Sergey I. Bozhko, Sergey A. Krasnikov, Olaf Lübben, **Barry E. Murphy**, Kevin Radican, Valery N. Semenov, Han Chun Wu, Egor A. Levchenko, Alexander N. Chaika, Natalia N. Sergeeva, and Igor V. Shvets

   Nanoscale **5** (2013) 3380–3386

5. *Modifying the axial ligand attached to a planar macrocycle: MnCl porphyrins on Ag(111)*

   Barry E. Murphy, Sergey A. Krasnikov, Natalia N. Sergeeva, Attilio A. Cafolla, Alexei B. Preobrajenski, Olaf Lübben, Alexander N. Chaika, and Igor V. Shvets

   In preparation (2014)

6. *Fe Nanoclusters on the Ge(001) Surface Studied by Scanning Tunneling Microscopy, Density Functional Theory Calculations and X-Ray Magnetic Circular Dichroism*

   Olaf Lübben, Sergey A. Krasnikov, Alexei B. Preobrajenski, **Barry E. Murphy**, and Igor V. Shvets

   Nano Research **4** (2011) 971–978

7. *Self-assembly of Fe nanocluster arrays on templated surfaces*

   Olaf Lübben, Sergey A. Krasnikov, Alexei B. Preobrajenski, **Barry E. Murphy**, Sergey I. Bozhko, Sunil K. Arora, and Igor V. Shvets

   Journal of Applied Physics **111** (2012) 07B515

8. *Finite element method simulations of heat flow in fixed bed solar water splitting redox reactors*

   Brendan Bulfin, **Barry E. Murphy**, Olaf Lübben, Sergey A. Krasnikov, and Igor V. Shvets

   International Journal of Hydrogen Energy **37**(13) (2012) 10028–10035

9. *Writing with atoms: Oxygen adatoms on the MoO$_2$/Mo(110) surface*

   Sergey A. Krasnikov, Olaf Lübben, **Barry E. Murphy**, Sergey I. Bozhko, Alexander N. Chaika, Natalia N. Sergeeva, Brendan Bulfin, and Igor V. Shvets

   Nano Research **6** (2013) 929–937

10. *Rotated domain network in millimeter-scale graphene synthesized on cubic-SiC(001)*

    Alexander N. Chaika, O. V. Molodtsova, Alexei A. Zakharov, Dimitri Marchenko, Jose Sánchez-Barriga, Alexei Varykhalov, S. V. Babekov, M. Portail, M. Zielinski, **Barry E. Murphy**, Sergey A. Krasnikov, Igor V. Shvets, and Victor Y. Aristov

    Accepted to Nanotechnology (2014)

11. *Atomically resolved STM imaging with a diamond tip: simulation and experiment*

    Victor Grushko, Olaf Lübben, Alexander N. Chaika, N. Novikov, E. Mitskevich, A. Chepugov, O. Lysenko, **Barry E. Murphy**, Sergey A.

Krasnikov, and Igor V. Shvets

Nanotechnology **25** (2014) 025706

12. ***An analytical model of CeO$_2$ oxidation and reduction***

Brendan Bulfin, Arran J. Lowe, Kevin A. Keogh, **Barry E. Murphy**, Olaf Lübben, Sergey A. Krasnikov, and Igor V. Shvets

Journal of Physical Chemistry C **46** (2013) 24129–24137

List of abstracts presented

1. *C_{60} monolayer on the tungsten oxide surface: from simple self-assembly to C_{60} quantum states*

   Barry E. Murphy*, Sergey A. Krasnikov, Sergey I. Bozhko, Kevin Radican, Olaf Lübben, Valery N. Semenov, Han-Chun Wu, and Igor V. Shvets

   18th Interdisciplinary Surface Science Conference (ISSC-18), Warwick, UK, April 2011

2. *Ni(II) Diphenylporphyrin Monolayers on Ag(111) and Ag/Si(111): the Effect of Surface Reactivity*

   Barry E. Murphy, Sergey A. Krasnikov, Attilio A. Cafolla, Natalia N. Sergeeva, Nikolay A. Vinogradov, John P. Beggan, Olaf Lübben*, Mathias O. Senge, and Igor V. Shvets

   16th International Conference on Solid Films and Surfaces (ICSFS-16), Genoa, Italy, July 2012

3. *Exploiting surface reactivity: Ni(II) diphenylporphyrin monolayers on Ag(111) and Ag/Si(111)*

   Barry E. Murphy*, Sergey A. Krasnikov, Attilio A. Cafolla, Natalia N. Sergeeva, Nikolay A. Vinogradov, John P. Beggan, Olaf Lübben, Mathias O. Senge, and Igor V. Shvets

   24th Conference of the EPS Condensed Matter Division (CMD-24, ECOSS-29), Edinburgh, Scotland, UK, September 2012

4. *Writing with Atoms: Oxygen Adatoms on the $MoO_2/Mo(110)$ Surface*

   Olaf Lübben, **Barry E. Murphy***, Sergey A. Krasnikov, Sergey I. Bozhko, and Igor V. Shvets

   24th Conference of the EPS Condensed Matter Division (CMD-24, ECOSS-29), Edinburgh, Scotland, UK, September 2012

5. *MnCl porphyrins on the Ag(111) surface: axial ligand transformation*

   Barry E. Murphy*, Sergey A. Krasnikov, Natalia N. Sergeeva, Attilio A. Cafolla, Alexei B. Preobrajenski, Olaf Lübben, Alexander N. Chaika, Mathias O. Senge, and Igor V. Shvets

   19th International Vacuum Congress (IVC-19), Paris, France, September 2013

6. *Electron orbital resolution in distance-dependent STM experiments with tungsten tips*

   Olaf Lübben*, Alexander N. Chaika, Sergei S. Nazin, Valerie N. Semenov, N. N. Orlova, E. Yu. Postnova, Sergey I. Bozhko, Sergey A. Krasnikov, **Barry E. Murphy**, Kevin Radican, and Igor V. Shvets

   19th International Vacuum Congress (IVC-19), Paris, France, September 2013

7. *Diamond-STM: Atomically resolved STM using a single-crystal conductive diamond tip*

Victor Grushko, Olaf Lübben, Alexander N. Chaika*, **Barry E. Murphy**, Igor V. Shvets, Sergey I. Bozhko, A. Chepugov, and O. Lysenko

International Conference on Diamond and Carbon Materials 2013 (DCM-13), Riva del Garda, Italy, September 2013

8. *Rotated domain network in millimeter-scale graphene layer synthesized on cubic-SiC(001)*

Alexander N. Chaika*, O. V. Molodtsova, Alexei A. Zakharov, Dimitri Marchenko, Jose Sánchez-Barriga, Alexei Varykhalov, S. V. Babekov, M. Portail, M. Zielinski, **Barry E. Murphy**, Sergey A. Krasnikov, Olaf Lübben, Igor V. Shvets, and Victor Y. Aristov

International Conference on Diamond and Carbon Materials 2013 (DCM-13), Riva del Garda, Italy, September 2013

---

*Presenting author

List of abbreviations

2D	-	two-dimensional
2D-FFT	-	two-dimensional fast Fourier transform
3D	-	three-dimensional
AES	-	Auger electron spectroscopy
BO	-	Born-Oppenheimer
C_{60}	-	Buckminster fullerene
CMA	-	cylindrical mirror analyser
Co-TBrPP	-	(5,10,15,20-tetrabromophenylporphyrinato)Co(II)
CYP	-	cytochrome P450
DFT	-	density functional theory
DOS	-	density of states
EXAFS	-	extended X-ray absorption fine structure
FCC	-	face-centred cubic
GGA	-	generalised gradient approximation
h	-	C_{60} facing a surface with a hexagon
h–h	-	C_{60} facing a surface with the bond between two hexagons
h–p	-	C_{60} facing a surface with the bond between a hexagon and a pentagon
H_2P	-	free-base porphine
H_2TPP	-	free-base tetraphenyl-porphyrin
HOMO	-	highest occupied molecular orbital
LDA	-	local density approximation

LEED	-	low energy electron diffraction
LUMO	-	lowest unoccupied molecular orbital
ML	-	monolayer
MnClTPP	-	(5,10,15,20-tetraphenylporphyrinato)Mn(III)Cl
MO	-	molecular orbital
NEXAFS	-	near-edge X-ray absorption fine structure
NiDPP	-	(5,15-diphenylporphyrinato)Ni(II)
NiP	-	Ni-porphine
NiTPP-dimer	-	5-((10,15,20-triphenylporphyrinato)Ni(II))$_2$ dimer
p	-	C_{60} facing a surface with a pentagon
PAW	-	projected augmented wave
PBE	-	Perdew-Burke-Ernzerhof
s	-	C_{60} facing a surface with a single atom
SNOM	-	scanning near-field optical microscopy
STM	-	scanning tunneling microscopy
T_0	-	Kauzmann temperature
T_C	-	critical temperature
T_g	-	kinetic glassy transition temperature
TPP	-	tetraphenyl-porphyrin
UHV	-	ultra-high vacuum
VASP	-	Vienna *ab initio* simulation package
vdW-DF	-	van der Waals density functional
VFT	-	Vogel-Fulcher-Tammann
XAFS	-	X-ray absorption fine structure

XANES	-	X-ray absorption near-edge structure
XAS	-	X-ray absorption spectroscopy
XPS	-	X-ray photoemssion spectroscopy

Contents

List of Figures

Chapter 1

Introduction

Understanding the mechanisms that control matter on the smallest level is one of the key goals of materials science. When deposited onto a surface, atoms and molecules arrange themselves into novel structures, often resulting in emergent behaviour and interesting phenomena.

This self-assembly is a fundamental topic of surface science and nanotechnology [1–20] and requires a broad understanding of the complex interplay between the adsorbates and the surfaces which support them. Organic molecules represent an interesting avenue for the study of self-assembly due to the myriad different species and activities available.

Three organic molecules will be examined in this thesis: the fullerene C_{60}; and two porphyrin derivatives, (5,15-diphenylporphyrinato)Ni(II), designated **NiDPP** for convenience, and (5,10,15,20-tetraphenylporphyrinato)-Mn(III)Cl, **MnClTPP**.

Fullerenes are a class of carbon allotropes consisting of sp^2-hybridised carbon atoms arranged in three-dimensional, closed-cage structures. The

fullerene family encompasses such exotic materials as the single atomic sheets of graphene, pseudo-one-dimensional carbon nanotubes and spherical C_{60} buckminsterfullerenes, from which the family derives its name. It is the last of these, C_{60}, which will be described in detail in this thesis.

Many potential applications of C_{60} fullerenes have been postulated, and they are the basis of active areas of research. When added to bulk hetero-junction solar cells as electron acceptors, in some cases they have been shown to increase efficiencies immensely [21], indicating that C_{60} may be very important for the future development of organic solar cells. C_{60} has also shown some promise as a future data storage medium [22], with precise, repeatable non-volatile storage possible with a data density approaching the theoretical limit of a single-molecular bit size.

However, even though many applications for C_{60} have been theorised since their discovery in 1985 [23], many open fundamental questions remain. When deposited onto metallic surfaces at room temperature, C_{60} molecules generally form close-packed islands, and start to nucleate at substrate step edges.

Thin C_{60} films on metal [18, 24–37] and semiconductor [22, 38–42] surfaces have been widely studied, however reports of their self-assembly on oxides are much more rare [43–45]. It is for this reason that the interaction between C_{60} and the oxide nanorows of $WO_2/W(110)$ is examined in this work.

Due to their spherical symmetry, C_{60} molecules have enough energy to freely rotate at room temperature. However during cooling, molecule–substrate interactions overcome the molecules' kinetic energy, resulting in two separate phase transitions. A number of different effects are observed, such

as spinning perpendicular to the surface, molecular charging and the eventual freezing in place of the C_{60} molecules' orientations.

The interaction between the molecules and substrate is dependent on the metal surface and can result in adsorbate-induced surface reconstruction, which can be accompanied by charge transfer between the surface and the molecules [25], however, in this thesis, no induced surface reconstructions are observed on the strained-commensurate WO_2/W(110) surface [46–48].
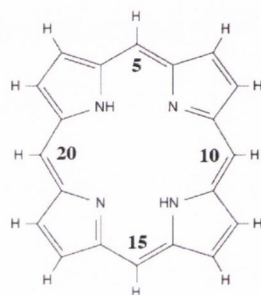
Figure 1.1: Chemical structure of the simplest porphyrin, Porphin, with numbers indicating the *meso*-positions

Porphyrins are another family of organic molecules. The simplest form, porphine, consists of an unsaturated macrocyclic carbon structure made up of four pyrrole rings and four C atoms in the meso positions, with two of the pyrrole rings' nitrogen atoms each bonded to a delocalised hydrogen atom, as shown in Figure 1.1. This simple structure forms the basis for many of the most important chemicals both in industry and the natural world. If the central hydrogen atoms are removed, the four nitrogen atoms can act as ligands for a transition metal ion. When an Fe(II) ion is added to the porphyrin, it becomes a heme, the metal complex which is the key component in the oxygen-storage capacity of red blood cells (haemoglobin), vital for most animal life on Earth. When Mg(II) is substituted instead of

Fe(II), the resulting structure forms the basis for chlorophyll, without which plant life on Earth would be unable to produce food from the sun. Porphyrins can form complexes with many transition metal ions, and those of Fe, Ni and Co have been shown to exhibit magnetic properties [49].

As well as by transition metal binding, complex porphyrins can be formed through the attachment of side chains to the outer carbon ring, most commonly at the 5, 10, 15 and 20 positions (as indicated in Figure 1.1). Such substituent groups alter both the bonding of the molecule and its electronic structure.

Depending on the central transition metal's oxidation state, it can bond to a fifth ligand pointing perpendicularly out of the plane of the porphyrin macrocycle, as in the case of MnClTPP. This ligand can be physically manipulated by annealing the organic layer or chemically altered by subjecting the molecules to reactive gas. The nature of the ligand affects the electronic structure of the porphyrin, which can be probed by scanning tunneling microscopy and X-ray spectroscopy.

In addition to the organic molecule examined, the choice of surface is crucial, with some substrates acting as templates for the the molecules' self-organisation.

When W(110) is oxidised it forms an ultra-thin O–W–O trilayer on its surface. This trilayer corresponds to the $WO_2(010)$ structure, however due to the slight lattice mismatch between W(110) and $WO_2(010)$, the surface reconstructs to form a strained-commensurate overlayer exhibiting ordered oxide nanorows oriented along the [$\bar{3}37$] and [$\bar{3}3\bar{7}$] directions of the substrate.

Such nanorows can be used to template the deposition of C_{60} molecules, and the morphology and chemistry of the surface cause the molecular layer to exhibit interesting physical and chemical properties.

In order to highlight the effect of the molecule-substrate interaction, NiDPP is deposited onto two different, but related, surfaces, Ag(111) and Ag/Si(111)-$\sqrt{3} \times \sqrt{3}$ R30°. Ag(111), which will also act as the substrate for MnClTPP deposition, is a simple close-packed noble metal surface, while Ag/Si(111) has the so-called honeycomb-chain-trimer structure, consisting of pseudo-hexagons of Ag surrounding Si trimers. This more complex and reactive surface interacts more strongly with the NiDPP molecules, affecting their self-assembly [50].

In chapter 3, C_{60} molecules are deposited onto the WO_2/W(110) surface, which exhibits a regular array of oxide nanorows. This causes some molecules to lie topologically lower than others, and they appear as dark chains in STM images. The ultrathin WO_2 layer also decouples the C_{60} molecules from the underlying W(110) substrate, allowing charge to accumulate on individual C_{60} molecules.

Chapter 4 discusses the effect two different, but related, surfaces have on the self-assembly of NiDPP molecules. Ag(111) is a relatively-simple, inert surface which leads to a close-packed structure, whereas the complex Ag/Si(111)-$\sqrt{3} \times \sqrt{3}$ R30° surface is more reactive and gives rise to a random domain structure within the NiDPP thin film.

Finally, MnClTPP is deposited onto the Ag(111) surface in chapter 5, again leading to a close-packed structure. However, this unreactive surface still plays a vital role in the transformation of the axial Cl-ligand. When the

Cl is removed from the molecule by annealing, an atom from the Ag(111)
surface acts as a fifth ligand, stabilising the Mn(III)TPP state.

Chapter 2

Experimental Techniques

In this chapter, the experimental techniques used over the course of this thesis will be explained. These are all common surface science techniques, ranging from measurements averaged over a large area of the surface (Auger electron spectroscopy, Section 2.1; low-energy electron diffraction, Section 2.2; etc.) to a very localised technique that can probe materials on the atomic scale (scanning tunneling microscopy, Section 2.3). The most accurate *ab initio* simulation technique available, density functional theory, is invaluable in explaining observed experimental results, and will be examined in Section 2.6.

2.1 Auger electron spectroscopy

Auger electron spectroscopy (AES) is a surface-sensitive and most importantly material-sensitive technique based on the Auger effect, which allows the characterisation of a surface's cleanliness and make-up. The Auger effect was discovered independently by Lise Meitner [51] and Pierre Auger [52] in

7

the 1920s, however it wasn't until the 1950s that its value as an experimental technique was realised.

2.1.1 The Auger effect

The Auger effect describes the non-radiative emission of an electron after a core vacancy is filled. A schematic of the Auger process is shown in Figure 2.1.
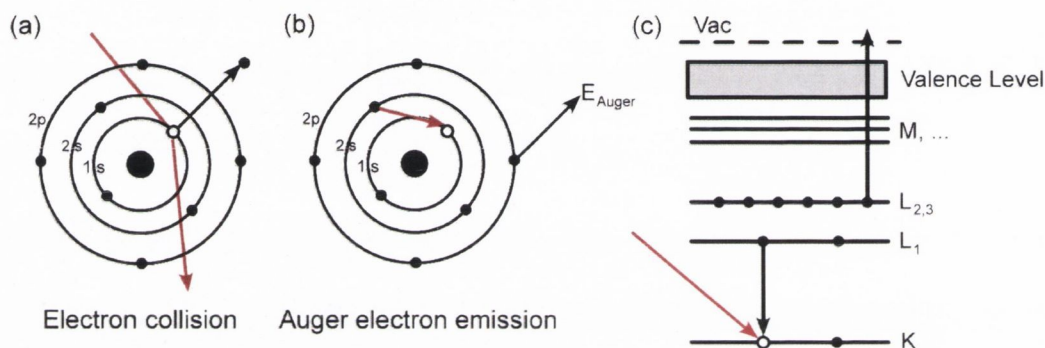
Figure 2.1: Schematic of the Auger process. (a) An impinging high-energy electron collides with a core electron, leaving behind a vacancy. (b) The vacancy is filled by a higher-level electron. The energy released causes the emission of an Auger electron. (c) The energy of the Auger electron is defined by the difference between the initial transition and the original energy level of the Auger electron before emission.

A high-energy electron (or photon) collides with an atom, causing the emission of a core electron (Figure 2.1a). The vacancy left behind is then filled by an outer-shell electron (Figure 2.1b). The energy released then stimulates the emission of an Auger electron, which can be detected and analysed. The kinetic energy of the Auger electron is the difference between the initial transition ($L_1 \rightarrow K$ in Figure 2.1c) and the Auger electron's ionisation energy ($L_{2,3}$). The Auger electron is defined by the spectroscopic notation of the energy levels involved in its emission ($KL_1L_{2,3}$ in Figure 2.1).

The K, L, M, etc. nomenclature used to describe the transitions is something of a holdover from the early days of X-ray research. The Nobel laureate Charles G. Barkla first noticed that some X-rays were able to penetrate thicker sheets of metal than others. He began to characterise these differing penetration "strengths" as "A" for more penetrating and "B" for less penetrating, however he worried that further types of X-rays would be discovered, and so reclassified A as K and B as L, to leave the labels A–J free. We now know that his K-type rays were produced by the refilling of the innermost 1s shell in a manner similar to that in Figure 2.1, and there can be no A–J transitions to closer-bound orbitals, however the nomenclature has been kept for historical reasons.

In this way, this terminology is commonly used in spectroscopic techniques such as AES. An electronic orbital's principal quantum number n is indicated alphabetically by its letter, i.e. K ($n = 1$; 1s), L ($n = 2$; 2s, 2p), etc. The subscript on L and higher gives a unique designation to each of the different orbitals which may have the same n, but different l, s or j quantum numbers, i.e. L_1 has quantum numbers $n = 2$ and $l = 0$, and so corresponds to the 2s orbital; L_2 is $2p_{(1/2)}$ with $n = 2$, $l = 1$, $j = \frac{1}{2}$ and L_3 is $2p_{(3/2)}$ with $n = 2$, $l = 1$, $j = \frac{3}{2}$, and so on in order of increasing energy. When a transition involves multiple orbitals it is described by the orbitals' spectroscopic notation, such as the $KL_1L_{2,3}$ transition in Figure 2.1.

2.1.2 Auger electron spectroscopy

The energies of Auger transitions are specific to each element and its chemical environment, so that its Auger spectrum acts as an elemental "fingerprint", which can be compared to a catalogue of known spectra. Each element typically has one or more "characteristic peaks" which can be used to detect its presence in complex spectra, e.g. when organic molecules are deposited on a surface, or when testing a surface for possible contamination.
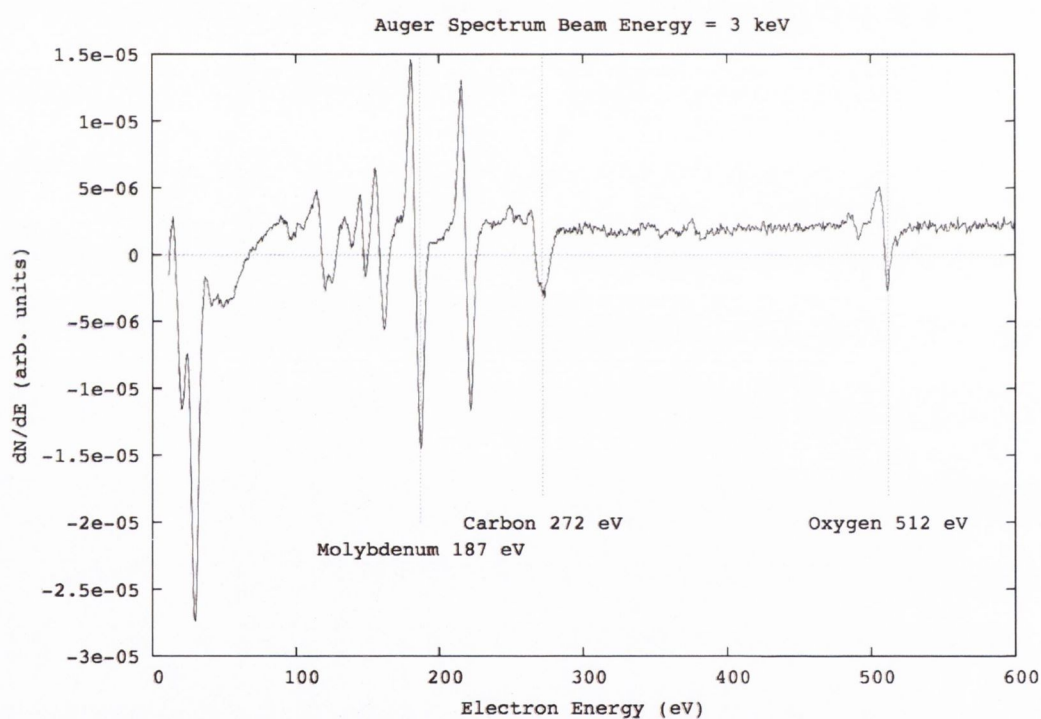
Figure 2.2: Auger spectrum of a Mo sample contaminated by O and C. The primary beam energy was 3 keV and the characteristic peaks of Mo and the main contaminants are shown.

Due to the high linear background signal, the Auger spectrum is usually represented as a differentiated spectrum, i.e. $\frac{dN}{dE}$ vs. E. Due to the fact that the differential of a peak (i.e. its slope) will be represented as first a negative

and then positive double peak, it is usual to refer only to the negative peak's position.

An example spectrum of a dirty Mo(110) sample is shown in Figure 2.2. The characteristic peaks of molybdenum (187 eV), and the two main contaminants, oxygen (512 eV) and carbon (272 eV), are highlighted.

2.1.3   Auger electron spectroscopy set-up

Figure 2.3 shows the experimental set-up of the Auger electron spectroscopy apparatus. 3–5 keV electrons are emitted by the electron gun and collide with the sample. The resulting Auger electrons are passed through a cylindrical mirror analyser (CMA).

The CMA consists of two concentric cylinders, the outer, which can have a bias of −10 V to −2000 V placed upon it, and the inner, which is grounded. Two apertures allow a narrow beam of Auger electrons to enter the space between the two cylinders, where they are repelled by the outer bias. The shape of the CMA is designed so that only those electrons with the same energy as the outer bias can pass through both apertures and arrive at the detector.

In this way the CMA selects the electrons according to their energy by sweeping through energies from 10–2000 eV, however, partial sweeps can also be used to more quickly screen samples, and to limit the time they are subjected to high energy 3–5 keV electrons, which can damage surface structures.
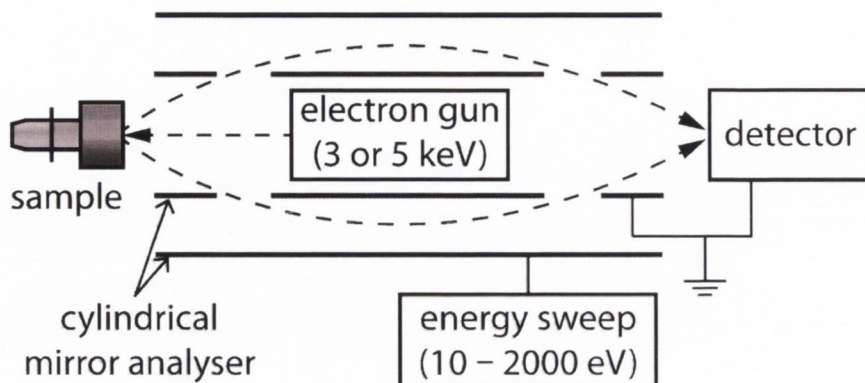
Figure 2.3: Auger electron spectroscopy apparatus.

2.2   Low-energy electron diffraction

Low-energy electron diffraction (LEED) is based on the diffraction of electrons by the Bragg planes of a single-crystalline sample. Due to the electrons' low energy (typically 10–200 eV), their mean free path in the material is limited to the first few atomic layers, and so LEED gives information only on the surface's topological structure.

The diffraction of electrons by a crystal's lattice was first observed experimentally by Davisson and Germer in 1927 [53]. The experiment was originally intended to study the surface of a nickel target, with the hypothesis that even the smoothest surface would be too rough for specular reflection, and would instead diffuse an incident electron beam. However, after the accidental oxidation of the target, the sample was cleaned in a high-temperature oven, thus creating single crystallites on the surface. When the experiment was repeated, they observed that the electrons were scattered as if by a diffraction grating, and using Bragg's law it was shown that the electrons were diffracting from the nickel crystal planes. This serendipitous result

bears mentioning because not only is it the first experimental evidence of the wave–particle duality of matter, but was also important for the development of quantum mechanics and the Schrödinger equation.

2.2.1   Bragg's law

The diffraction of X-rays from crystalline solids was explained by William Lawrence Bragg by describing the solid as a series of parallel planes, and the characteristic spots observed originating from points of constructive interference of the X-rays. A similar treatment can be performed for electron diffraction, since the electrons' de Broglie wavelength is comparable to the interatomic spacing, however an alternate theory is described in Section 2.2.3 for scattering due to a surface.

As shown in Figure 2.4, depending on the angle of diffraction from the atoms in the crystal, the path length difference between the scattered waves reflecting from different layers of the crystal can cause them to interfere constructively (Figure 2.4a) or destructively (Figure 2.4b).

The path difference is given by $d\sin(\theta)$, where d is the interlayer spacing, and θ is the angle subtended between the incident and diffracted waves. In the case of Figure 2.4a, the path length difference between the two reflected waves is an integer number of wavelengths (2λ). This is equivalent to a phase shift of 2π, and so the two waves constructively interfere. In contrast, in Figure 2.4b the path difference is equal to one and a half wavelengths, i.e. a phase shift of π, leading to destructive interference.
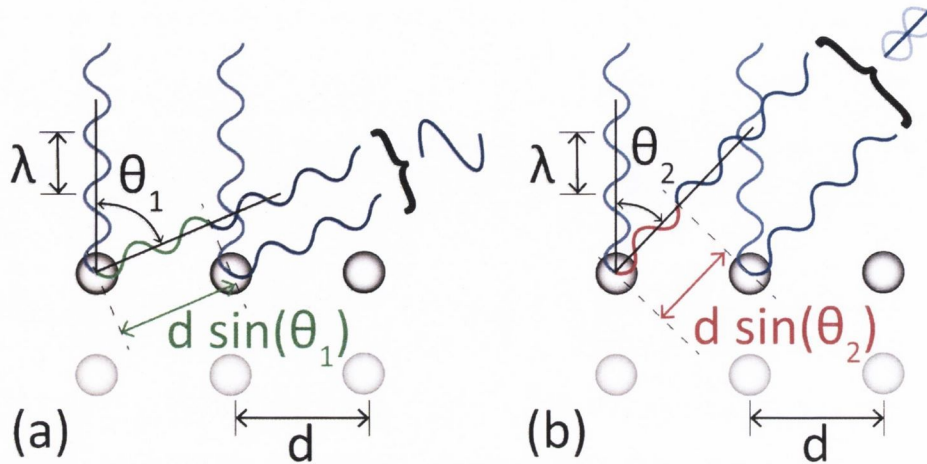
Figure 2.4: Diagram of Bragg diffraction. The incident beams are shown normal to the lattice planes of the sample, as in LEED. Different angles of the diffracted waves exhibit **(a)** constructive and **(b)** destructive interference, depending on whether the path difference (shown in green for constructive and red for destructive interference. λ is the wavelength of the incident beam, d is the in-plane atomic spacing and θ is the angle between the incident beam and the atomic layers.

The relation derived by Bragg for constructive interference between two waves at normal incidence was:

$$n\lambda = d\sin(\theta) \tag{2.1}$$

where n is an integer and λ is the wavelength of the incident wave.

It is clear from Equation 2.1 that some angles will lead to maxima in the diffracted beam intensity, but it should be noted that in the case of the diagram, if only two atoms are involved, there will be a smooth transition between maxima and minima. In practice, the size of the electron beam in LEED means that many atoms diffract the beam, mainly sharp peaks are

observed, surrounded by areas of destructive interference. For this reason LEED is an averaging technique.

Bragg diffraction (and hence LEED) does not directly measure real-space atomic distances. Instead, the distance between diffraction spots is inversely proportional to the interatomic spacing, d, and the $n\lambda$ term is related to the number of wavelengths that fit between atoms. Therefore, a LEED pattern describes reciprocal space.

2.2.2 The reciprocal lattice

Reciprocal space effectively represents the periodicity of a Bravais lattice. This is equivalent to performing a Fourier transform on a periodic function.

Consider a vector $\vec{R}$, which represents the Bravais lattice, and a plane wave $e^{i\vec{K}\cdot\vec{r}} = \cos(\vec{K}\cdot\vec{r}) + i\sin(\vec{K}\cdot\vec{r})$ which has the same periodicity as the Bravais lattice.

If their periodicities are equal, then for any point $\vec{r}$:

$$e^{i\vec{K}\cdot(\vec{r}+\vec{R})} = e^{i\vec{K}\cdot\vec{r}}$$

$$e^{i\vec{K}\cdot\vec{r}}e^{i\vec{K}\cdot\vec{R}} = e^{i\vec{K}\cdot\vec{r}}$$

$$\therefore e^{i\vec{K}\cdot\vec{R}} = 1$$

The set of vectors $\vec{K}$ which satisfy the above relation describes the reciprocal lattice. It is also noted that the reciprocal lattice is itself a Bravais lattice, and the reciprocal of the reciprocal lattice returns the original real-space lattice.

For an infinite 3-dimensional lattice, defined by its primitive vectors $(\vec{a}, \vec{b}, \vec{c})$, the reciprocal lattice $(\vec{a^*}, \vec{b^*}, \vec{c^*})$ is defined as:

$$\vec{a^*} = 2\pi \frac{\vec{b} \times \vec{c}}{\vec{a} \cdot (\vec{b} \times \vec{c})} \qquad (2.2)$$

$$\vec{b^*} = 2\pi \frac{\vec{c} \times \vec{a}}{\vec{b} \cdot (\vec{c} \times \vec{a})} \qquad (2.3)$$

$$\vec{c^*} = 2\pi \frac{\vec{a} \times \vec{b}}{\vec{c} \cdot (\vec{a} \times \vec{b})} \qquad (2.4)$$

2.2.3   Surface diffraction

The de Broglie wavelength of an electron, λ_e is given by:

$$\lambda = \frac{h}{\sqrt{2m_e E}}; \qquad \lambda_e[\text{nm}] \approx \sqrt{\frac{1.5}{E_e[\text{eV}]}} \qquad (2.5)$$

where m_e and E_e are the electron's mass and kinetic energy, respectively.

Consider a beam of electrons impinging on a 3-dimensional crystal, as in Section 2.2.1. For an incident electron with wave vector $\vec{k_0} = 2\pi/h\lambda_0$, and a scattered wave vector $\vec{k} = 2\pi/h\lambda$, the von Laue condition for constructive interference states that:

$$\vec{k} - \vec{k_0} = \vec{G}_{hkl} = h\vec{a^*} + k\vec{b^*} + l\vec{c^*} \qquad (2.6)$$

i.e. $\vec{G}_{hkl}$ is a vector of the reciprocal lattice.*

Only elastic scattering is considered, and so energy is conserved, i.e. $|\vec{k_0}| = |\vec{k}|$. As mentioned, the mean free path of electrons within a crystal

---

*Note that the condition $2\vec{k_0} \cdot \vec{G} = |\vec{G}|^2$ reduces to the Bragg condition $n\lambda = 2d\sin(\theta)$

is small and so only the first few atomic layers play a role in the diffraction. Therefore, there are no diffraction elements perpendicular to the surface, and the lattice can be considered as a 2-dimensional series of rods extending from the surface lattice points.

Following from this, the 2-dimensional simplification of Equation 2.6 and the reciprocal lattice vectors become

$$\vec{k^{2D}} - \vec{k_0^{2D}} = \vec{G}_{hk} = h\vec{a^*} + k\vec{b^*} \tag{2.7}$$

$$\vec{a^*} = 2\pi \frac{\vec{b} \times \hat{n}}{|\vec{a} \times \vec{b}|} \tag{2.8}$$

$$\vec{b^*} = 2\pi \frac{\hat{n} \times \vec{a}}{|\vec{a} \times \vec{b}|} \tag{2.9}$$

where $\hat{n}$ is the surface normal unit vector.

A useful visualisation of the effect of Equation 2.7 is the Ewald sphere, shown in Figure 2.5.

The Ewald sphere illustrates the points of constructive interference formed by the incident and diffracted electron waves. The upper half of the sphere can be considered as the hemispherical fluorescent screen of the LEED apparatus, and from Figure 2.5b it is clear how a higher kinetic energy leads to more LEED spots visible on the screen.

2.2.4 Low-energy electron diffraction apparatus

The set-up for LEED is shown in Figure 2.6a.

Electrons are emitted from the electron gun by an accelerating voltage V, and are diffracted by the sample. They then pass through a series of up
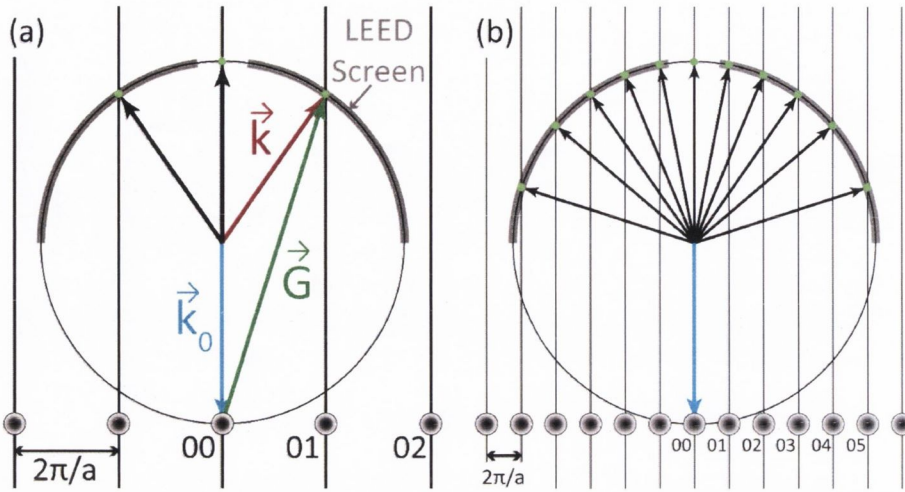
Figure 2.5: The Ewald sphere construction. The sphere has a radius $|\vec{k_0}|$, and because LEED is performed using a beam of electrons impinging normal to the surface, by default the incident wave vector $\vec{k_0}$ lies parallel to the vertical 00 rod. The spots (rods) are numbered by their hk value. Points where the rods cross the sphere coincide with the Laue condition (Equation 2.7). **(a)** Spots are then formed on the fluorescent LEED screen at these points of constructive interference. **(b)** at higher kinetic energies, the Ewald sphere radius increases and more rods cross the sphere, thus more LEED spots (green circles) are visible.
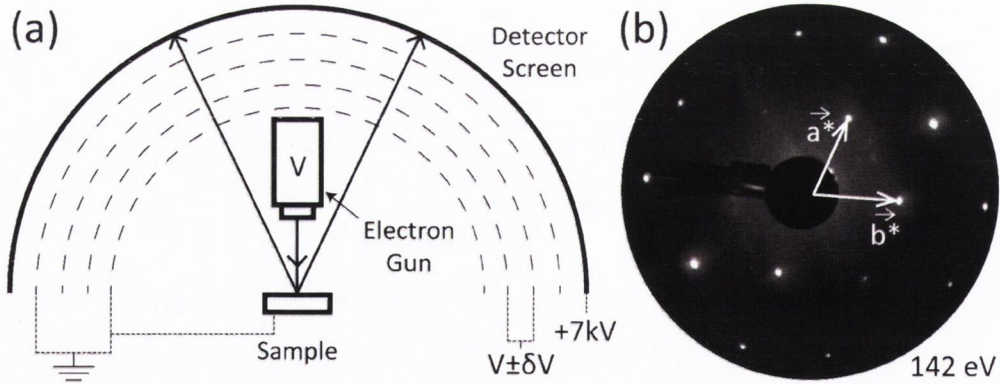
Figure 2.6: **(a)** Experimental apparatus for low energy electron diffraction. **(b)** LEED pattern recorded from the clean Mo(110) surface at an energy of 142 eV. The primitive reciprocal lattice vectors $\vec{a^*}$ and $\vec{b^*}$ are shown in white.

to four grids before colliding with a fluorescent coating on the screen, where light is emitted. The first and last grids are held at the ground potential

to confine the field. The central grids are kept close to V at $V \pm \delta V$, in order to select only elastically scattered electrons. Finally, the electrons are post-accelerated by a high voltage placed on the screen, in order to maximise the efficiency of the fluorescence.

A LEED pattern obtained from the clean Mo(110) surface is shown in Figure 2.6b, showing the hexagonal reciprocal lattice representative of the close-packed (110) surface of a body-centred cubic crystal.

2.3   Scanning tunneling microscopy

The scanning tunneling microscope (STM) was developed at IBM in the 1980s by Gerd Binnig and Heinrich Rohrer, however no introduction to scanning probe microscopy would be complete without mentioning the contribution of Edward Hutchinson (Hutchie) Synge.

E H Synge was the nephew of playwright of John Millington Synge and older brother of physicist John Lighton Synge, and he studied mathematics at (but did not graduate from) Trinity College Dublin. Becoming reclusive after his time at TCD, it was not until after his death that his contributions to what is now known as nanoscience were recognised. In correspondence with Albert Einstein in 1928, Synge elaborated on his idea for a scanning near-field optical microscope (SNOM) capable of optically imaging materials with sub-wavelength resolution by scanning the aperture over the surface, making point-by-point measurements. Unfortunately for Hutchie, his ideas were at least 50 years ahead of their time, with technology only catching up with him after the development of piezoelectric materials to facilitate the

scanning mechanism. However, this often-overlooked pioneer described quite succinctly the technology which would later be used for SNOM and STM today.

2.3.1   Quantum tunneling

Imagine attempting to throw a ball to a person on the other side of a wall. Rather than tossing it over the wall, you hurl the ball directly at it, and instead of bouncing off, it passes through to the other side unscathed. This seems fantastic, but this is analogous to the process that occurs on the quantum scale, known as tunneling.

The time-independent Schrödinger equation describes the motion of a particle's (in this case an electron's) wavefunction $\psi_n(z)$ moving under the influence of a potential $U(z)$. For simplicity, the one-dimensional case is considered:

$$-\frac{\hbar^2}{2m}\frac{d^2\psi_n(z)}{dz^2} + U(z)\psi_n(z) = E\psi_n(z) \tag{2.10}$$

where $\hbar$ is the reduced Planck's constant, m is the mass of the electron, E is its energy and z its position.

For a wave encountering the potential barrier $U(z)$, as in Figure 2.7a, there are three regimes to consider: (I) the travelling wave before meeting the barrier, where $U(z < 0) = 0$; (II) the wave inside the barrier, where $U(0 < z < W) = U > E$; and (III) the wave after encountering the barrier, where $U(z > W) = 0$. In the classical case, the wavefunction's value in regimes (II) and (III) would be equal to zero, however when one solves the Schrödinger equation, two solutions are possible; a travelling wave where
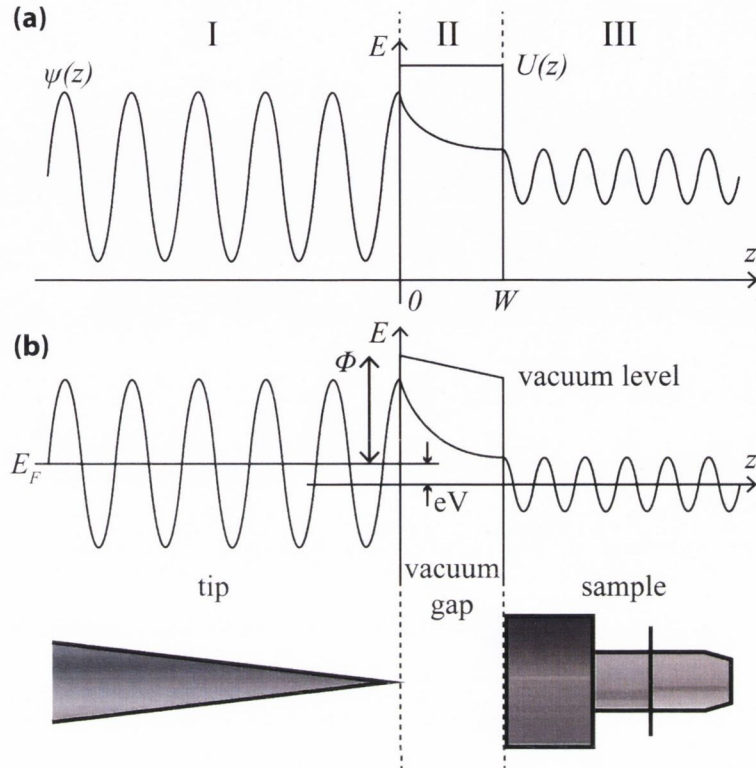
Figure 2.7: **(a)** The general tunneling case through a one-dimensional potential barrier. **(b)** Schematic of the tunneling arrangement from the tip to the sample through the vacuum barrier in an STM.

$U(z) < E$ (regimes (I) and (III)) and an exponential decay within the barrier (regime (II)). We are only concerned with the latter of the two, as this is what governs tunneling.

$$\psi_n(z) = \psi_n(0)e^{\pm \kappa z} \qquad \text{where} \qquad \kappa = \frac{\sqrt{2m(U - E)}}{\hbar} \qquad (2.11)$$

Since the probability density is given by the square of the wave function and, assuming there is a small bias V between the tip and sample, in order for tunneling to occur there must be a finite probability of finding an electron

from $z = 0$ at $z = W$, thus:

$$P \propto |\psi_n(0)|^2 e^{-2\kappa W} \tag{2.12}$$

If the bias is small, $U(z) - E \approx \phi_M$, the work function of the sample. ϕ_M gives the minimum energy needed to bring electrons from the highest occupied energy level (Fermi level, E_F, in metals at $T = 0\,\mathrm{K}$) to the vacuum level. The small bias also means that only electron states within eV of E_F are excited, thus tunneling is mainly by electrons near the Fermi Energy.

However, in order for tunneling to occur (assuming electrons are tunneling from tip to surface, as in Figure 2.7b) there must be empty states of the same energy in the surface for the electrons to tunnel into, therefore the tunneling current is dependent on the density of states, as well as the number of electrons between $E_F - eV$ and E_F.

$$i.e. \qquad I \propto \sum_{E_f - eV}^{E_f} |\psi_n(0)|^2 e^{-2\kappa W} \tag{2.13}$$

By definition, summing the probability over an energy range, such as between $E_F - \varepsilon$ and E_F, gives the number of states available in this energy range per unit volume, i.e. the local density of states, $\rho_s(z, E)$:

$$\rho_s(z, E) = \frac{1}{\varepsilon} \sum_{E - \varepsilon}^{E} |\psi_n(z)|^2 \tag{2.14}$$

Therefore the tunneling current is proportional to the local density of states and a scaling factor which decays exponentially with the width of the gap,

$$I \propto \sum_{E_f - eV}^{E_f} \rho_s(z, E) e^{-2\kappa W} \tag{2.15}$$

An elegant demonstration of the power of the exponential dependence arises when considering typical physical parameters. Taking a value for the work function of $\phi_M \sim 4\,\text{eV}$ gives $\kappa \approx 1.025 \text{Å}^{-1}$. If the difference between the distance from the sample of the closest tip atom, d_1, and the second closest atom, d_2, is $d_2 - d_1 \approx 1\,\text{Å}$, then the ratio between the current flowing through atom 1 to that flowing through atom 2 is $I_1/I_2 \approx 10$, i.e. a tip atom only $1\,\text{Å}$ closer to the surface collects 90% of the current flowing between the surface and tip [54].

It is this exponential dependence of the tunneling current on the gap width which gives the STM its high resolution: in the horizontal plane only those atoms closest to the apex contribute significantly to tunneling; and in the vertical direction, a small $1\,\text{Å}$ difference in height changes the current by 10 fold.

2.3.2 The scanning tunneling microscope

Binnig and Rohrer were awarded the 1986 Nobel prize in Physics for their invention of the scanning tunneling microscope (STM). The STM utilises the phenomenon of quantum tunneling in order to visualise the electronic and topological structure of the surfaces of metals and semiconductors. The apparatus consists of an extremely sharp needle or "tip", the apex of which

has a radius of curvature on the order of several nanometers, and is capable
of precise positioning and movement. This tip is brought extremely close to
the conducting sample, upon which a voltage bias is placed, and the tip is
rastered across the sample, recording the tunneling current at every point in
the raster scan.

The positioning apparatus usually makes use of the reverse piezoelec-
tric effect. When a voltage is placed across a piezoelectric crystal it un-
dergoes a deformation proportional to the voltage. This deformation is ex-
tremely controllable and repeatable, allowing the tip to be positioned with
sub-nanometer precision.

The STM can be operated in two modes: constant-current and constant-
height. The difference between these modes is illustrated in Figure 2.8. In
the constant-current mode, the tunneling current is kept constant using an
electronic feedback loop, and the height is varied, thus causing the tip to map
out a convolution of the density of states and the topography of the surface.
The constant-height mode on the other hand scans the tip at a constant
height and records the varying tunneling current due to the corrugation and
make-up of the surface.

The latter of these two modes is considerably more "risky", since the
roughness of the surface on the nanoscale is unknown before scanning, and
so it is inevitable that the tip will come into contact with parts of the surface,
either changing the tip's structure and hence the scanned image, or ruining
the tip altogether. The advantage of constant-height over constant-current
is that very high speed scanning is possible, since the constant-current mode
is limited by the response of the feedback system, however it is only suitable
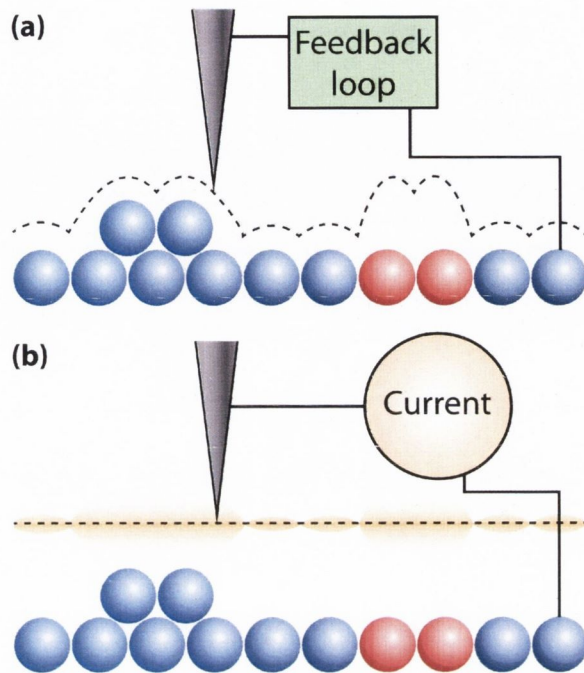
Figure 2.8: **(a)** Tunneling in the constant-current mode. The dotted line shows the path followed by the STM tip. Notice that the substituted atoms shown in red exhibit a different apparent height to the blue surface atoms due to their different local density of states. **(b)** STM tip operating in the constant-height mode. The tip maintains a constant height over the surface and records the current, shown by an orange glow. Again, the current due to the substituted atoms is higher than the surrounding surface.

for atomically-flat systems, and so all images presented in this thesis were obtained in constant-current mode.

2.3.3   Createc GmbH LT-STM

The low-temperature STM (LT-STM) used in Chapters 3 and 5 for the C_{60} and MnClTPP work is a commercial instrument from Createc GmbH, shown in Figure 2.9, modified to accept "Omicron-style" sample plates. It consists of independent analysis and preparation chambers, separated by a gate valve

and each pumped by their own ionisation pump, and a differentially pumped load-lock with a turbomolecular pump. The preparation chamber has a 4-axis (x, y, z and θ) manipulator with integrated electron-beam heater for sample preparation and copper block for LEED measurements and deposition, with optional LN_2 cooling.
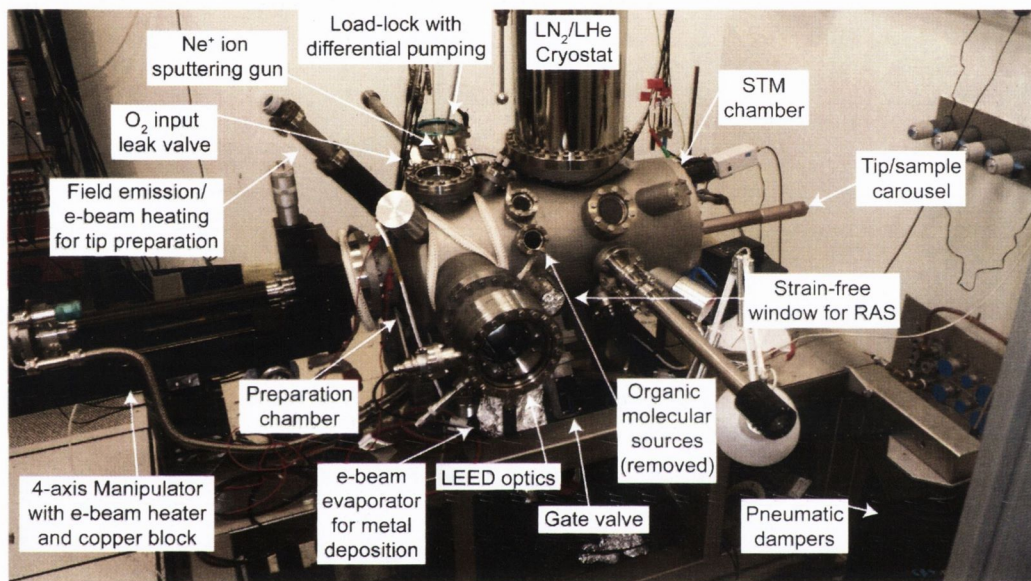
Figure 2.9: Photograph of the Createc LT-STM system, with its component parts labelled.

Also integrated into the preparation chamber are a Ne^+ ion sputtering gun, metallic and organic deposition sources, LEED optics, leak valve for gas input and a tip preparation stage with field emission via a single-crystalline Mo plate, and e-beam heating using a "V"-shape filament.

The analysis chamber houses a tip/sample carousel and the STM head. The scanning head is cooled via a two-chamber cryostat compatible with either liquid nitrogen or liquid helium. The head used for measurements in this work was a Besocke-style design, however it has since been replaced

by a Slider-type head (commissioning in progress). The tip is magnetically mounted onto the scanning head in both designs, however the Slider scanner allows up to 10 mm of movement in the z-direction, while the Besocke only permitted 2–3 mm of vertical motion.

The entire chamber can be supported by four pneumatic dampers to mechanically decouple it from its environment and reduce noise during scanning.

2.3.4 Omicron GmbH VT-STM
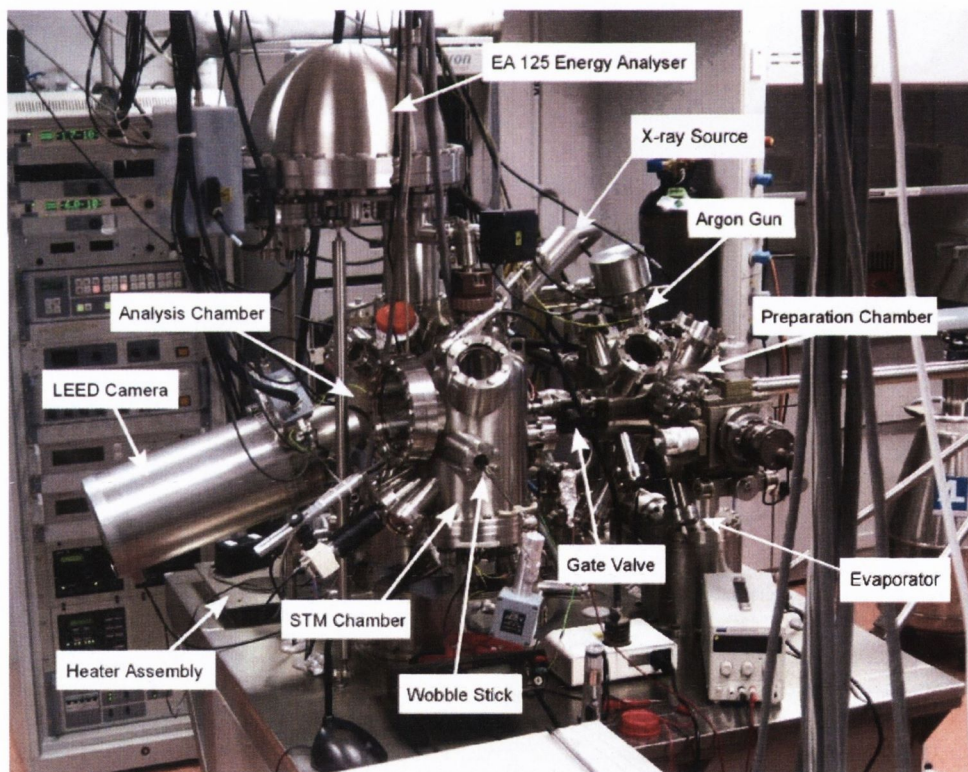
Figure 2.10: Photograph of the Omicron VT-STM system, with its component parts labelled [55].

The images of NiDPP in Chapter 4 were obtained using a variable-temperature scanner (VT-STM) from Omicron, shown in Figure 2.10 [55].

Similar to the Createc system, it consists of separate preparation and analysis chambers, and a fast entry load-lock, again with an ionisation pump on each of the main chambers and a turbomolecular pump attached to the load-lock.

The preparation chamber is equipped with an Ar^+ ion sputter gun, a manipulator with resistive sample heating and three molecular evaporators. The analysis chamber houses another manipulator with direct and resistive heating, a DAR 400 twin-anode X-ray source, an EA 125 energy analyser for XPS, Omicron LEED optics and the Omicron VT-STM head. In the VT-STM, the sample is placed above the tip with the surface facing down and the tip facing up, in contrast to the Createc scanner.

2.3.5   Image processing

Data collected by an STM is in the form of an (X, Y, Z) map of height values, i.e. for each of 512×512 points in the X–Y plane, the STM records the height of the tip (Z). This is then represented by specialised software [56] as a topographic image. Usually this image will include mechanical noise from the environment, artefacts introduced by tip instability, piezo creep, etc. In order to remove these artefacts, the image is processed by various techniques such as plane subtraction, flattening, smoothing, reducing the Z-range, 2-D fast Fourier transform filtering, drift correction, etc. Some treatments are more radical than others. In this thesis all original STM images have been processed to some degree, the minimum being plane subtraction and Z-range equalisation to enhance contrast, which is applied to all images, however none

have been corrected for thermal drift or piezo creep. Any further processing is noted in the relevant figure caption.

2.4 X-ray absorption spectroscopy

X-ray absorption spectroscopy (XAS) is a technique for probing the local electronic structure of materials. Due to the need for a high signal-to-noise ratio, high brilliance source, and tunable frequency range, synchrotron X-ray radiation is generally used to analyse the small amount of material comprising a molecular monolayer.

During an XAS measurement, a monochromated X-ray beam is tuned to an energy range where core electrons of the sample can be excited and passed through a sample. This excitation is observed as a loss in intensity of the transmitted X-ray beam, and the difference in intensity between the incident beam (I_0) and transmitted beam (I_t) is expressed as the absorption coefficient μ:

$$I_t = I_0 e^{-\mu x}$$

$$\therefore \mu = \frac{-\ln(I_t/I_0)}{x}$$

where x is the thickness of the sample. With a constant sample thickness, a plot of μ vs. incident energy gives a "fingerprint" of the chemical nature and electronic structure of the sample.

Due to the complex nature of the interaction between the incident X-rays and the crystal, the resulting XAS spectra exhibit several distinct features, as shown in Figure 2.11.
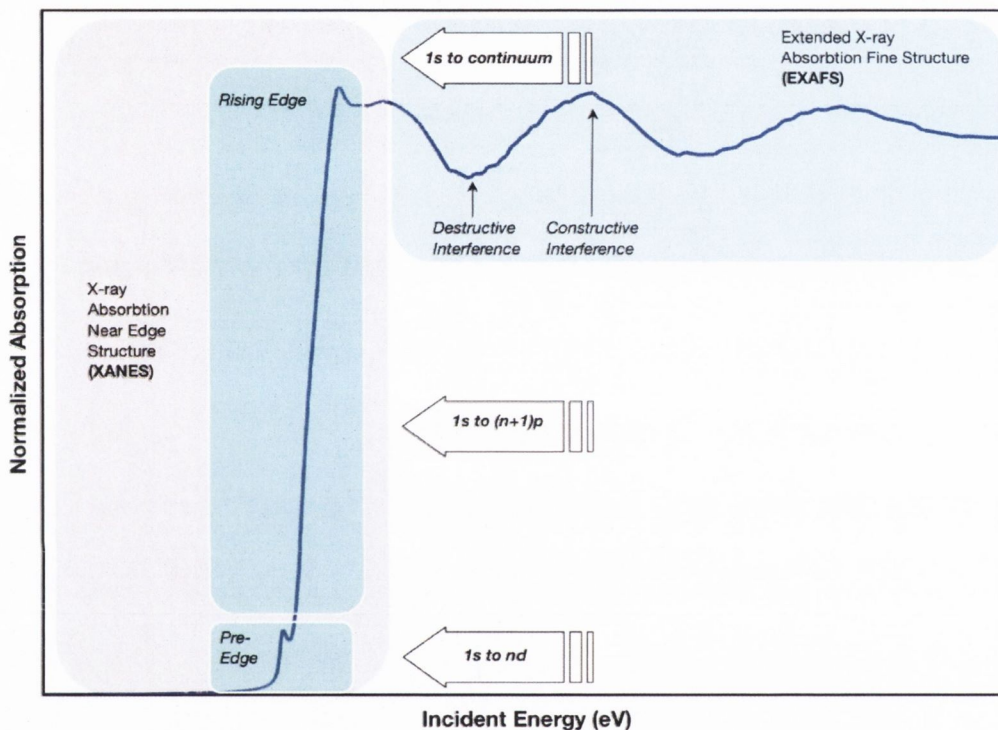
Figure 2.11: A schematic XAS spectrum, with the main peak regions and their sources highlighted [57].

Walther Kossel first explained the structure of X-ray absorption peaks as due to electronic transitions to the first unoccupied molecular orbital above the Fermi energy (chemical potential). In turn, these were named the "Kossel structure", however the more usual name for this region today is the absorption edge region.

The dominant feature of the spectrum produced by X-ray absorption is the "rising edge", which occurs at the core-level binding energy of the absorb-

ing atoms, with some smaller "pre-edge" features present at lower energies. Measurements of this are usually referred to as XANES (X-ray Absorption Near-Edge Structure) or NEXAFS (Near-edge X-ray Absorption Fine Structure). Mn 2p NEXAFS spectra are presented in Chapter 5 (Figure 5.7).

The oscillatory structure which can extend for hundreds of eV past the absorption edge was explained by Ralph Kronig, who had earlier first postulated the idea of electron spin. This so-called "Kronig structure" was attributed to multiple scatterings of the excited electron by the crystal lattice, and Kronig's equation formed the basis for many early publications on X-ray absorption, although his theoretical basis was somewhat flawed. It was not until the 1970s when Edward Stern and colleagues at the University of Washington and Boeing Scientific Research Laboratory teased out the details of the theory [58]. The modern description for the high-energy structure is EXAFS (Extended X-ray Absorption Fine Structure).

At higher energies, scattering of the excited photo-electron from neighbouring atoms gives rise to a fine structure (EXAFS) due to the constructive and destructive interference of the excited and scattered electrons. When NEXAFS (XANES) and EXAFS are combined, the overall technique is known as XAFS (X-ray absorption fine structure).

The edges are designated according to the principal quantum number of the core electron excited; n = 1, 2, and 3 correspond to the K-, L- and M-edges, respectively. These transitions are shown schematically in Figure 2.12

Since a photo-electron is excited into an unoccupied orbital or band, XANES (NEXAFS) primarily gives information on the sample's unoccupied states in the presence of the core-hole induced by the initial excitation from
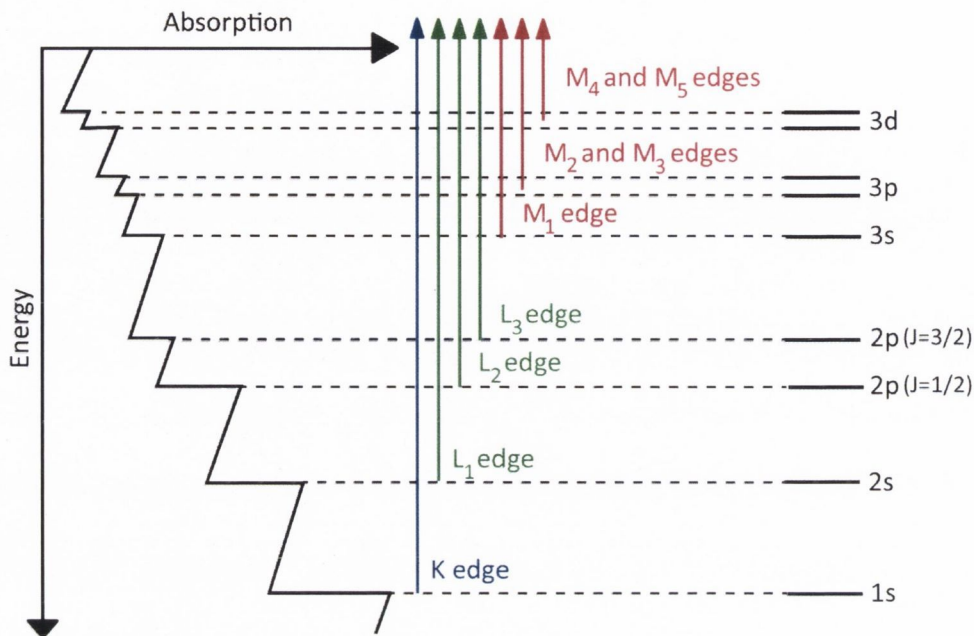
Figure 2.12: Schematic diagram showing the designation of XAS transitions according to their core energy level. K transitions are excited from the 1s state, L from the 2s and 2p, and M from the 3s, 3p and 3d states [59].

the core-level, and thus the final NEXAFS state can be thought of as a core "exciton".

2.5 X-ray photoemission spectroscopy

Similar to XAS, X-ray photoemission spectroscopy (XPS) involves a colli-mated, monochromatic beam of X-rays incident on a sample, however in this case, the kinetic energy and number of photoelectrons which escape the sur-face are measured. Due to the small mean free path of electrons in a material, XPS is a surface-sensitive technique, as only electrons ejected from the top 1–10 nm of a sample can be detected.

The photoelectric effect has a rich history, beginning with its discovery in 1887 by Heinrich Hertz, and its Nobel prize-winning explanation by Albert Einstein in 1905. Several attempts were made to make use of photoelectrons produced by X-rays, however it was only after World War II that Kai Siegbahn developed the equipment necessary for high energy resolution experiments, and, together with engineers from Hewlett Packard, produced the first commercial XPS instrument in 1969. His efforts to develop XPS into a useful tool for science were recognised in 1981 when he shared the Nobel prize in Physics.

An XPS spectrum is generally plotted as the number of electrons detected vs. their binding energy ($E_{binding}$):

$$E_{binding} = E_{photon} - (E_{kinetic} + \phi)$$

where E_{photon} is the photon energy of the X-rays incident on the sample, $E_{kinetic}$ is the kinetic energy of the electron as measured by the instrument, and ϕ is the work function of the spectrometer.

The relative binding energies of the electrons captured depend on their atomic orbitals, with core electrons having a higher $E_{binding}$ than weakly-bound outer-shell electrons, however the particular spectrum of energies observed is characteristic of the element being analysed. The number of electrons counted at a particular element's characteristic energy is directly proportional to the amount of that element within the area irradiated (when a relative scaling factor is taken into account), and so XPS can give a quantitative measure of a sample's make-up.

2.6   Density functional theory

Density functional theory (DFT) is an *ab initio* approach to the calculation
of materials' properties on the atomic scale, in that it is derived from first
principles without assumptions e.g. fitting parameters based on experimental
evidence. However, due to its complex nature, certain justified simplifications
are made in order to allow calculations to be performed with a reasonable
speed.

To perfectly simulate the properties of a material, one must solve the
Schrödinger equation (Equation 2.16) for all the material's electrons and
nuclei. The Hamiltonian for this system is given in Equation 2.17, with the
first two terms describing the kinetic energies of the nuclei and electrons,
respectively, and the following terms the internuclear, electron-electron and
nucleus-electron Coulomb interactions.

$$\hat{H}\Psi(\{\vec{R}_\alpha\};\{\vec{r}_i\}) = \varepsilon\Psi(\{\vec{R}_\alpha\};\{\vec{r}_i\}) \tag{2.16}$$

$$\hat{H} = -\sum_\alpha \frac{h^2}{2M_\alpha}\nabla_\alpha^2 - \sum_i \frac{h^2}{2m}\nabla_i^2 + \frac{e^2}{2}\sum_{\alpha,\beta} \frac{Z_\alpha Z_\beta}{|\vec{R}_\alpha - \vec{R}_\beta|}$$

$$+\frac{e^2}{2}\sum_{i,j} \frac{1}{|\vec{r}_i - \vec{r}_j|} - \frac{e^2}{2}\sum_{i,\alpha} \frac{Z_\alpha}{|\vec{R}_\alpha - \vec{r}_i|} \tag{2.17}$$

For N electrons and M nuclei, this leads to a non-separable partial dif-
ferential equation with $3(M + N)$ variables, which is obviously impossible to
solve in practice for all but the simplest systems.

Instead, the Born-Oppenheimer (BO) approximation states that since
the ratio of the mass of a nucleon to that of an electron $M_n/m_e \approx 1836$,
nuclei move much slower than electrons, and so can be regarded as static;

i.e. their kinetic energy term can be neglected. In this way, the molecular wavefunction is split into an electronic and a nuclear term:

$$\Psi(\{\vec{R}_\alpha\}; \{\vec{r}_i\}) = \psi_e(\{\vec{R}_\alpha\}; \{\vec{r}_i\}) \times \psi_n(\{\vec{R}_\alpha\}) \qquad (2.18)$$

The BO Hamiltonian for the electrons therefore becomes:

$$\hat{H}_{\mathrm{BO}} = -\sum_i \frac{h^2}{2m}\nabla_i^2 + \frac{e^2}{2}\sum_{i,j}\frac{1}{|\vec{r}_i - \vec{r}_j|}$$
$$-\frac{e^2}{2}\sum_{i,\alpha}\frac{Z_\alpha}{|\vec{R}_\alpha - \vec{r}_i|} + \frac{e^2}{2}\sum_{\alpha,\beta}\frac{Z_\alpha Z_\beta}{|\vec{R}_\alpha - \vec{R}_\beta|}$$
$$\therefore \hat{H}_{BO}\psi_e(\{\vec{R}_\alpha\}; \{\vec{r}_i\}) = E_e(\{\vec{R}_\alpha\})\psi_e(\{\vec{R}_\alpha\}; \{\vec{r}_i\}) \qquad (2.19)$$

i.e. the electronic dynamics are effectively decoupled from those of the nuclei. The nuclear coordinates R_α enter the Schrödinger equation as external parameters, not dynamic variables, thus greatly reducing the complexity of the partial differential equation.

The nuclear kinetic energy is then reintroduced into the Schrödinger equation for the nuclear motion:

$$\left(E_e(\{\vec{R}_\alpha\}) - \sum_\alpha \frac{h^2}{2M_\alpha}\nabla_\alpha^2 \right)\psi_n(\{\vec{R}_\alpha\}) = E_{\mathrm{mol}}\psi_n(\{\vec{R}_\alpha\}) \qquad (2.20)$$

where the eigenvalue E_{mol} is the total energy of the molecule.

Implicit in the BO approximation is the idea that electrons which interact with each other merely move in a fixed potential created by the nuclei, and that no electronic transitions occur as a result of the (slow) nuclear motion.

Unfortunately, even the decoupled equation is a very complicated interacting many-body problem and still contains $3N$ variables.

In 1927, just one year after the publication of the Schrödinger equation, Douglas Hartree proposed a formalism to describe many electron systems. In the Hartree approach, the many-body wavefunction is replaced by the product of the wavefunctions of the individual electrons:

$$\Psi_n(\{\vec{r}_i\}) = \psi_1(\vec{r}_1)\psi_2(\vec{r}_2) \cdots \psi_N(\vec{r}_N)$$

Applying this wavefunction to Equation 2.19, and minimising the energy while constraining the wavefunction to be normalised leads to the Hartree equation:

$$\left(-\frac{h^2}{2m}\nabla^2 + V_{\text{ext}}(\vec{r}) + V_H^i(\vec{r})\right)\psi_i(\vec{r}) = \epsilon_i\psi_i(\vec{r}) \qquad (2.21)$$

thus reducing the problem to the solution of a single particle equation in an effective potential, V_H^i, which depends on the single particle orbitals. This is the simplest case of a mean-field approximation to the electron-electron interaction, and is solved using the self-consistent iteration method:

1. Guess starting orbitals

2. Calculate effective potential V_H^i

3. Solve single particle equation

4. Recalculate effective potential from new single particle orbitals

5. Iterate to self-consistency

Unfortunately, in 1930, J. C. Slater and V. A. Fock pointed out that the Hartree method did not conserve the antisymmetry of the wavefunction, and so the more complex Hartree-Fock approximation was developed.

Taking an ansatz for $|\Psi\rangle$ where the Slater determinant guarantees that the Pauli principle is respected and the wavefunction is antisymmetric upon particle exchange:

$$\Psi(\{\vec{r}\}, \{\sigma_i\}) = \frac{1}{\sqrt{N!}} \begin{vmatrix} \psi_1(\vec{r}_1)\chi_1(\sigma_1) & \psi_2(\vec{r}_1)\chi_2(\sigma_1) & \cdots & \psi_N(\vec{r}_1)\chi_N(\sigma_1) \\ \psi_1(\vec{r}_2)\chi_1(\sigma_2) & \psi_2(\vec{r}_2)\chi_2(\sigma_2) & \cdots & \psi_N(\vec{r}_2)\chi_N(\sigma_2) \\ \vdots & \vdots & \ddots & \vdots \\ \psi_1(\vec{r}_N)\chi_1(\sigma_N) & \psi_2(\vec{r}_N)\chi_2(\sigma_N) & \cdots & \psi_N(\vec{r}_N)\chi_N(\sigma_N) \end{vmatrix}$$

A similar treatment to that of Hartree leads to:

$$\langle\Psi|\,\hat{H}\,|\Psi\rangle = -\frac{\hbar^2}{2m}\sum_i \int \mathrm{d}^3r\, \psi_i^*(\vec{r})\nabla^2\psi_i(\vec{r}) \qquad \mathbf{A}$$

$$+ \int \mathrm{d}^3r\, n(\vec{r})V_{\mathrm{ext}}(\vec{r}) \qquad \mathbf{B}$$

$$+ \frac{e^2}{2}\sum_{i,j} \int \mathrm{d}^3r \int \mathrm{d}^3r'\, \frac{\psi_i^*(\vec{r})\psi_j^*(\vec{r}')\psi_i(\vec{r})\psi_j(\vec{r}')}{|\vec{r}-\vec{r}'|} \qquad \mathbf{C}$$

$$- \frac{e^2}{2}\sum_{i,j} \delta_{\chi_i\chi_j} \int \mathrm{d}^3r \int \mathrm{d}^3r'\, \frac{\psi_i^*(\vec{r})\psi_j^*(\vec{r}')\psi_i(\vec{r}')\psi_j(\vec{r})}{|\vec{r}-\vec{r}'|} \qquad \mathbf{D}$$

where the the energy terms are identified as: $\mathbf{A}$ kinetic energy; $\mathbf{B}$ energy due to the external potential; $\mathbf{C}$ the "Hartree" energy; and $\mathbf{D}$ the "exchange" energy. This exchange energy term leads to a non-local potential that acts on ψ_i at all $\vec{r}'$, and gives rise to an integral-differential equation, which is more computationally intensive to solve than the Hartree approximation.

The eigenvalues of ψ_i are Lagrange multipliers, and can be interpreted as an approximation to the electron's ionisation energy under the approximate assumption that the other orbitals are unaffected.

The "Hartree" term simplifies to:

$$V_{\mathrm{H}}(\vec{r}) = e^2 \int \mathrm{d}^3 r' \, \frac{n(\vec{r'})}{|\vec{r} - \vec{r'}|} \qquad (2.22)$$

where $n(\vec{r}) = \sum_i \psi_i^*(\vec{r})\psi_i(\vec{r})$ is the full charge density. This realisation leads to the fundamental idea behind density functional theory. If the full wavefunction was used, the amount of memory required to store it grows exponentially with N. For example, if it were represented on a very rough grid, with 3 points per degree of freedom, the amount of memory scales as roughly $\sim 10^{1.5N}$, so for just 50 electrons, $\sim 10^{75}$ values would need to be stored (for comparison, the number of baryons in the observable universe is $\sim 10^{80}$). Instead, in their seminal 1964 work Pierre Hohenberg and Walter Kohn proposed that it is sufficient to avoid the full many-body wavefunction and instead calculate the charge density $n(\vec{r})$ directly [60].

2.6.1   The theorems of Hohenberg and Kohn

Hohenberg and Kohn proposed two theorems for any system of interacting particles in an external potential [60]:

1. The external potential V_{ext} is uniquely determined by the ground state particle density $n(\vec{r})$; i.e. there cannot be two potentials that differ by more than a constant and that give rise to the same ground state density.

2. An energy functional $E[n]$ exists, such that the exact ground state energy is given by the global minimum of $E[n]$, and the ground state density is the density that minimises $E[n]$.

$$\text{i.e.} \quad E_{\text{GS}} = \min_n [E[n]] = \min_n \left[F[n] + \int \mathrm{d}^3r \, n(\vec{r}) V_{\text{ext}}(\vec{r}) \right]$$

$$\text{where} \quad F[n] = \min_{\Phi \to n} \left[\langle \Phi | \hat{T} + \hat{V}_{\text{ee}} | \Phi \rangle \right] \tag{2.23}$$

A major consequence of the first theorem is that since the external potential defines the Hamiltonian, all properties of the system (including the many-body wavefunction) are uniquely determined by its ground state density. The density functional $F[n]$ is universal, in that it depends only on the type of interacting particles, not on the specific problem (V_{ext}), however the exact form of $F[n]$ requires a constrained search over N electron wavefunctions, which is impractical.

Although some approximations for $F[n]$ are known, these explicit functionals of the density are generally thought to be too crude to be very useful. It is noted however that the group of Emily Carter in Princeton has recently made some strides towards an orbital-free DFT based on the Thomas-Fermi equation [61], but this approach is still in its infancy. The more usual solution to the problem of the functional is to use the so-called Kohn-Sham theory.

2.6.2   Kohn-Sham theory

In 1965, Walter Kohn and his colleague Lu Jeu Sham published a practical method to calculate the density by solving a non-interacting Hartree-type problem with the same ground state energy as the interacting system.

From Equation 2.23, the functional $F[n]$ consists of a kinetic energy term $\hat{T}$ and an electron-electron potential energy term $\hat{V}_{\text{ee}}$. These terms are given below in Equation 2.24:

$$F[n] = \underbrace{\langle \Phi_{\text{GS}}| - \frac{h^2}{2m} \sum_i \nabla_i^2 |\Phi_{\text{GS}}\rangle}_{\text{Kinetic energy}} + \underbrace{\frac{e^2}{2} \int \mathrm{d}^3 r \int \mathrm{d}^3 r' \frac{n(\vec{r})n(\vec{r'})}{|\vec{r} - \vec{r'}|}}_{\text{Hartree energy } E_{\text{H}}[n]} + \tilde{E}_{\text{XC}}[n]$$

$$(2.24)$$

The Hartree energy is the largest part of the interaction energy and is known exactly, while $\tilde{E}_{\text{XC}}[n]$ is the "exchange-correlation" energy, which contains all interaction effects beyond the classical Hartree energy, and is expected to be small.

The kinetic energy term is unknown, due to the non-local Laplacian operator. The kinetic energy of one system however, can be calculated exactly; the case of non-interacting electrons. Therefore the kinetic energy can be approximated by a hypothetical non-interacting system with the same density as the interacting system, and the solution can be found by self-consistent iteration.

This process can be succinctly shown by the following equations. The original problem of the energy functional of the interacting system can be

expressed as:

$$E[n] = T_0[n] + \int \mathrm{d}^3r\, n(\vec{r}) \left(V_{\text{ext}}(\vec{r}) + \frac{1}{2} V_{\text{H}}(\vec{r}) \right) + E_{\text{XC}} \tag{2.25}$$

$$\text{where} \quad E_{\text{XC}} = \tilde{E}_{\text{XC}} + (T[n] - T_0[n])$$

where $T_0[n]$ is the kinetic energy of the non-interacting system with the same density.

Similarly, the energy functional of the non-interacting system is given by:

$$E_0[n] = T_0[n] + \int \mathrm{d}^3r\, n(\vec{r}) V_{\text{eff}}(\vec{r}) \tag{2.26}$$

and the effective potential V_{eff} is chosen so that the density of the non-interacting system is equal to that of the interacting one. Applying variational theory to Equations 2.25 and 2.26 results in an expression for the effective potential on the non-interacting system:

$$V_{\text{eff}}[n(\vec{r})] = V_{\text{ext}}(\vec{r}) + V_{\text{H}}[n(\vec{r})] + \frac{\delta E_{\text{XC}}[n]}{\delta n(\vec{r})} \tag{2.27}$$

The ground state energy of the original interacting problem can now be calculated by iteratively solving effectively single-particle equations (Kohn-Sham equations):

$$\left(-\frac{h^2}{2m} \nabla^2 + V_{\text{eff}}[n(\vec{r})] \right) \phi_n(\vec{r}) = \epsilon_n \phi_n(\vec{r}) \tag{2.28}$$

$$n(\vec{r}) = \sum_{n,\text{occ}} \phi_n^*(\vec{r}) \phi_n(\vec{r}) \tag{2.29}$$

However, although its contribution is small, an expression for $E_{XC}[n]$ is still missing. The Kohn-Sham equations are a technically exact method for determining the ground state of the system, and so the exchange-correlation term is where the first approximation arises so far.

A common method used to calculate the exchange and correlation term (and that which is used in Chapter 3) is the local density approximation (LDA):

$$E_{XC}[n] = \int d^3r \, n(\vec{r}) \, \epsilon_{XC}(n(\vec{r})) \qquad (2.30)$$

$$\text{where} \quad \epsilon_{XC}(n) = \epsilon_X(n) + \epsilon_C(n)$$

and $\epsilon_X(n)$ is known exactly for the homogeneous interacting electron gas, and the prefactors in $\epsilon_C(n)$ are calculated numerically using quantum Monte Carlo.

An alternative method is the generalised gradient approximation (GGA):

$$E_{XC}[n] = \int d^3r \, n(\vec{r}) \, \epsilon_{XC}(n(\vec{r}), \nabla n(\vec{r})) \qquad (2.31)$$

Both the GGA and LDA have their strengths and weaknesses, e.g. with the LDA, the geometry of molecules on surfaces tends to be well-described, however their binding energies are underestimated. Similarly the GGA can yield improvements in the binding energies over LDA, but can overcorrect for the lattice constants in solids.

Further improvements can be made by including higher order gradient terms, however at the expense of higher computational demand. The Perdew-

Burke-Ernzerhof formulation of the GGA [62] is used in Chapter 5 to optimise the different molecular conformations.

Some of the most drastic advances in recent years have been the development of DFT with van der Waals corrections included [63]. These come in various flavours [64–68], each with its own strengths and weaknesses, and some are advanced enough to be included in major commercial DFT codes such as VASP [69], however the open questions that remain promise to maintain the vibrancy this field has shown in recent years.

2.6.3   Basis sets and pseudopotentials

In order to solve the Kohn-Sham equations (Equation 2.28), they must be expanded in some basis set and solved as a linear eigenvalue problem, however there are several choices for the basis set: plane waves, local orbitals, or augmented functions.

In general, valence orbital wavefunctions tend to have many oscillations close to the atomic core, in order to maintain orthogonality with core states, however this introduces many Fourier components. A common method to alleviate this complexity is to replace them with a more simple pseudo-wavefunction which matches the real wavefunction beyond a specific cut-off radius, as can be seen in Figure 2.13, and can be represented by a small number of plane waves.

Similarly, the Coulomb potential wells centred on the ionic cores are very deep, and so it is common to use a smooth pseudopotential with the same scattering properties as the real potential. In this work, the augmented-
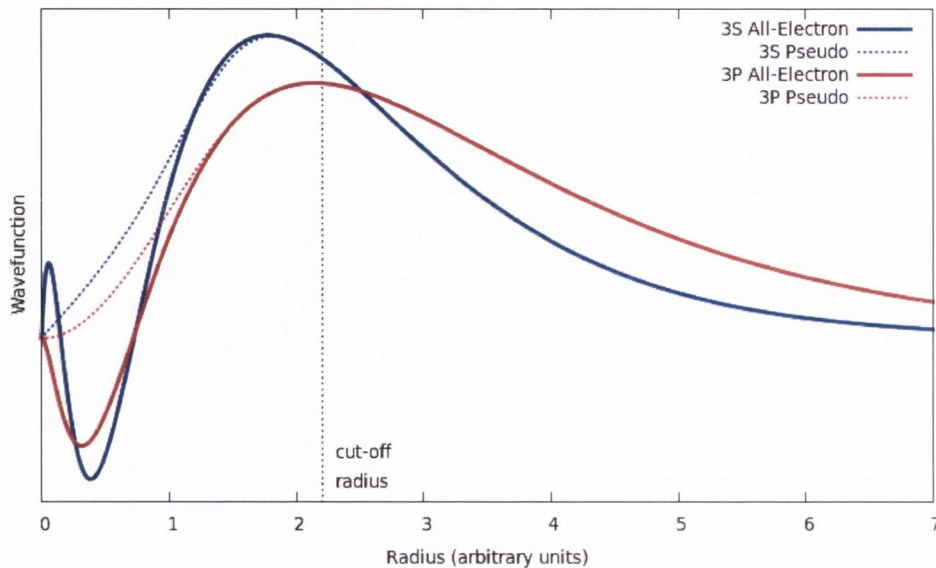
Figure 2.13: Comparison of the 3s and 3p all-electron wavefunctions and pseudo-wavefunctions calculated for Si using the Quantum Espresso package. The pseudo-wavefunctions are shown as dotted lines, and a cut-off radius of 2.2 a.u. was used.

plane-waves method is used with the projected augmented wave (PAW) pseudopotentials [70] included in the Vienna *Ab initio* Simulation Package (VASP).

The construction of accurate, transferable, and ultrasoft pseudopotentials could be the subject of an entire thesis in itself and so will not be described in detail here.

2.6.4   Methfessel-Paxton smearing

Since the Fermi level is the level of the highest occupied energy state of a material, its position determines whether that material is an insulator or conductor. If the Fermi level falls inside a gap in the band structure, that material is an insulator. This means that the density of states smoothly goes

to zero before the band gap, and its $\vec{k}$-integration does not cause problems during calculation. For conductors however, the occupation at the Fermi level is sharp, which makes integration and the use of plane-waves very difficult.

Increasing the number of k-points will cause the Fermi level to oscillate around its exact value, however by allowing k-points to be partially occupied (i.e. through smearing), a smaller number of k-points will yield an accurate band structure.

A symptom of this oscillation is the so-called "charge sloshing" where, for a small band-gap material, the electrons may transfer from a filled energy level to an unoccupied one during one iteration, however this switches the ordering of the levels, and the electrons "slosh" back in the next iteration. This can lead to calculations on small band-gap materials to converge slowly or never converge at all.

To solve this problem, the occupancies of the levels are "smeared out" using Fermi statistics, simulating an artificial temperature. In essence we are calculating the integral over the filled parts of the bands:

$$\sum_n \frac{1}{\Omega_{BZ}} \int_{\Omega_{BZ}} \epsilon_{nk} \Theta(\epsilon_{nk} - \mu) \mathrm{d}k \tag{2.32}$$

which, for a finite number of k-points, becomes

$$\sum_k w_k \epsilon_{nk} \Theta(\epsilon_{nk} - \mu) \mathrm{d}k \tag{2.33}$$

where $\Theta(\epsilon_{nk} - \mu)$ is the Dirac step function (Figure 2.14a). The use of this step function, however, slows down the convergence, as it abruptly jumps

from 0 to 1 at the Fermi level, and so for metals, $\Theta(\epsilon_{nk} - \mu)$ is replaced by

a smooth function $f(\{\epsilon_{nk}\})$ [71]. Using the so-called finite temperature or

Gaussian method, Θ is replaced by the Fermi-Dirac distribution function:

$$f\left(\frac{\epsilon - \mu}{\sigma}\right) = \frac{1}{e^{\frac{\epsilon - \mu}{\sigma}} + 1} \tag{2.34}$$

where σ is the 'smearing' energy, analogous to $k_B T$ in Fermi-Dirac statistics

(Figure 2.14b). It should be noted that this σ is not a physical temperature,

despite the name 'finite temperature method'. For $\sigma \to 0$, $f \to \Theta$, and the

step function is recovered. However, this method gives a non-groundstate

energy, and so σ should be chosen carefully.
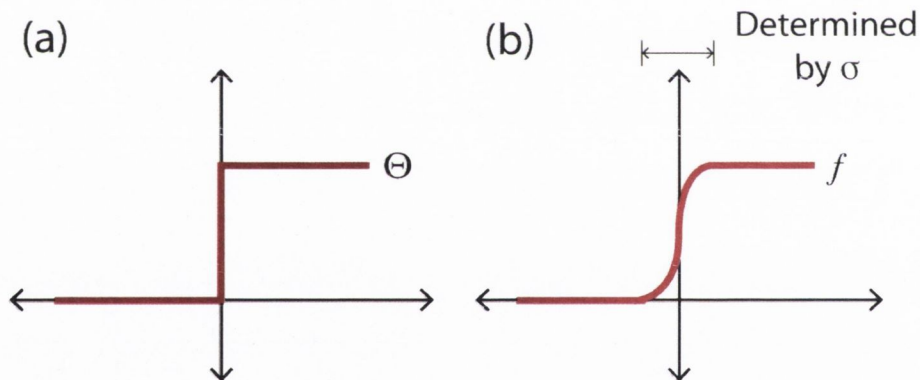
Figure 2.14: **(a)** The sharp Dirac step function Θ and **(b)** the smooth Gaussian function f. The width of the Gaussian function is determined by the smearing energy σ, and for $\sigma \to 0$, $f \to \Theta$.

The method of Methfessel and Paxton solves this problem by expanding

Θ in a complete orthonormal set of Hermite functions, of order N, for which

$N = 0$ recovers the Gaussian approximation [72].

$$\delta(x) \approx D_N = \sum_n^N A_n H_{2n} e^{-x^2} \tag{2.35}$$

where the step function Θ is recast by a delta function $\delta(x)$, and D_N can be integrated to recover the approximation to the step function, and H_{2n} are the even-order Hermite polynomials.

The energy is then replaced by a generalised free energy functional $F = E - \sum_{nk} w_k \sigma S(f_{nk})$, however the entropy term $\sum_{nk} w_k \sigma S(f_{nk})$ is very small for reasonable values of σ. The main drawbacks of the Methfessel and Paxton method are that it can introduce unphysical negative occupations, and increasing the order N introduces extra oscillations into the density of states, which can mask the real features.

Chapter 3

C_{60} on WO_2/W(110): From Self-Assembly to Phase Transitions and Charge States

Much excitement in the field of C_{60} was based on the prospects of using these remarkable molecules for constructing nano-electronic devices [14–20]. However, 25 years have passed since the discovery of C_{60} and these expectations are yet to be fulfilled. The stability of such molecular electronic devices is one of their main drawbacks, and nanomechanical motion can result in the generation of noise in C_{60}-based devices [20]. A natural approach to constructing such devices is through frameworks based on a monolayer of C_{60} molecules.

In this chapter, by using STM, LEED and DFT calculations, we focus on the molecular self-assembly of C_{60} on the WO_2/W(110) surface in the submonolayer to monolayer regimes in order to reveal the conformational

behaviour of C_{60} molecules. DFT is utilised to obtain information about the local density of states.

As the monolayer film is cooled from room temperature down to 78 K, it undergoes two phase transitions which are accompanied by several different types of molecular movement. Close to the first phase transition at 259 K, some molecules switch between at least two charge states, becoming alternately "bright" or "dark" as they gain or lose electrons. These states are elucidated using systematic STM studies, and confirmed by DFT calculations. The results of this work yield important information on the electronic and structural properties of C_{60} molecules adsorbed on the $WO_2/W(110)$ surface.

3.1   Experimental details

All STM experiments were performed using a commercial variable-temperature STM (78–300 K) from Createc GmbH in an in an ultra-high-vacuum (UHV) system consisting of an analysis chamber (with a base pressure of 2×10^{-11} mbar and a preparation chamber (5×10^{-11} mbar). The STM tips were fabricated from [001]-oriented $0.3 \times 0.3 \times 10$ mm^3 single-crystalline tungsten bars by electrochemical etching in 2 M NaOH and cleaned in the UHV chamber by Ar$^+$ ion bombardment [73, 74]. The voltage V_{sample} corresponds to the sample bias with respect to the tip. No drift corrections have been applied to any of the STM images presented in this paper, and all STM images were recorded in the constant-current mode. The experiments were performed in the temperature range of 78–300 K, while the switching phe-

nomenon, over the time scale of the experiment, was observed in the temperature range of 220–260 K. The acquisition time of 10 ms per point was used to measure the time-evolution of the distance between the STM tip and the surface. All STM images were analysed using the software package WSxM [56].

A W(110) single crystal, prepared at the Institute of Solid State Physics, Russian Academy of Sciences, was used as the substrate. An atomically-clean W(110) surface was prepared by *in situ* annealing at 1900 K in an oxygen atmosphere of 1×10^{-7} mbar, followed by a series of high temperature flashes at 2200 K. The sample was heated by electron beam bombardment and temperatures were measured using an optical pyrometer (Ircon UX20P, emissivity 0.35). The clean W(110) surface was verified by LEED and STM before oxidation. Once a clean surface was obtained, the sample was oxidised at 1600 K in an oxygen atmosphere of 1×10^{-6} mbar for 60 minutes. The quality of the resulting oxide structure was verified by LEED and STM before the deposition of C_{60} molecules.

C_{60} (Aldrich Chemicals) was evaporated in the preparation chamber isolated from the STM chamber at a rate of about 0.2 ML (monolayer) per minute from a deposition cell operated at a temperature of approximately 700 K. Before evaporation, the C_{60} powder was degassed for about 8 hours to remove water vapour. The total pressure during C_{60} deposition was in the 1×10^{-9} mbar range and the substrate was kept at room temperature [46].

The WO_2/W(110) surface was covered with monatomic steps and terraces up to 50 nm in width. Oxide rows and monatomic steps were used to calibrate the STM scanner in the variable temperature experiments. The height from

the substrate surface to the molecules' centers was 5 Å, as measured by STM of the fullerene film thickness at the edges of the closed C$_{60}$ layer.

In order to determine which part of the static and spinning C$_{60}$ molecules face the WO$_2$/W(110) surface, density functional theory (DFT) simulations of the partial charge distribution of electron states were performed in collaboration with Dr Olaf Lübben, whose work and expertise are gratefully appreciated and acknowledged. Density of states (DOS) calculations were performed using the Vienna *Ab initio* Simulation Package (VASP) program. VASP implements a projected augmented basis set (PAW) [70] and periodic boundary conditions. The electron exchange and correlation was simulated by local density approximation (DFT-LDA) pseudopotentials with a Ceperley-Alder exchange-correlation density functional [75]. A Γ-centred (2 × 2 × 1) k-point grid was used for all calculations to sample the Brillouin zone. The applied energy cut-off was 400 eV. The global break condition for the electronic self-consistent loops was set to a total energy change of less than 1×10^{-4} eV. For the DOS a smearing of 0.2 eV was applied using the Methfessel-Paxton method [72].

3.2   C$_{60}$

The fabrication of complex organic molecular structures on technologically important substrates held together by weak and reversible van der Waals interactions, hydrogen bonds or electrostatic interactions has been a much-investigated topic in the past ten years [9–11, 76–82]. This controlled self-assembly of organic nanostructures offers a number of powerful approaches

for the development of organic molecule-based devices, which possess functions such as rectifying, switching and sensing [10, 11, 15, 76–81, 83, 84].

Fullerenes in particular have attracted considerable attention in recent years due to their potential in surface chemistry and nanotemplating [84], non-linear optics [84, 85], single-molecule transistors [15, 20], and especially molecular electronics because of their tuneable electronic properties, resulting in superconducting or semiconducting behaviour [15, 86, 87].

The formation and characterisation of fullerene adlayers on surfaces are of great interest from the fundamental and technological points of view because they provide valuable information about molecular interactions and can lead to potential applications in existing technologies.

The study of these surface-supported systems is important for future developments in molecular electronics, since they represent promising materials for applications in advanced nanopatterning, surface templating, molecular data storage, solar cells, sensors/molecular recognition and functional surfaces [14, 15, 20, 22, 84–88].

Of particular interest are the nature of the bonding between the fullerene molecules and the substrate, as reflected in the electronic charge distribution and their geometric configuration at the interface, and the dynamics of electron-hole transfer between the molecule and the metal or semiconductor surface. This information can be obtained by using a combination of scanning tunneling microscopy and theory (STM and DFT).

STM is a highly local technique that has become a powerful tool for studying the adsorption geometry and the conformation and dynamics of single organic molecules and molecular assemblies on conducting substrates [9–

11, 76–82]. Over the last decade STM has been used intensively for the study of C_{60} self-assembled layers on a variety of metal [18, 24–37] and semiconductor [22, 38–42] surfaces.

On most surfaces fullerene molecules self-assemble into close-packed monolayers with a hexagonal or quasi-hexagonal structure and a molecule-molecule separation close to 1 nm, as observed in bulk C_{60} [18, 22, 24–27, 29–39, 42, 89]. In some cases the formation of a C_{60} monolayer leads to an adsorbate-induced reconstruction of the substrate [25, 30–37].

Surprisingly, only few studies of C_{60} on metal oxide surfaces have been performed to this end [43–45]. This is despite the fact that metal oxide surfaces and thin films have many potential applications in existing technologies [90–93] and may be used as nanostructured templates with preformed surface patterns [94–97] for molecular self-assembly.

The choice to study the combination of C_{60} and $WO_2/W(110)$ in this work was motivated in part by the expertise present in the research group. Dr Kevin Radican had recently described the $WO_2/W(110)$ surface in detail [94], and the width of the oxide nanorows (~2.5 nm) was expected to lead to some interesting templating behaviour of adsorbates. Similarly, Dr Sergey Krasnikov joined the group and brought with him vast experience on molecular self assembly, and so C_{60} was chosen as a test molecule about which a large amount was known from the literature. It was expected that C_{60}'s dynamic behaviour could be explored by controlling the temperature, which could give insights into fundamental physical processes.

C_{60} has been well studied on many metal surfaces, and some common properties and differences can be derived from past research. Arguably the

most studied C_{60}/metal system is C_{60} on Cu(111) [37, 98–102]. The Cu(111) lattice and that of solid C_{60} have only a small 2% lattice mismatch, making the substrate ideal for the growth of films. Detailed theoretical calculations show that the most stable adsorption site on Cu(111) is the so-called "hcp" hollow site, with the hexagon facing down (h-orientation, see below) [99, 100]. However the hcp (h-orientation), fcc (p-orientation, pentagon facing down) and bridge (h or p) sites of the close-packed surface are very close in energy, leading to a very high C_{60} mobility when the molecules have rotational and translational motion [98]. This leads to a hexagonal close-packed monolayer formed on the surface [101, 102].

Upon the formation of a monolayer, the Cu surface is reconstructed, with the Cu–Cu bonds closest to the C_{60}'s bottom hexagon elongating and forming a nanopit. In turn the short and long C–C bonds of the bottom hexagon extend by 3% and 2%, respectively [98]. This assembly is accompanied by a charge transfer of 1.5–2 electrons/C_{60} from the surface to the molecules as measured by NEXAFS [103, 104].

Interestingly, when a monolayer of C_{60} is deposited on a thin layer of Cu, the sheet resistance of the system is decreased, however when deposited on a thick Cu layer, its sheet resistance is *increased* [105]. The explanation for this is that the thick Cu is a good conductor, and the presence of the molecule/metal interface introduced extra scattering processes, causing the conductance to suffer.

Gardener *et al.* have studied the dynamics of a monolayer of C_{60} on the noble Au(111) surface [25]. They observed that some molecules appeared darker than others in the monolayer, and the amount of dark molecules

appeared to be correlated to the registry of the overlayer with the substrate.
Figure 3.1a shows a characteristic image of a quasi-periodic domain. The
two bright features highlighted by arrows show the $22 \times \sqrt{3}$ "herringbone"
reconstruction underneath the C_{60} layer, however these two isolated regions
are all that remain of the original $22 \times \sqrt{3}$ structure, indicating that the C_{60}
layer has lifted the reconstruction over the majority of the surface.
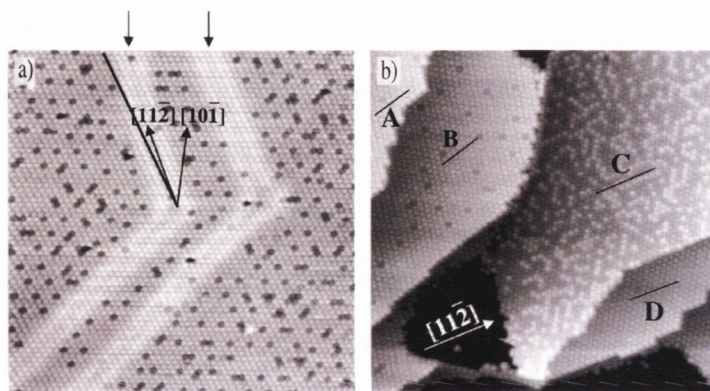
Figure 3.1:   Room temperature STM of C_{60} monolayer domains on the
Au(111) surface. (a) Quasi-periodic domain of bright and dim C_{60}, with
two "herringbone" features indicated by arrows, emphasising that this re-
construction has been lifted over the rest of the surface. (b) Several different
C_{60} domains, with their primary axes indicated by black lines, showing that
the only obvious difference between them is their orientation [25].

Figure 3.1b illustrates several different domains $A - D$ within a post-
annealed C_{60} monolayer on the Au(111) surface. These domains are char-
acterised by the arrangement of "dim" C_{60} molecules which have a lower
apparent height than other C_{60}. D shows a domain with a uniform appar-
ent height, whereas domains A and B exhibit the so-called quasi-periodic
structure of dim C_{60} molecules, and C demonstrates a disordered structure.

The fundamental difference between these domains is the angle made be-
tween the primary directions of the C_{60} overlayer and the crystallographic

directions of the substrate, as indicated by solid black lines in Figure 3.1b. C and D are aligned along the $[11\bar{2}]$ direction of the Au(111) surface, implying a strong correlation between the uniform and disordered regions of the monolayer, whereas A and B are offset by an angle of 16° from this direction. This is indicative of a 7×7 R14° superstructure for these domains, as shown in Figure 3.2, where every seventh C_{60} molecule occupies the same Au lattice site, giving rise to the quasi-periodicity observed in A and B.
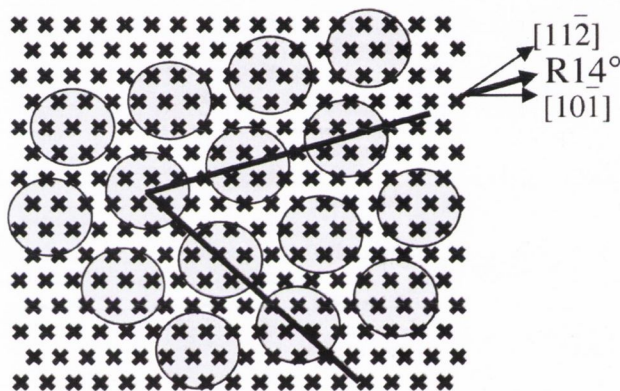
Figure 3.2: Schematic of the 7×7 R14° superstructure of C_{60} on Au(111) proposed to explain the quasi-periodic structure of domains A and B [25].

The apparent height differences between individual molecules in each domain exhibit a dynamic behaviour, with many molecules switching between high, medium and low states. This switching has been attributed to charge transfer occurring between the C_{60} molecules and the Au substrate, with such transfer accommodated by nanopits forming via substrate reconstruction.

Early work on C_{60} adsorption on Ag(111) disagreed on its binding and absorption sites, with the group of Eric Altman proposing the p-orientation C_{60} on the on-top site [106, 107], and Takayasu Sakurai showing the favoured adsorption as the h-orientation on the hollow site [101]. Time has borne out

the latter interpretation, with numerous theoretical [98] and experimental works [108–110] and confirming that the hollow site model has the lowest energy, however with some dynamical behaviour observed by STM [108].

Similar to the case on Au(111), C_{60} causes the Ag(111) surface reconstruction to change position over time [108–110]. This is represented as an apparent contrast between some C_{60}. Such contrast is observed to switch over time in a correlated fashion at room temperature. This behaviour is explained by the mass transport of Ag atoms along the surface, i.e. at one point C_{60} will be sitting on-top of a Ag atom, and during the next scan the surface atoms have shifted and it will be sitting in a hollow site. Although the hollow site has the lowest energy, the on-top site with the hexagon-hexagon C–C bond (h–h) facing the substrate is only slightly higher in energy, and from the temperature dependence of the switching rate, an energy barrier of 0.84 eV has been derived between the two states [108].

This dynamical behaviour on noble metal surfaces is well-understood and indeed a recent study asserted that it appears that "interface reconstruction of close-packed metal surfaces induced by large-molecule C_{60} adsorption is the rule rather than the exception" [110], however as will be shown in Section 3.6, the results on $WO_2/W(110)$ do not support substrate reconstruction, instead the ultrathin O–W–O trilayer decouples the C_{60} organic layer from the metallic substrate, allowing the charge-states to have a finite lifetime without the need for surface reconstruction.

In contrast to the high-mobility, van der Waals-bound systems discussed so far, when deposited on Pt(111), C_{60} is very strongly bound and immobile [111]. At room temperature (300 K), the Pt surface catalyses the poly-

merisation of the C$_{60}$, and at higher temperatures ($\sim$1050 K) the molecules decompose [112]. Similarly on Pt(110), there is a strong interaction with the surface, with C$_{60}$ lifting the so-called "missing-row" reconstruction, and forming a dumbbell-shaped nanowire array above 700 K [113]. Decomposition is also observed on Ni(110) with a carbon layer formed at about 760 K, transforming into graphitic carbon at higher temperatures [37, 111, 114].

On semiconductor surfaces the molecules can be even more strongly bound, however studies of C$_{60}$ on Si(001)-(2 $\times$ 1) and Si(111)-(7 $\times$ 7) show only physisorption until the systems are annealed up to 670 K, at which temperatures strong covalent bonds are formed [115–117]. Decomposition to SiC is observed when the temperature is increased above 1000 K.

Nakaya *et al.* [22] have demonstrated data storage on the molecular scale using a trilayer of C$_{60}$ molecules prepared on the passivated Ag/Si(111)-$\sqrt{3} \times \sqrt{3}$ R30° substrate. By controlling the bias voltage of the STM tip, it was shown that the C$_{60}$ in the overlayers could be induced to form dimer and trimer structures, which were visible as dark depressions in the formerly pristine close-packed structure of the film (Figure 3.3).

It was also shown that the induced depressions could be repaired by pulsing with a bias voltage of opposite polarity, and the process could be repeated multiple times with no adverse effects on the C$_{60}$ molecules (Figure 3.4).

Finally, the few studies of C$_{60}$ on metal oxides thus far have focussed on either SrTiO$_2$ [43] or TiO$_2$ [44, 45]. On TiO$_2$(110), C$_{60}$ grows in an island fashion, with each C$_{60}$ bridging a groove between two oxygen rows [44]. Although the rutile TiO$_2$ surface is inherently defective, the C$_{60}$ overlayer is quite free of defects, indicating a stronger molecule–molecule interaction
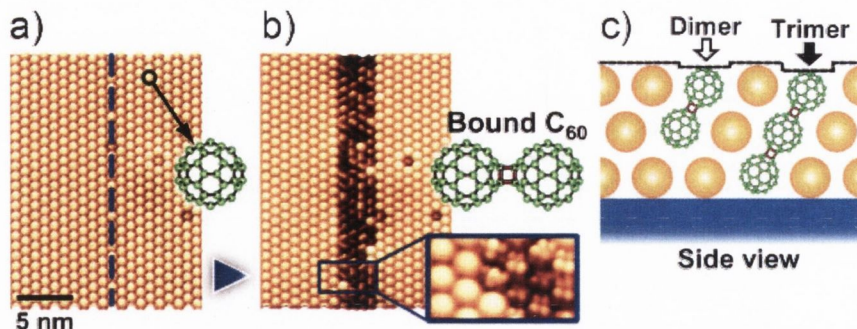
Figure 3.3: **(a)** Pristine C$_{60}$ trilayer on Ag/Si(111)-$\sqrt{3} \times \sqrt{3}$ R30°. **(b)** After scanning the tip along the dotted line at $60 \, \text{nm s}^{-1}$ with a sample bias of $-3.5 \, \text{V}$, a dark line of bound C$_{60}$ is formed. **(c)** Schematic of dimer and trimer formation [22].
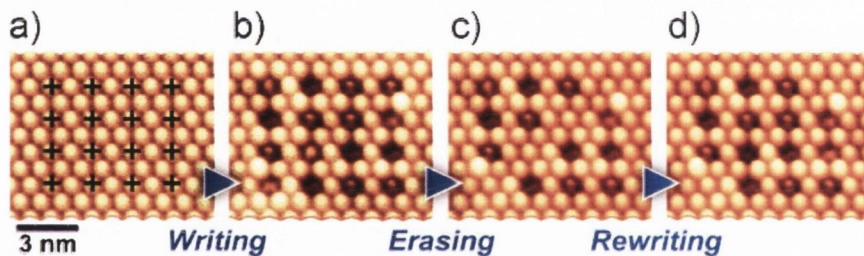
Figure 3.4: STM of C$_{60}$ trilayer showing single-molecular writing **(a)** to **(b)**, erasing **(b)** to **(c)** and rewriting **(c)** to **(d)** [22].

than the molecule–substrate interaction, with images of isolated molecules very rare.

In summary, C$_{60}$ has been widely studied on a range of metal, semiconductor and metal oxide surfaces, several of which show an apparent contrast between some molecules, attributed to either surface reconstruction or molecular polymerisation, however it will be shown in the following sections that the contrast observed on WO$_2$/W(110) cannot be attributed to either of these explanations, and instead is due to charge transfer to the C$_{60}$ molecules.

3.2.1 Possible C$_{60}$ orientations

Although C$_{60}$ is a spherical molecule, it is not completely symmetric, in that it has discrete faces, bonds and atoms, and so when it is deposited onto a surface, five different high-symmetry orientations are possible, as shown in Figure 3.5. When the 6 or 5 atoms in either a hexagonal or pentagonal face of the molecule is directed towards the surface, that orientation will be designated **h** or **p**, respectively. Similarly two atoms can form either the border between two hexagons (**h–h**) or a hexagon and a pentagon (**h–p**). Finally, each of the C$_{60}$'s 60 carbon atoms are identical, so if the molecule faces the surface by a single atom it is designated **s**. The final panel in Figure 3.5 shows the relationship between the faces and bonds in one half of the C$_{60}$ molecule.

3.3 WO$_2$/W(110)

The high-temperature oxidation of W(110) results in the formation of a thin, strained-commensurate WO$_2$(010) structure at the surface [94]. A typical STM image and a LEED pattern taken from the WO$_2$/W(110) surface are shown in Figures 3.6a and 3.6b, respectively.

WO$_2$(010) has an O–W–O trilayer structure and forms well-ordered oxide nanorows separated by 2.5 nm on the surface (Figure 3.6a). These rows appear as bright regions with dark depressions in between. The atomic structure of the WO$_2$ overlayer is shown in Figure 3.7. The trilayer structure can be clearly seen in the side view schematic, looking along the [001] direction of the substrate.
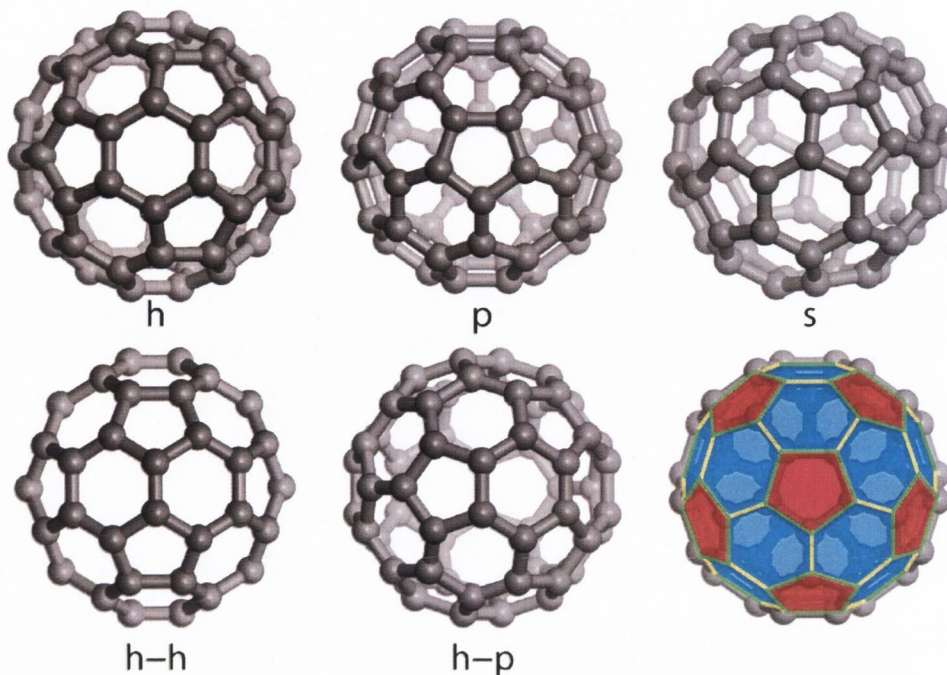
Figure 3.5: The high-symmetry orientations of C$_{60}$ are shown, and are labelled according to the part of the molecule which is facing up; **h** hexagon, **p** pentagon, **s** single atom, **h–h** bond between two hexagons, **h–p** bond between a hexagon and a pentagon. The sixth panel shows all the bonds and faces colour coded; p red, h blue, h-h yellow, h-p green.

The LEED pattern (Figure 3.6b) shows characteristic satellite spots around each primary W(110) spot, representing two equivalent overlayer domains on the surface. The WO$_2$ nanorows follow either the $[\bar{3}37]$ or the $[\bar{3}3\bar{7}]$ directions of the W(110) substrate depending on the domain [94]. The WO$_2$ overlayer has an oblique unit cell with vectors $a = 2.5$ nm and $b = 1.3$ nm, as obtained by STM and confirmed by LEED, shown on Figure 3.6a as a green parallelogram.

The presence of oxide nanorows can influence the growth of a C$_{60}$ molecular overlayer, and so the WO$_2$/W(110) surface has been chosen as an interesting nanostructured template for their self-assembly.
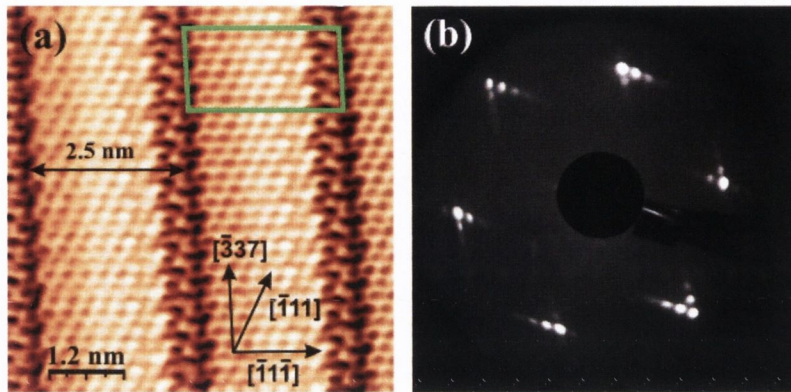
Figure 3.6: **(a)** Low-temperature STM image of the WO$_2$/W(110) surface: $V_{sample} = -0.06$ V, $I_t = 0.10$ nA, size 6.5 nm × 6.5 nm, 78 K. The green parallelogram shows the oxide's oblique unit cell with dimensions $a = 2.5$ nm and $b = 1.3$ nm. **(b)** LEED pattern from the WO$_2$/W(110) surface, acquired at a primary beam energy of 70 eV

3.4 Growth and topography of the C$_{60}$ film

At a very low coverage (0.2 ML), C$_{60}$ molecules start nucleating at the inner step edges of the WO$_2$/W(110) surface (see Figure 3.8a), which provides evidence for a weak molecule-substrate interaction and for the diffusion of the molecules on the surface at room temperature. C$_{60}$ molecules appear as bright protrusions in the STM images and decorate the substrate's inner step edges, forming molecular chains. The tungsten oxide nanorows of the underlying substrate are also visible (Figure 3.8a).

At intermediate coverages (0.4–0.7 ML), C$_{60}$ molecules self-assemble at room temperature into compact two-dimensional islands with a hexagonal close packed structure (see Figure 3.8b). The C$_{60}$ molecular layer is incommensurate with the WO$_2$/W(110) substrate. However, the growth of the C$_{60}$ overlayer starts from the substrate's inner step edges, which follow the [$\bar{1}$11] direction on the surface. This behaviour causes one of the primary
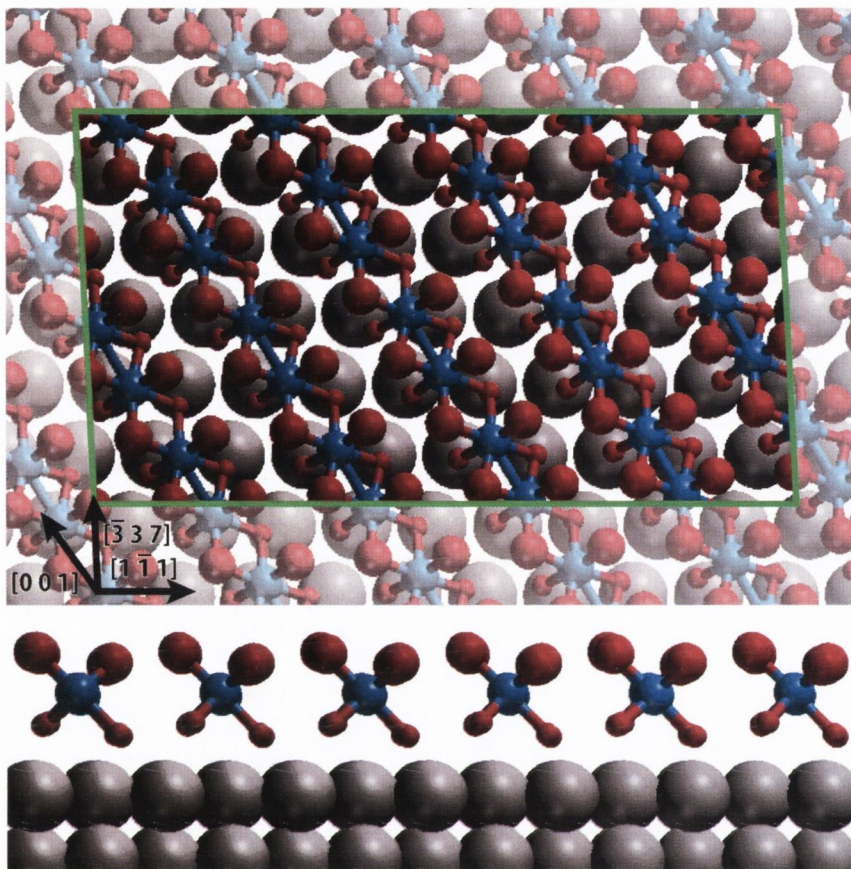
Figure 3.7: Top and side view of the WO$_2$/W(110) surface. Red atoms indicate oxygen, with the large atoms forming the topmost layer. Blue atoms represent the tungsten sandwiched in the WO$_2$ trilayer, and grey atoms make up the W(110) surface. The side view is looking along the [001] direction of the W(110) surface, parallel to the W–W short bonds in the oxide. The green parallelogram highlights the unit cell of one nanorow.

directions of the molecular layer to coincide with the [$\bar{1}$11] direction of the WO$_2$/W(110) surface. This is a clear indication that the substrate plays a certain role in the adsorption and arrangement of the molecules. The angle between this direction of the C$_{60}$ layer and the [$\bar{3}$37] direction of the oxide nanorows is equal to 23°.
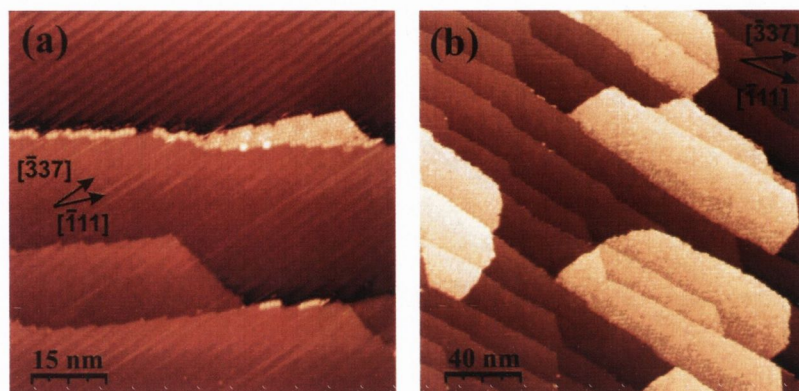
Figure 3.8: **(a)** Low-temperature STM images acquired after the deposition of 0.2 ML and **(b)** 0.5 ML of C_{60} molecules onto the $WO_2/W(110)$ surface. (a) $V_{sample} = 1.0\,\text{V}$, $I_t = 0.10\,\text{nA}$, size 76 nm $\times$ 76 nm, 78 K. (b) $V_{sample} = 1.0\,\text{V}$, $I_t = 0.10\,\text{nA}$, size 200 nm $\times$ 200 nm, 78 K.

The intermolecular bonding that occurs through the C_{60} π-electron system appears to be stronger than the molecule-substrate interaction, leading to the formation of such compact islands. This is confirmed by the fact that there are no single C_{60} molecules adsorbed in the middle of substrate terraces after deposition, indicating a high mobility of the individual molecules on the surface at room temperature. Furthermore, each $WO_2/W(110)$ substrate terrace is covered with a single molecular domain, with terrace widths of up to 40 nm, and domain boundaries are rarely observed. The distribution of the C_{60} among the substrate terraces is not homogeneous at this coverage – some terraces have almost no C_{60}. This indicates that C_{60} molecules can easily cross substrate step edges while moving on the surface as a result of inter-terrace diffusion.

At approximately 1 ML coverage, the molecules form large domains whose width is limited only by the width of the $WO_2/W(110)$ substrate terraces. One molecular monolayer is defined as the case in which the substrate is

completely covered by molecules such that if one further molecule is added, it will have no direct contact with the substrate and will form a second layer. For the C_{60} monolayer on the $WO_2/W(110)$ surface, the molecular packing density is 1.25 C_{60} molecules per $1\,nm^2$.
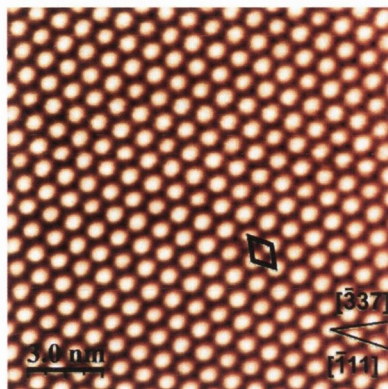
Figure 3.9: $V_{sample} = -1.5\,V$, $I_t = 0.13\,nA$, size 15.4 nm × 15.4 nm. The unit cell of the C_{60} lattice is shown in black and has the following parameters: the unit cell vectors are each equal to $0.95 \pm 0.05\,nm$, and the angle between them is $60.0 \pm 0.5°$. This image has been smoothed using a 3 × 3 matrix to remove mechanical noise.

The unit cell of the C_{60} lattice (shown in black in Figure 3.9) contains a single C_{60} molecule and its unit cell vectors are each equal to $0.95 \pm 0.05\,nm$, with an angle between them of $60.0 \pm 0.5°$, forming a hexagonal close-packed structure. The intermolecular separation within the overlayer is very close to the natural molecule-molecule distance of 1 nm observed in bulk C_{60} crystals. The formation of ordered domains of such an extent and the C_{60}–C_{60} separation further indicate the presence of a significant intermolecular interaction, as well as a low diffusion barrier for the molecules on the $WO_2/W(110)$ surface at room temperature. Thus, C_{60} molecules are physisorbed on this sur-

face and a weak molecule-substrate interaction occurs through the molecular π-electron system.

At some voltage biases, the C_{60} molecules on the $WO_2/W(110)$ surface show a significant difference in apparent height (see Figure 3.10a), which can be a reflection of local electronic and/or topographic variations.
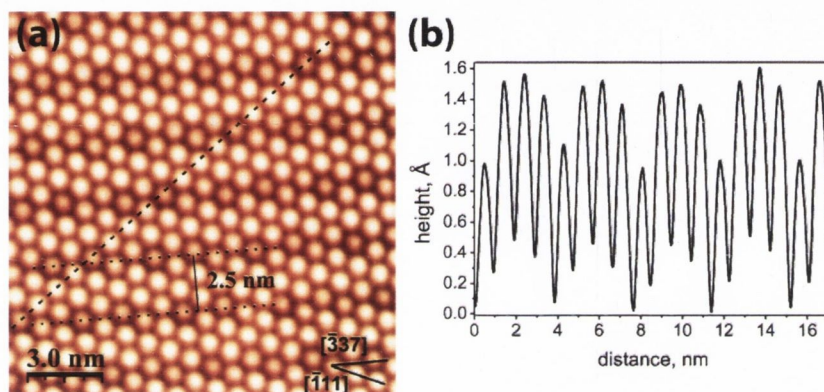
Figure 3.10: **(a)** STM image of C_{60} on the $WO_2/W(110)$ surface, showing chains of the 'dim' molecules, which occupy the grooves between the oxide nanorows of the $WO_2/W(110)$ surface: $V_{sample} = -0.7\,\mathrm{V}$, $I_t = 0.3\,\mathrm{nA}$, size $15.6\,\mathrm{nm} \times 15.6\,\mathrm{nm}$. Dotted lines separated by $2.5\,\mathrm{nm}$ indicate the $[\bar{3}37]$ direction of the nanorows. **(b)** A line profile (along the dashed line in (a) indicating the height difference between the 'bright' and 'dim' C_{60} across the nanorows.

These so called 'bright' and 'dim' molecules have been previously observed by STM on a variety of surfaces and are often attributed to C_{60}-induced substrate reconstructions [25, 30–37]. Such surface reconstructions can lead to two topographically different C_{60} adsorption sites, where 'dim' C_{60} molecules are sunk into nanopits of the reconstructed substrate, and are lower in height than 'bright' ones. Other explanations suggest that this apparent height difference is due to electronic and molecular orientation effects [106, 118]. From Figure 3.10a it is clearly seen that the 'dim' C_{60}

molecules on the $WO_2/W(110)$ are arranged in dark chain-like structures. The distance between these chains is equal to $2.5\,nm$ as observed by STM.

From STM images it is clear that the 'dim' C_{60} molecules follow the oxide nanorows of the substrate and are adsorbed between them. The nanostructured $WO_2/W(110)$ surface exhibits grooves separated by $2.5\,nm$ [94], which are seen as dark depressions in the STM image (Figure 3.6a). The 'dim' C_{60} molecules observed in Figure 3.10a occupy these grooves, and are situated slightly lower than the others ('bright' C_{60}). The line profile shown in Figure 3.10b indicates that the height difference between the 'bright' and 'dim' C_{60} molecules is equal to approximately $0.6\,\text{Å}$. The same value of corrugation was observed for oxide nanorows forming the $WO_2/W(110)$ surface [94], indicating that such an apparent height difference between C_{60} molecules is due to the substrate topography.

Furthermore, a similar apparent height difference in the range of 0.4–$1.0\,\text{Å}$, attributed to an adsorbate-induced reconstruction of the substrate, has been observed between 'bright' and 'dim' C_{60} molecules on other surfaces and was explained by an adsorbate-induced reconstruction of the substrate [25, 30, 33–35]. However, there is also the possibility of a slightly different interaction between the $WO_2/W(110)$ surface and the electron orbitals of the 'dim' C_{60} molecules, caused by their specific arrangement on the surface, which results in proximity of the molecule to the W layer.

Low-temperature STM of C_{60} molecules performed at $78\,K$ demonstrates well-resolved molecular orbitals within individual molecules. It was not possible to resolve these orbitals by performing STM at room temperature. This
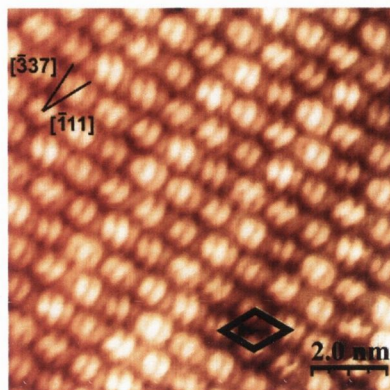
Figure 3.11: Low-temperature STM image of C_{60} on the $WO_2/W(110)$ surface, showing that most of the C_{60} molecules have the same orbital appearance, and hence the same orientation on the substrate at 78 K: $V_{sample} = 0.9\,V$, $I_t = 0.70\,nA$, size 10 nm × 10 nm, 78 K. The unit cell of the C_{60} overlayer is shown in black.

is due to movement (rotation) of the molecules within the layer at this temperature, and will be discussed further in the following Sections 3.5 and 3.6.

At 78 K however, most of the molecules in the complete C_{60} monolayer on the $WO_2/W(110)$ surface exhibit the same internal stucture, and are rotated approximately in the same direction due to interactions with the substrate and the suppression of molecular movement at such a low temperature. This is shown in Figure 3.11 by the ordered molecular orbitals (lobes) of individual C_{60}. The molecules appear on the STM image as spheres composed of three 'stripes' (molecular lobes), suggesting that the same part of each C_{60} molecule is facing the substrate. The similar appearance of most of the C_{60} on the $WO_2/W(110)$ surface indicates that the molecule-substrate interaction is strong enough to align the molecules at low temperature, when their movement is suppressed.

Similar parallel orientation of C_{60} molecules has been previously observed on certain other surfaces by low-temperature STM [28, 30, 33, 34, 89]. It is noted that STM images exhibiting three molecular lobes within an individual C_{60} molecule have been acquired at a sample bias in the range from 0.7–1.0 V (0.9 V in Figure 3.11). At such a voltage, electron tunneling occurs into the lowest unoccupied molecular orbital (LUMO) of C_{60}, making the LUMO responsible for the 'three-stripe' appearance of C_{60} molecules on the $WO_2/W(110)$ surface. C_{60} molecules exhibiting three 'stripes' have been previously observed by STM on different metal and semiconductor surfaces [25, 31, 32, 41, 119, 120]. In most of these cases the proposed C_{60} orientation was the one in which the carbon-carbon bond that forms the border between two adjacent hexagons of C_{60} (h–h bond) is parallel to the substrate [31, 32, 41, 119, 120].

3.5   Rotational transitions in the C_{60} thin film

The study of phase transitions in two-dimensional (2D) systems is an active area of research due to their potential applications, such as improving the performance of liquid crystal opto-electronic devices [121] and high-T_C superconductors [122, 123], and determining the thermodynamic properties of nanoparticles [124]; and also due to the fundamental physics at play such as the crystal structure of novel intermetallic compounds [125]. There are major differences between phase transitions in 2D and 3D systems [126–129]. For example, melting in 3D crystals is always a first order transition, whereas in 2D systems this is not necessarily the case.

In the close-packed, two-dimensional layer of C_{60} molecules, individual molecules are weakly bonded to their nearest neighbors. If each molecule in such a monolayer could be addressed individually, this could provide the basis for a device with an ultra-high element density. The properties of such devices are determined by the behavior of both the individual molecules and the C_{60} layer as a whole.

The unique properties of fullerenes and fullerene-based compounds result from the structure and shape of the C_{60} molecule. The symmetry of the molecule and its deviations from a uniform spherical shape give it rotational degrees of freedom, which often determine the physical properties of C_{60} compounds, C_{60}-based clusters, 2D layers and the 3D crystal. At room temperature, C_{60} molecules arranged in a face-centred cubic lattice (FCC) undergo rapid rotation around their centers of mass. The typical time for a single molecular rotation is in the range of 3 picoseconds [130].

Below 259 K, however, ordering occurs, resulting in a change of space group symmetry from FCC to simple cubic [131–133]. Neutron scattering studies [132, 134] have shown that between 90 K and 259 K, C_{60} molecules in the 3D crystal shuffle between two nearly degenerate orientations, which differ in energy by 11 meV. The orientations are separated by an energy barrier of 290 meV [135, 136].

There is a glassy transition in the 3D crystal at 90 K, resulting from a freezing of the molecules' hopping between the two orientations [137]. The relaxation time is estimated to be about 1 day at 90 K [138, 139]. The relaxation process around the glassy transition can be fitted by a non-exponential function $\exp\{-(t/\tau)^\beta\}$ [137], where $\beta = 0.94$ [139]. The deviation of the

relaxation dependency from a simple exponential ($\beta = 1$) curve provides
evidence for significant interaction between the molecules.

The rotational phase transition in an 80 nm, single-crystalline C_{60} film de-
posited on GaAs(111) has been previously studied by X-ray diffraction [140].
The results of these measurements reveal an anomaly in the lattice parame-
ter at the phase transition temperature $T_C = 240$ K, 19 K below that of the
bulk C_{60} crystal. This difference was attributed to a strain effect in the C_{60}
film introduced by the substrate.

Mean field theory has been used to model the interactions of solid C_{60},
both at the surface of the crystal and in the bulk, and these calculations have
been confirmed by experimental results. In solid C_{60}, melting of the orien-
tational order starts from the top layer of the surface. Lu *et al.* [138] and
Lamoen and Michel [141] have each modelled the interactions in bulk C_{60}
using mean field techniques, and were able to reproduce the experimentally-
observed crystal symmetries, including the phase transition from a low-
temperature simple cubic structure to a disordered face-centred cubic struc-
ture at 260 K.

Passerone and Tosatti [142], and Laforge *et al.* [143] later built upon these
models to describe the rotational surface disordering phase transition for the
(111) surface of solid C_{60}, for which three separate phases are predicted and
observed. Below 150 K, the surface has (2×2) symmetry. Three molecules in
the surface (2×2) unit cell have only a twofold axis normal to the surface. The
fourth, more frustrated molecule has instead its threefold axis normal to the
surface. Between 150 K and 230 K, the surface symmetry is still (2×2), but

the more frustrated molecule begins to rotate, and above 230 K, all surface molecules are in the disordered state, with (1 × 1) surface symmetry.

This section is focused on the link between an individual molecule's transitions between different states and the phase transition of a statistical ensemble of C$_{60}$ molecules forming a single molecular layer on the WO$_2$/W(110) surface in the temperature range between 78 K and 320 K. A rotational phase transition at 259 K and a kinetic glassy transition at 220 K have been observed. A good agreement between the parameters of the observed rotational transitions and those predicted from the properties of individual C$_{60}$ molecules has been found.

3.5.1   Temperature dependence

At low temperatures (below 220 K), STM images of individual molecules reveal an orbital structure that is determined by the orientation of the C$_{60}$ molecule (Figure 3.12a, b). The arrangement of the molecular orbitals depends on the cooling regime. When the sample was quenched with a cooling rate of 10 K/min, it formed the orbital structure presented in Figure 3.12a. This structure is characterized by a random orientation of C$_{60}$ molecules forming a glassy, metastable state. No correlations between the individual orientations of neighboring C$_{60}$ molecules have been found.

The orbital arrangement shown in Figure 3.12b was realized by slowly cooling the film, at a rate of 100 K/day, from 300 K down to 78 K. The molecular orbitals of individual C$_{60}$ appear in the STM image of the orbital-correlated state as stripes aligned in approximately the same direction (Fig-
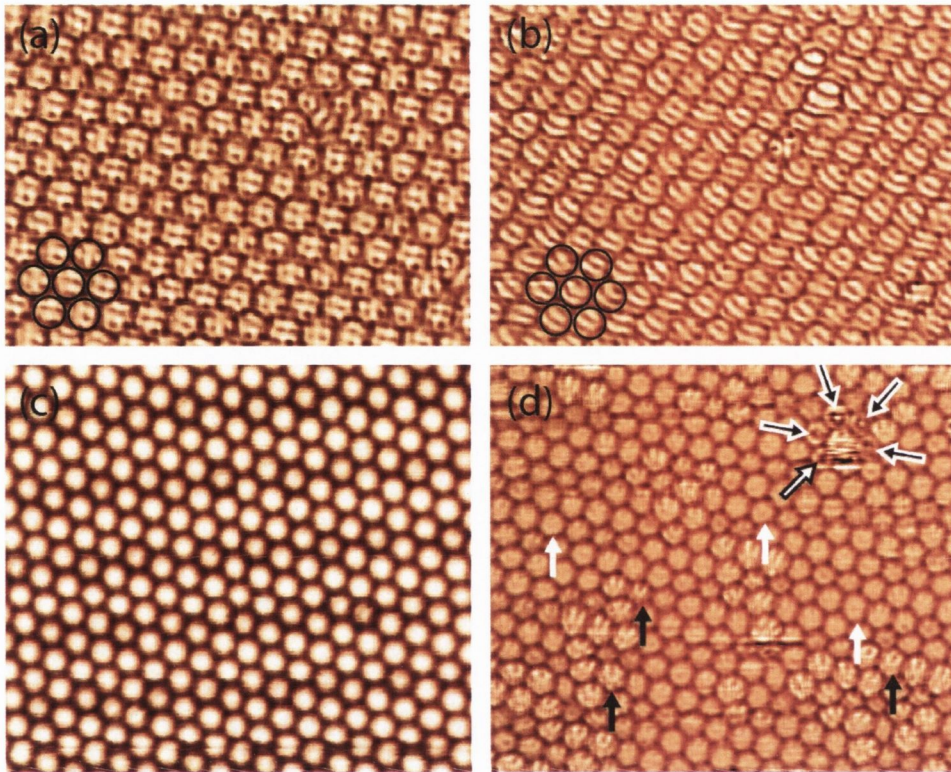
Figure 3.12:   STM images of the C$_{60}$ monolayer at different temperatures.
(a) and (b) 12 nm × 14 nm STM images acquired at 78 K. (a) image of
quenched C$_{60}$ film; (b) image of the C$_{60}$ film obtained by slow cooling at
a rate of 100 K/day. Highlighted in black in panels (a) and (b) are the
outlines of individual molecules. (c) and (d) 19 nm × 16 nm STM images
of the same C$_{60}$ film acquired at 315 K and 256 K respectively. All molecules
in (c) appear as perfect spheres due their fast rotation. Solid black arrows
in panel (d) indicate examples of static C$_{60}$ molecules, solid white arrows
show molecules with unresolved orbital structure, black-outlined and white-
outlined arrows point to spinning molecules with a dip or a protrusion at
the centre, respectively (see text). (a) and (b) have had some high-frequency
mechanical noise removed by FFT filter.

ure 3.12b). Almost all C$_{60}$ molecules in Figure 3.12b exhibit this striped

structure, which indicates that these molecules face the substrate with an

h–h bond [46]. Such an approximate orbital alignment has been observed

both along and perpendicular to a close-packed direction of the molecular

layer. As the state shown in Figure 3.12b results from slow cooling, it would suggest that the alignment with the h–h bonds facing the substrate has lower energy than the glassy, metastable state obtained by quenching the sample. In this chapter, common notations for states characterized by different bonds between C_{60} and the surface are used: h, h–h, p, h–p, and s.

At a temperature of 78 K, the majority of the molecules retained their orbital structure and they were static for the duration of the experiment (up to several days), regardless of whether they were in the h–h or h–p state. In contrast, at high temperatures ($T > 259$ K), the orbital structure of individual C_{60} molecules is no longer visible in STM images (Figure 3.12c) due to the molecules' rotation, which is faster than the time resolution of the STM. All C_{60} molecules appear in these STM images as perfect spheres.

At intermediate temperatures (220–259 K), both static and rotating molecules appear in the STM images (Figure 3.12d). In the temperature range 220–259 K the fraction of static molecules rapidly decreases with increasing temperature.

At $T < 220$ K, almost all molecules exhibit the orbital structure. The few anomalies are likely caused by defects on the surface. Figure 3.13 shows the temperature dependence of the square of the probability of finding a static C_{60} molecule, p^2, to demonstrate the observed transitions and reveal the order parameter η. Each point in Figure 3.13 corresponds to several large-scale STM images of the C_{60} film at that temperature (of similar size to Figure 3.12d), and p is calculated by counting the number of static molecules in an image and dividing by the total number of visible molecules.

According to Landau's theory of phase transitions, the order parameter η is proportional to $(T_C - T)^{1/2}$. At low temperatures $(T < 220\,\text{K})$, p^2 is constant with respect to temperature, but does not quite reach unity, since the few molecules close to the defects appearing in the STM images were not included in the number of static molecules. The horizontal blue trend line shown is a fit to the data, with its slope set to 0.
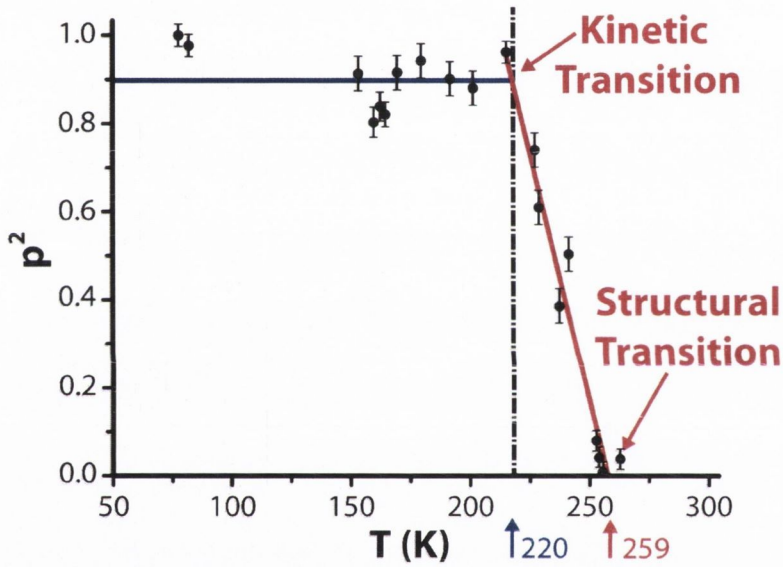
Figure 3.13: Squared probability of finding a static C$_{60}$ molecule, p^2, versus temperature, T. Blue (220 K) and red (259 K) arrows indicate the temperatures of the kinetic and structural rotational transitions respectively. In the temperature range from 220 K to 259 K, p^2 is fitted by a linear function $p^2 = \alpha(T_C - T)$, where $\alpha = 0.022 \pm 0.002\,\text{K}^{-1}$ and $T_C = 259\,\text{K}$.

In the temperature range from 220–259 K, p^2 is fitted by a linear function $p^2 = \alpha(T_C - T)$, where $\alpha = 0.022 \pm 0.002\,\text{K}^{-1}$ and $T_C = 259\,\text{K}$. T_C indicates the temperature of the rotational phase transition. The glassy transition at $T_g = 220\,\text{K}$ is a kinetic transition, at which the molecular switching rate between different states becomes slower than the time scale of the experi-

ment. Below T_g, the C_{60} molecules' nanomotion becomes virtually frozen and orbital-resolved STM images of individual molecules do not change.

3.5.2   Molecular transitions between different states

Orbital-resolved STM images of C_{60} present a unique opportunity to study the rotational transition mechanism on a molecular scale. Figure 3.14 shows a consecutive set of STM images of the C_{60} monolayer measured at $T = 256\,K$, in the vicinity of the rotational phase transition, $(T_C - T)/T_C = 0.012$.
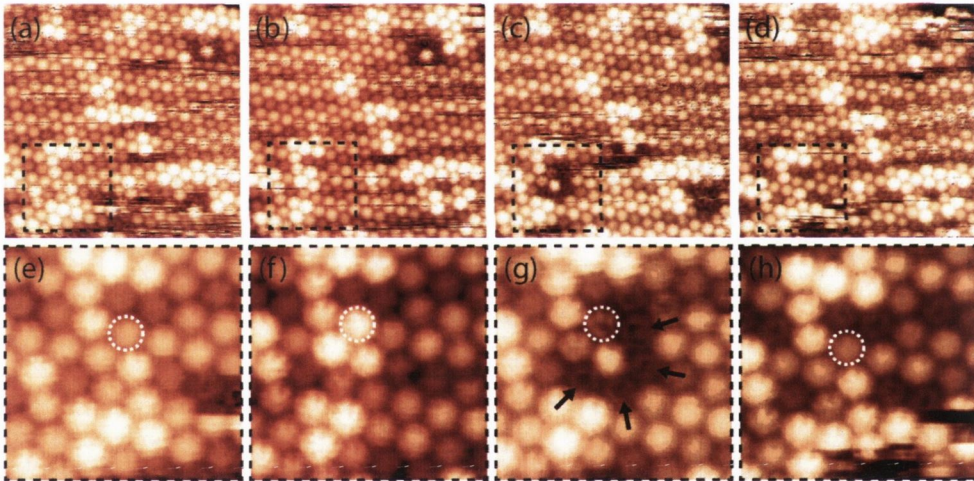
Figure 3.14: Dynamics of the transitions between different molecular states of a C_{60} monolayer at $T = 256\,K$. **(a)–(d)** 19 nm $\times$ 19 nm STM images of the C_{60} film acquired at $V_{sample} = 1.0\,V$ and $I_t = 0.07\,nA$, over a sampling time of 480 sec. Panels **(e)–(h)** present a zoom of the area marked by the dashed box in panels (a)–(d). The same molecule is indicated by a white circle in (e)–(h) and it can be seen to switch from the medium-conductance state (e) to the high-conductance state (f) and to go from spinning (g) to non-spinning (h). Arrows in panel (g) highlight several molecules that engage in spinning motion, resulting in their ring-shaped appearance. These molecules do not spin in (e) and (f). (a)–(d) are unfiltered, however the zooms have had some horizontal scarring corrected to enhance presentation.

The STM images presented in Figure 3.14a–h indicate how C_{60} molecules can switch between several different states, leading to changes in their appearance. Some molecules switch between a high- and a low-conductance state, observed in STM images as a repetitive switching between a bright and dark appearance. This will be explored in detail in Section 3.6. Furthermore, static molecules exhibit an orbital structure [46], while those with high-magnitude oscillations and molecular rotation appear blurry in STM images.

Panels e–h show a zoom of the area marked by a dashed box in panels a–d. A single molecule which switches between states in subsequent scans is shown by a dashed circle. The mechanism of a molecule's switching is connected to its rotation, accompanied by charge transfer to or from the molecule, leading to it becoming polarized [144, 145]. The molecules can also switch between static (orbitals resolved) and dynamic (orbitals blurred) states.

We also observe molecules that appear in the STM images as a ring shape, or a ring with a protrusion at the centre (Figure 3.12c, Figure 3.14e, f, h). Such shapes can be explained by the molecules spinning around their axis perpendicular to the surface. This is shown in detail in Figure 3.17. Arrows in Figure 3.14g indicate several such spinning molecules exhibiting the ring shape appearance. These molecules do not spin in Figure 3.14e or Figure 3.14f.

From the analysis of an extensive number of STM images it was found that, in many cases, the switching of one molecule into a bright state can trigger the spinning of its nearest neighbors. It was also observed that spinning

molecules tend to occupy positions along the grooves of the WO$_2$/W(110) substrate, as shown in Fig. 3.15. This suggests that the energy levels of the C$_{60}$ molecules are affected by the substrate and also that the molecular states can be made more stable or less stable depending on the position of the molecule within the unit cell of the WO$_2$/W(110) structure.
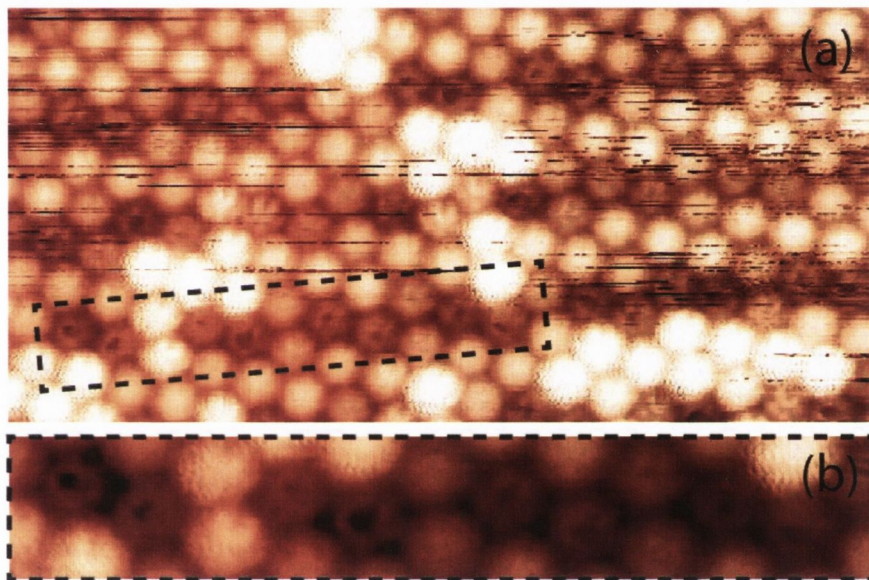
Figure 3.15: **(a)** 19 nm × 9 nm STM image of the C$_{60}$ film acquired at $V_{sample} = 1.0$ V and $I_t = 0.07$ nA, demonstrating the decoration of the WO$_2$ rows of the underlying substrate surface by dim C$_{60}$ molecules, $T = 256$ K. **(b)** Zoom of the area indicated by the dashed box showing a row of spinning molecules.

Therefore, in addition to the transition between different orbital states, there are transitions between the static state of the molecule and spinning state (in-plane rotation). Such phenomena are only observed for isolated molecules and molecular clusters in the monolayer, and so are not caused by molecular transfer to the tip or other tip effects, because if that were the case, the tip would affect all molecules being imaged.

3.5.3   DFT calculations of C_{60} orientation & spinning molecules

DFT was performed using the VASP code and LDA pseudopotentials. The choice of LDA is justified, as it has been shown that DFT-LDA has given excellent results for the total energies and band structures of fullerites and other carbon-based structures (graphite, nanotubes) [146–151].

Girifalco and Hodak state that first-principles calculations for graphitic structures can be carried out quite successfully, but they are sensitive to the details of the calculation, and long-range dispersion interactions, such as van der Waals forces, should be included for separation distances greater than 1.15 of the equilibrium separation [152]. However, the separation distance of C_{60}–C_{60} on the $WO_2/W(110)$ surface is 9.5 ± 0.5 Å, which is less than the intermolecular distance of 10 Å in the bulk C_{60} crystal. This strongly suggests that van der Waals interactions can be neglected for the system under investigation in this thesis, and that DFT-LDA calculations are sufficient.

To find the optimum surface site of a single C_{60} molecule on one layer of WO_2, several different surface sites (labelled A, B, C, D and E in Figure 3.16) were sampled and the total energy of those systems was calculated. The system was found to have the lowest ground state energy when the C_{60}'s surface-facing C–C bond bridged two surface oxygen atoms, each of which was bonded to a different tungsten atom (site A). This site was chosen for all further calculations, and in order to further minimize the energy of the system, different orientations of C_{60} on this site were simulated. For all
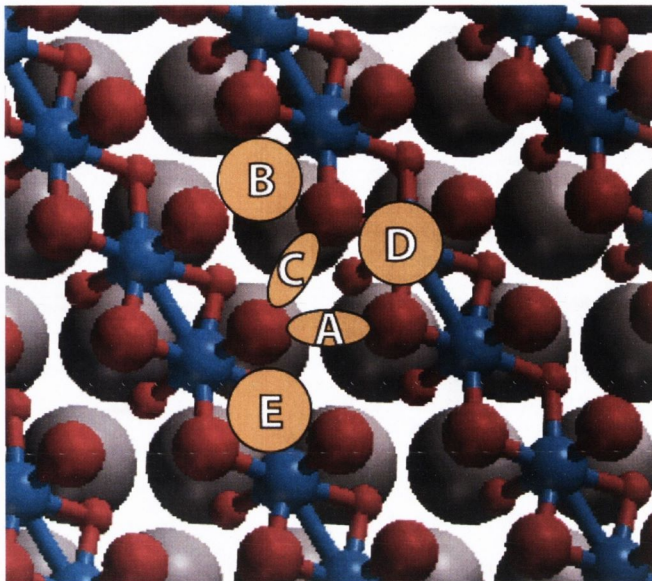
Figure 3.16: Model showing the absorption sites on WO$_2$/W(110) tested during optimisation. Each ellipse shows the position of the surface-facing C–C bond of the C$_{60}$. Site A was exhibited the lowest energy and so was chosen for all subsequent calculations.

orientations, the C$_{60}$ molecule was allowed to relax on a constrained layer of WO$_2$.

DFT calculations of the total free energy reveal that the h–h configuration corresponds to the lowest energy state. The h–p configuration is separated from the lowest energy state by 17 meV, which is comparable to $k_B T$ in our STM experiments. The energy gap between the p and the h–h configurations is about 90 meV. The h and s configurations are the least favorable, being separated in energy from the h–h configuration by 360 meV and 420 meV respectively. The partial charge density of each of these systems was calculated in the range from E_F to 1 eV, where E_F is the Fermi energy.

The obtained charge distribution images (Figure 3.17, first row) were then processed by rotating them in increments of 5 degrees. The resulting rotated
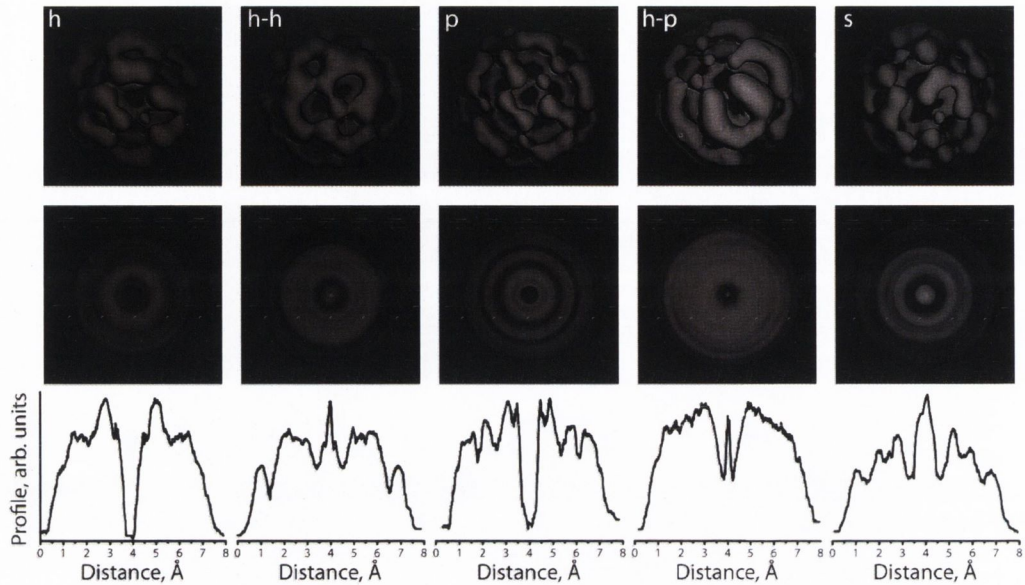
Figure 3.17: First row: DFT simulations of the partial charge density distribution of electron states of static C_{60} molecules facing the substrate by different parts of the molecule. h and p configurations correspond to the molecule facing the substrate by a hexagon or a pentagon, respectively. In h–h and h–p configurations, C_{60} faces the surface by the C–C bond shared between two hexagons or a hexagon and a pentagon, respectively; and in the s configuration, C_{60} faces the surface by a single atom. Second row: Images obtained by rotating the charge distributions in the top panel in increments of 5 degrees. These represent the weighted electron density of a molecule in a particular configuration with the additional degree of rotation around the axis perpendicular to the substrate. Third row: Cross-sections through the rotated charge distribution shown in the second row.

images (Figure 3.17, second row) were combined to form a single composite weighted image for each orientation. This represents a molecule spinning too fast for the STM probe to resolve. The charge distribution images for h and p orientations reveal a dip at the center of the molecular image while for h–h, h–p and s orientations, the ring shape of the molecule is accompanied by a protrusion at the center. Cross-section profiles of these simulated spinning molecules are shown in Figure 3.17 for comparison with experiment. STM

images of individual spinning molecules were found to have either a ring shape with a dip/dent (Figure 3.18a) or a protrusion in the centre (see molecules indicated by black arrows in Figure 3.12c and Figure 3.18c).
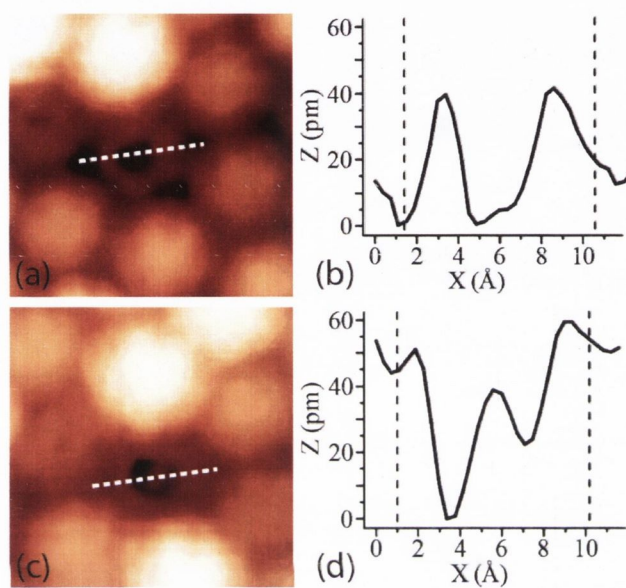
Figure 3.18: STM images of individual spinning molecules with a dip **(a)** or a protrusion **(c)** at the centre. Panels **(b)** and **(d)** correspond to cross-sections along the indicated lines in the STM images of the spinning molecules presented in panels (a) and (c). Dashed lines indicate the boundaries of an individual molecule's cross-section. (a) and (b) have had some horizontal lines on the 'bright' molecules corrected for clarity.

Cross-sections of typical STM images of the spinning C_{60} molecules are presented in Figure 3.18. Panel (b) corresponds to the dip at the centre while (d) corresponds to the protrusion. About 90% of the examined STM images of spinning C_{60} molecules reveal a protrusion at the centre of ring shaped images. According to DFT calculations, h–h and h–p orientations are most favorable in energy. Thus, we conclude that most of spinning molecules face the surface by C–C bonds. The STM image presented in Figure 3.18 with a

dip at the center of the molecule is most likely due to a spinning molecule with a pentagon facing the substrate.

The peak-to-peak diameter of the holes has been observed to vary between approximately 3–6 Å, and the diameters of the experimental cross-sections in Figure 3.18 are approximately a factor of 2 larger than those calculated in Figure 3.17. This difference, and the distribution of diameters, is attributed to molecular movement on the surface, such as the precession of the spinning axis around the surface normal, for which different precession angles will alter the apparent size of the hole by different amounts. The h and s configurations of the molecules are unlikely to be observed to spin under the present experimental conditions because of the large gap in energy from the ground state. Thus the model suggests that a spinning molecule presents a reasonable explanation for the unusual appearance of the C$_{60}$ molecules observed in the temperature range of 220–259 K.

3.5.4   Phase transition

In the three-dimensional C$_{60}$ crystal, two transitions are associated with molecular rotation: a first-order transition that takes place at 259 K and a kinetic glassy transition at 90 K [130–136]. Above 259 K, the molecules freely rotate. At lower temperatures, the molecules hop between two orientations separated in energy by about 11 meV. At 90 K, the C$_{60}$ crystal undergoes a glassy transition when the equilibrium relaxation time τ exceeds the laboratory experiment time. τ was estimated to change from 1 second to 1 day

between $130\,\mathrm{K}$ and $90\,\mathrm{K}$, with a relaxation activation energy, W_τ of about $290\,\mathrm{meV}$ [138].

We found that at $T > 259\,\mathrm{K}$, the C$_{60}$ molecules in the monolayer deposited on the WO$_2$/W(110) surface freely rotate (Figure 3.12d), similar to behaviour observed in solid C$_{60}$. In contrast, at lower temperatures ($T < 259\,\mathrm{K}$) we found significant differences between the monolayer and bulk C$_{60}$. However, it is surprising that the temperature of the rotational phase transition in the C$_{60}$ monolayer on the WO$_2$/W(110) surface coincides with that of solid C$_{60}$.

When very close to the phase transition temperature, fluctuations appear in the form of blinking or spinning molecules. Hence, close to T_C there will be inhomogeneity introduced by these fluctuations but not necessarily large regions of instability, similar to how orientational melting begins at the surface of bulk C$_{60}$ [143]. The amount of these fluctuations decays exponentially away from T_C, and at low temperatures the film looks homogeneous (Figure 3.12b).

According to mean field theory [153], the temperature of a phase transition, $T_C = E/2k_B$, is determined by the total energy of interaction between the molecule and its neighbors. In a C$_{60}$ monolayer, this is determined by the C$_{60}$'s interaction with its neighboring molecules, the C$_{60}$–substrate interaction and the crystal field. The interaction between C$_{60}$ molecules has been studied using several models. Calculations [154, 155] reveal that, in the case of C$_{60}$ molecules separated by $1\,\mathrm{nm}$, a distance comparable to the separation between molecules' centres in a monolayer, the dominant contribution is due to the Coulomb interaction between the molecules' respective

charge densities. These calculations show that several combinations of orbital configurations of two adjacent C_{60} molecules are close in energy.

The coordination number of a C_{60} molecule in a monolayer is halved to 6, compared to the 12-fold coordinated FCC bulk lattice. Therefore one could simplistically expect a T_C reduced roughly by a factor of two compared to that of the bulk, if the interaction with the substrate was neglected. Such a reduction is indeed observed at the (111) surface of a C_{60} crystal [143, 156]. In contrast, our experiment shows the same value of $T_C = 259$ K for the C_{60} monolayer as that of the bulk, suggesting that an energy contribution on the order of $k_B T_C = 24$ meV originates from interactions with the substrate.

There are two possible mechanisms for such an interaction: via the crystal field, which has a strong component perpendicular to the substrate due to the breaking of z-translational invariance [157]; or due to the effect of the overlap of the orbitals of the C_{60} molecules and the substrate.

The wave function of the HOMO of a single C_{60} decays out of the molecule over the length scale of a covalent bond (1.4 Å). This is comparable to the distance between the C atoms of an individual C_{60} molecule and the substrate surface atoms, as determined experimentally (approximately 1.5 Å). The importance of the interaction of C_{60} with the substrate is confirmed by the decoration of $WO_2/W(110)$ grooves by spinning molecules (Figure 3.15d). This suggests that the energy of the C_{60} is sensitive even to relatively small changes in the environment, such as being brought into closer contact with the substrate due to the $WO_2/W(110)$ coincidence structure.

In the mean field theory approximation, the order parameter's dependence on the temperature is specified as $p^2 \approx \frac{3(T_C-T)}{T_C} = \alpha(T_C - T)$, where

$\alpha = 0.012\,\mathrm{K}^{-1}$. The experimentally-measured value of $\alpha = 0.022 \pm 0.002\,\mathrm{K}^{-1}$ is approximately a factor of two greater than that predicted by theory. One reason for this discrepancy is that correlation effects are ignored by mean field theory. Examples of such correlation effects that have been observed are presented in Figure 3.12d, where it is shown that static molecules form clusters, and their orientations within the clusters are correlated. This implies that the total energy of a molecule's interaction with its neighbours is also affected by its configuration on the substrate.

3.5.5   Kinetic transition

The glassy transition and non-exponential relaxation in solid C$_{60}$ are due to the freezing of weakly-correlated orientations of nearest-neighbor molecules [137]. In bulk C$_{60}$, the molecules can occupy two rotational orientations which are almost equivalent in energy but are separated by a potential barrier, and these orientations are distributed in a random fashion over the sites of an FCC lattice. The relaxation of solid C$_{60}$ is determined by the potential barrier between these two states. All individual molecules in solid C$_{60}$ occupy equivalent positions in the FCC lattice; each molecule relaxes nearly identically in an intrinsically non-exponential manner according to a homogeneous scenario [158].

This relaxation is characterized by the Kohlrausch-Williams-Watts or stretched exponential function, $q(t) = q_0 \, \exp[-(t/\tau)^\beta]$, where τ is the relaxation time, and β is called the non-exponential factor or "stretching exponent". $\beta = 1$ corresponds to an exponential, Arrhenius-like relax-

ation [137]. The temperature dependence of τ can be fitted by the Vogel-Fulcher-Tammann (VFT) function, $\tau(T) = \frac{1}{f_l} \exp[\frac{W}{k_B(T_0-T)}]$, where f_l is the libron frequency [158, 159]. When $T_0 = 0\,\mathrm{K}$, the Arrhenius equation is realized and W corresponds to the activation energy. According to empirical observations, T_0 corresponds to the temperature of an ideal glass state ("Kauzmann temperature"), at which the crystal and the extrapolated glass state attain equal entropies [159] and the relaxation time becomes infinite.

Both β and $\frac{T_0}{T_g}$ are a measure of the deviation from Arrhenius relaxation. The relaxation in solid C_{60} was found to differ slightly from a purely exponential decay ($\beta = 0.94$) [137]. The kinetic behavior of the C_{60} monolayer grown on the $WO_2/W(110)$ surface is influenced by several factors. The low-temperature glassy state of the C_{60} film is characterized by a random orientation of the molecules (Figure 3.12a). In contrast, the glassy state in solid C_{60} is characterized by the random freezing of molecules among just two states. The large number of different molecular orientations observed in the film results in an averaging-out of the interaction potentials and should cause Arrhenius-like relaxation processes. However, STM experiments reveal correlations in the nanomotion of the C_{60} molecules that suggest arguments in favour of a constrain-dynamic scenario [160]. It is proposed that the mechanism for the molecule–molecule interaction required for such a constrain-dynamic scenario can be based on some molecules acquiring charge. Indeed, the time-resolved STM experiments presented herein demonstrate that the rotational transition of an individual C_{60} molecule between states is accompanied by charge transfer to the molecule, and subsequently, charge carried

by a molecule affects the energy levels and barrier heights of its neighboring molecules via the Coulomb interaction.

From the lifetime of a molecule in a single state, the potential barrier height separating the states has been calculated to be 617 meV. If one assumes that the bulk libron frequency of $f_l = 1 \times 10^{12}$ Hz and the relaxation time at the temperature of glassy transition for solid C_{60}, $\tau_S(90\,K) = 1$ day can be applied to the film, then the VFT law can be used to estimate the Kauzmann temperature T_0. The obtained value $T_0 = 45$ K indicates that the relaxation process in the C_{60} monolayer film is close to the Arrhenius scenario of $\frac{T_0}{T_g} = 0.2$.

3.6 Charge transfer and rotation

As has been touched upon in previous sections, some molecules appear to switch between "dim" and "bright" states [25, 35]. This phenomenon has previously been attributed to C_{60}-induced substrate reconstructions [25, 30–36]. Such surface reconstructions lead to two topographically-different C_{60} adsorption sites, where dim C_{60} molecules are sunk into nanopits on the reconstructed substrate, and are lower in height than the bright ones [25, 30–36, 46]. The switching between dim and bright C_{60} states was attributed to changes in the substrate underneath the molecular layer due to the diffusion of substrate atoms [25, 35]. Other explanations suggest that this apparent height difference is due to electronic and molecular orientation effects [106, 107, 118]. Better understanding of the switching of C_{60} between different

charge states is central to further progress in electronic devices utilizing these molecules.

This section describes the charge-transfer induced switching of some isolated C_{60} molecules within the monolayer grown on the $WO_2/W(110)$ surface. Such switching of individual C_{60} between different charge states represents a phenomenon that is different from the "bright" and "dim" contrast shown in Figure 3.10a, which was due to the "dim" molecules lying in the grooves between the nanorows. Furthermore, these two phenomena coexist on the $WO_2/W(110)$ surface. Our results indicate that C_{60} switching between charge states correlates with the molecule's rotation, i.e. some orientations of the molecule favour its charge neutral state and others favour the negatively charged state.

Figures 3.19a–c show a sequence of constant-current STM images of the same area of the C_{60} monolayer self-assembled on the $WO_2/W(110)$ surface, acquired at a sample bias of 1.0 V. These images, taken at 255 K, exhibit an internal structure corresponding to molecular orbitals for most of the C_{60} molecules. Comparing their appearance with the partial charge density calculated by DFT [46, 47] (Section 3.5.3), it is noted that the majority of the molecules face the substrate with an h–h bond (indicated by a black circle in Figure 3.19b), exhibiting three distinct "stripes" [25, 31, 32, 46, 47, 161]. Most of the other molecules face the substrate with an h–p bond (white circle). This is in agreement with DFT calculations described in Section 3.5.3 which show that the h–h orientation has the lowest total energy, while the h–p orientation differs from the lowest energy state by 17 meV [47], which is comparable to $k_B T$ in our STM experiments.
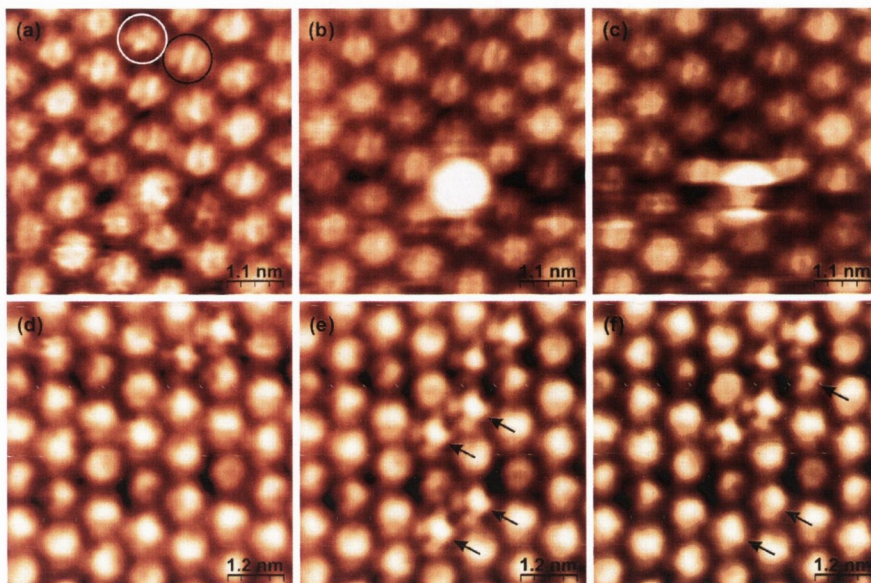
Figure 3.19: **(a)**–**(c)** Constant-current STM images (5.5 nm × 5.5 nm) of the same area of the C_{60} monolayer on the WO_2/W(110) surface acquired at 255 K, $V_{sample} = 1.0$ V, $I_t = 0.1$ nA. The majority of C_{60} molecules face the substrate with an h–h bond (indicated by a black circle), while others face the surface with an h–p bond (white circle). The molecule at the centre of images (a)-(c) switches between different states, changing its appearance. (c) demonstrates the case when switching occurs fast enough to be seen on a single image. **(d)**-**(f)** Constant-current STM images (6 nm × 6 nm) of another area of the monolayer acquired at 255 K, $V_{sample} = -1.9$ V, $I_t = 0.1$ nA. Arrows indicate the C_{60} that have switched between frames. The molecules exhibiting internal structure in (d)-(f) are in the negatively charged state. (a)–(c) have had some high-frequency noise removed by FFT filter, and (d)–(e) have been smoothed using a 3 × 3 matrix to remove mechanical noise.

Although individual C_{60} molecules do not appear identical to one another due to their different orientations on the surface [25, 30–36], the orbital structure of each molecule remains unchanged from one image to the next, indicating that these molecules are not rotating. However, some individual molecules, such as the one at the centre of the image, switch between different states. In the temperature range between the phase transitions (220–260 K) such molecules change their appearance continuously in a random fashion

for the entire duration of the experiment. Figure 3.19c demonstrates the case when switching occurs fast enough to be seen on a single image. This phenomenon is observed at both positive and negative biases, with the best apparent contrast achieved at a positive sample bias of 0.8 V.

Figures 3.19d–f show a sequence of constant-current STM images of another area of the monolayer, acquired at a sample bias of -1.9 V. Several molecules are observed to switch between scan frames (indicated by arrows). The apparent height difference between the molecules in the two different states is much smaller at this bias. The orientation of most of the molecules cannot be resolved at a negative bias. However, the orbital structure of the molecules in the state which has a lower apparent height is more pronounced and they are observed to be in the h–p orientation on the surface. It is noted that imaging the surface with a sample bias in the range of -0.5 V to 0.6 V, was unsuccessful, resulting in noisy images. This was most likely due to the band gap of C_{60}. At lower temperatures the molecular switching between the different states ceases and at high temperatures the molecules rotate continuously so fast that no switching is observed and all molecules appear as perfect spheres [47].

Figure 3.20a shows a constant-current STM image of the C_{60} monolayer, acquired at 257 K. The image emphasizes the difference between the previously described phenomenon of the "bright" and "dim" C_{60} contrast [25, 30–36] and the C_{60} switching between charge states. Three types of molecules are clearly visible in Figure 3.20a: "dim", "normal" and "very bright". They are different in apparent height, which can be seen from the line profile taken along the dashed line in Figure 3.20a and shown in Figure 3.20b. The first

two types represent "dim" and "bright" contrast due to the substrate topography, with "dim" C_{60} molecules arranged in dark chain-like structures on the surface (marked by the arrows in Figure 3.20). Such a contrast is also observed at temperatures below 220 K as well as at both bias polarities [46].
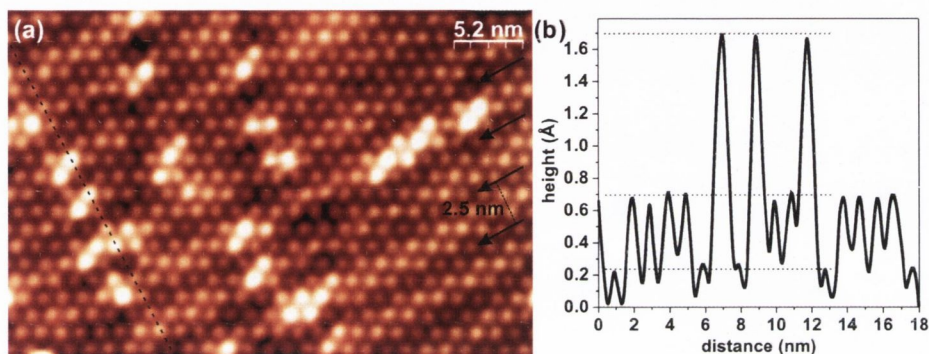
Figure 3.20: **(a)** Constant-current STM image (26 nm × 18 nm) of the C_{60} monolayer on the WO_2/W(110) surface acquired at 257 K, $V_{sample} = 1.0$ V, $I_t = 0.1$ nA. The majority of very bright molecules are predominantly located along the top of the oxide nanorows. **(b)** A line profile (along the dashed line in (a)) indicating the height difference between the "dim", "normal" and very bright C_{60}.

The distance between these chains is 2.5 nm, which is equal to the width of oxide nanorows forming the substrate [46]. These "dim" C_{60} molecules follow the oxide nanorows along the $[\bar{3}37]$ direction of the substrate, occupy the grooves between them, and, as a result, are situated slightly lower (by approximately 0.5 Å, see Figure 3.20b) than the "normal" C_{60}. There are, however, very bright molecules in Figures 3.19 and 3.20, with a much greater height difference of about 1 Å (Figure 3.20b) between them and the "normal" C_{60}. These very bright molecules are predominantly located along the top of the oxide nanorows, with very few of them found lying in the grooves between the rows, as can be seen in Figure 3.20a.
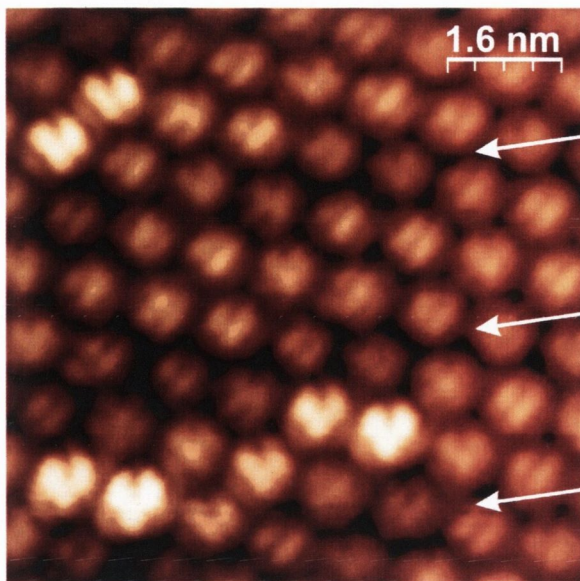
Figure 3.21: Constant-current STM image (8 nm × 8 nm) of C_{60} on the $WO_2/W(110)$ surface, showing that the very bright C_{60} molecules have the h–p orientation: $V_{sample} = 0.95\,\text{V}$, $I_t = 0.1\,\text{nA}$. Arrows indicate chains of the "dim" molecules, which occupy the grooves between the oxide nanorows of the $WO_2/W(110)$ surface.

A majority of very bright molecules face the substrate surface with an h–p bond, as can be seen in Figure 3.21. Furthermore, such C_{60} molecules change their appearance in time, switching randomly between two different states. The rate of switching between the states depends on temperature. In the temperature range of 220–260 K, where switching is observed, the total number of switching molecules rapidly decreases with decreasing temperature.

3.6.1   Switching time-evolution

The time-evolution of the tip-surface distance measured at two different sample biases (1.0 V and −1.9 V) is presented in Figure 3.22, when the STM tip

is placed above an individual switching C_{60}. In both cases the STM tip shifts between two different height levels (indicated by dashed lines), corresponding to two different states of the molecule. The tip-surface distance changes by approximately 1 Å during the switching of the molecule when a bias of 1.0 V is applied (Figure 3.22, top spectrum). This cannot be explained in terms of different geometrical orientations of the C_{60} on the surface or by C_{60}-induced substrate reconstructions [25, 30–36].
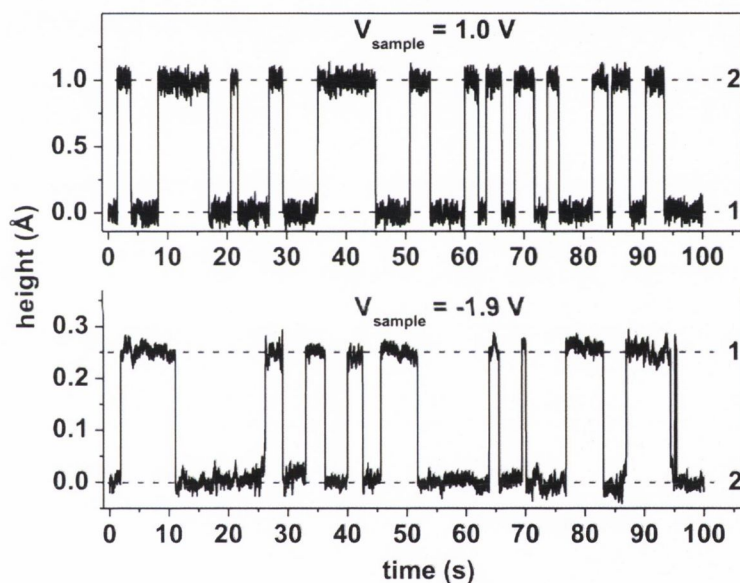
Figure 3.22: The time-evolution of the STM tip-surface distance for the switching C_{60} molecule measured at a sample bias of 1.0 V (top) and −1.9 V (bottom). The acquisition time was 10 ms per point. Two different states are present (indicated by dashed lines): state 1 corresponds to the charge-neutral C_{60} and state 2 to the negatively charged C_{60}.

If, for example the C_{60} molecules were inducing the substrate to reconstruct, the number of bright molecules would be conserved over time, as described by Gardener and co-workers [25]. However in the present case, molecules are observed to switch at random. The quality of the oxide sub-

strate was confirmed by STM prior to C_{60} deposition, and the film was found to have a very low concentration of defects. Since C_{60} switching was observed over the entire sample and was not limited to one particular area, it can be concluded that the effect is not caused by the presence of defects.

It is suggested that this C_{60} state arises due to charging of the molecule, which causes changes in the local density of electron states and consequently a variation in tunneling current. Using density functional theory calculations, it was found that the two different states of the C_{60} on the $WO_2/W(110)$ surface can be related to: (1) the charge-neutral C_{60} (normal appearance, Figure 3.19a) and (2) the negatively charged C_{60}, which has accepted an electron (C_{60}^-, very bright appearance, Figure 3.19b). It is noted that, in most cases, switching between the charge-neutral C_{60} in the h–h orientation and the C_{60}^- in the h–p orientation has been observed (see Figures 3.19d–f).

However, in rare events, more than two states were distinguished during the switching of some molecules, indicating that this phenomenon can be quite complex. It is proposed that the negatively charged C_{60} state results from the acceptance of a tunneling electron from the STM tip or the substrate depending on the bias applied. This is based on the fact that the switching of the molecule into the charged state is triggered continuously when the STM tip is static above an individual C_{60} with a bias applied (as in Figure 3.22). Molecular movement accompanies the molecule's switching back to the charge neutral state, i.e., as the molecule rotates, it loses charge to the substrate or neighbouring molecules.

A similar charging process was observed by Repp et al., for the system of gold atoms adsorbed on bi- and trilayers of NaCl grown on the Cu(111) and

Cu(100) surfaces [162]. By positioning the STM tip above an Au adatom and applying a voltage pulse, the adatom can be reversibly switched between its neutral and negatively-charged state. Both states have been found to be stable due to the greatly suppressed mobility of Au adatoms at the temperature of the experiment (5–60 K) as well as the reduced coupling of the electronic states of the adatom with the metal substrate due to the insulating NaCl film [162]. Recently, it has been shown that the charge state of molecules can be manipulated in a similar manner [163].

STM experiments performed at temperatures below 10 K have revealed that individual Cu phthalocyanine molecules deposited on the NaCl/Cu(111) surface can be negatively charged by applying low voltage pulses [163]. In our experiment, the ultrathin WO_2 layer reduces the coupling of the electronic states of the C_{60} with the W(110) substrate, which allows the molecule to hold charge for some time. However, each C_{60} molecule that undergoes switching is surrounded by six neighbours in the monolayer, resulting in van der Waals interactions between the molecules. This interaction may influence molecular movement and stability on the surface and hence affect the switching.

3.6.2   Density of states of C_{60}

Figure 3.23 shows the density of states (DOS) calculated for two different molecules, the charge-neutral C_{60} and the C_{60}^- with the h–h and h–p orientations, respectively. The C_{60} orientation on the surface in each case has been chosen on the basis of experimental observation that most of the "normal" molecules face the substrate with an h–h bond, while the majority of very

bright C_{60} face the substrate with an h–p bond. The addition of an electron
to the C_{60} molecule changes its electron density of states. This results in
the old lowest unoccupied molecular orbital (MO) being half-occupied and
becoming the new highest occupied MO, which in turn causes the valence
band structure to shift relative to the Fermi energy.
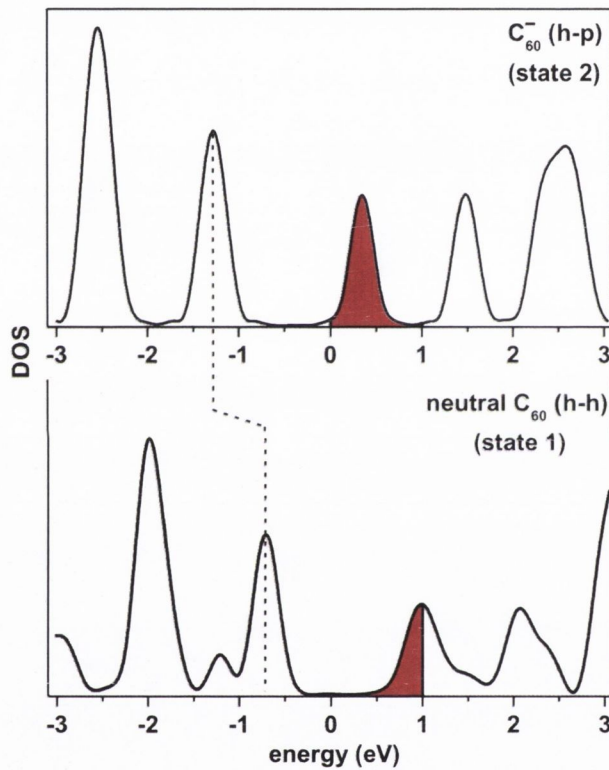
Figure 3.23:   The calculated density of states (DOS) for C_{60} on the
$WO_2/W(110)$ surface in two different states: negatively charged (C_{60}^-, h–p
orientation, very bright appearance at 1.0 V bias) and charge-neutral (C_{60}, h–
h orientation, normal appearance at 1.0 V bias). The highlighted area shows
the molecular states involved in tunneling, when a sample bias of 1.0 V is
applied. The dashed line indicates the shift of the DOS relative to the Fermi
energy ($E = 0\,\text{eV}$) when an extra electron is added to C_{60}.

The highlighted area in Figure 3.23 shows the molecular states involved

in tunneling, when a 1.0 V sample bias is applied. This bias leads to the

apparent height contrast of 1.0 Å between different molecular states in STM images (see Figures 3.19 and 3.20) and corresponding changes in the STM tip-surface distance (Figure 3.22, top curve). Note that there is a significant increase in the molecular states available for tunneling (in the energy range from 0–1.0 eV) in going from the charge-neutral C_{60} molecule (state 1) to the C_{60}^- (state 2), which is reflected in the very bright appearance of the latter at the 1.0 V sample bias.

A difference in DOS for the C_{60}^- and C_{60} molecules (Figure 3.23) suggests that the apparent height difference ΔZ should depend on the applied bias voltage. Indeed, at sample biases higher than 1.5 V (or lower than −1.5 V), the observed apparent contrast between different C_{60} states was significantly smaller because multiple molecular orbitals were involved in tunneling. This minimizes the difference between the DOS for each state of the C_{60} charac-terised by the molecule's charge and orientation on the surface.

From Heisenberg's uncertainty principle, $\Delta E \Delta t > \hbar/2$, the energy res-olution of a state should be inversely proportional to its lifetime [164], i.e. an electron should only exist for a short time in a state whose energy range is broad. This would imply that the broad states calculated in Figure 3.23 should only lead to an observed lifetime on the order of femtoseconds, how-ever one must remember that for the system in question, charge transfer is not the only phenomenon that must be accounted for. In going from the neu-tral C_{60} to charged C_{60}^-, the molecule must rotate from h–h to h–p, which will have its own associated characteristic timescale, and the presence of the STM tip causes charging to be constantly triggered by tunneling electrons. The tip itself may also affect the rotation of the molecule, thus the full complexities

of the switching mechanism are not encompassed by simply calculating the DOS for the two "final" states, however it is illustrative in explaining the apparent contrast between the two observed states. It is unfortunately beyond the scope of this thesis to develop a full theoretical basis for the switching mechanism, however it is an interesting avenue for future work.

The STM tip-surface distance changes by only 0.25 Å during the switching of the molecule with $-1.9\,V$ bias applied (Figure 3.22, bottom curve). This is due to the relatively small difference between the molecular states of C_{60} and C_{60}^- available for tunneling between $-1.9\,eV$ to $0\,eV$. At this bias the C_{60}^- molecule (state 2) has a slightly darker appearance in STM images than the charge neutral C_{60} (Figures 3.19d-f), which is in good agreement with the STM tip-surface distance obtained at $-1.9\,V$ bias (Figure 3.22, bottom curve).

In constant current mode, the apparent height difference ΔZ between the C_{60}^- and the C_{60} molecules can be determined as:

$$\Delta Z = \frac{1}{k} ln \left(\frac{\int_0^{V_b} g_b(\varepsilon) g_t(\varepsilon)\, d\varepsilon}{\int_0^{V_b} g_n(\varepsilon) g_t(\varepsilon)\, d\varepsilon} \right) \tag{3.1}$$

where $g_b(\varepsilon)$ and $g_n(\varepsilon)$ are the DOS of the C_{60}^- and C_{60}, respectively, $g_t(\varepsilon)$ is the DOS of the STM tip and $k = 2\,Å^{-1}$ [165]. The DOS of the monocrystalline W(100) tip, previously calculated in this group [74, 166], exhibits no major features close to the Fermi energy and can be treated as nearly constant in the range considered here. Although it cannot be guaranteed that the tip does not have an attached molecule during the experiments, STM performed before and after $z(t)$ measurements were consistent with the most stably-

observed appearance of the film, and so it is assumed for simplicity that the tip apex consists of only clean tungsten.

Using this formula, the ΔZ between the C_{60}^- (h–p orientation) and the C_{60} (h–h orientation) molecules on the $WO_2/W(110)$ surface has been calculated from the density of states presented in Figure 3.23 under the assumption that $g_t(\varepsilon)$ is nearly constant and is shown in Figure 3.24 as a solid line. This curve is in good agreement with the experimental data for ΔZ obtained from STM images and the time-evolution of the tip-surface distance measured at different sample biases. The data presented in Figure 3.24 indicate that both a large value of ΔZ at certain biases and its overall dependence on bias voltage can only be explained in terms of different charge states of the C_{60} molecules on the surface.
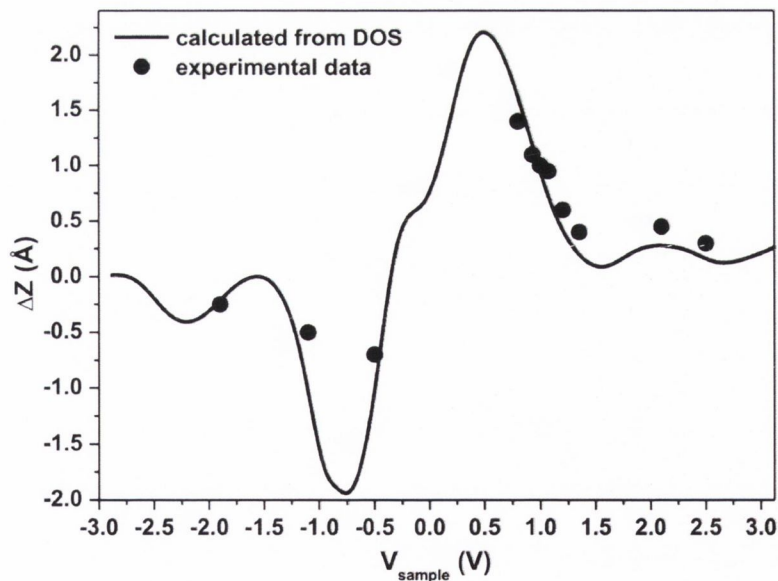
Figure 3.24: The apparent height difference ΔZ between the C_{60}^- (h–p orientation) and the C_{60} (h–h orientation) molecules on the $WO_2/W(110)$ surface calculated (solid line) from the DOS shown in Figure 3.23 compared to the experimentally observed ΔZ (dots) as a function of the sample bias voltage.

These observations are in good agreement with the results of Yamachika et al., obtained during their low-temperature study of controllable C_{60} doping with K atoms on the Ag(001) surface [167]. They have found that approximately 0.6 of an electron is transferred to C_{60} from each K. They have observed only small changes in apparent size between the C_{60} and K_4C_{60} molecules when scanned at 2.0 V sample bias. At this bias the number of orbitals involved in tunneling does not change dramatically when going from C_{60} to K_4C_{60}, as observed by scanning tunneling spectroscopy [167]. However, the $\frac{dI}{dV}$ map measured at 1.25 V and 50 pA was found to be much brighter in the case of the K_4C_{60} molecule, where approximately 2.4 electrons are transferred to the C_{60}, than in the case of undoped C_{60} [167].

3.6.3   The Fukui function of charge states

It has been observed that switching C_{60} molecules change their orientation on the surface. Furthermore, most of the "normal" molecules face the substrate with an h–h bond, while the majority of negatively charged C_{60} face the substrate with an h–p bond. It is reasonable to propose that the process of gaining or losing an electron depends on the C_{60} orientation. Charge transfer efficiency to or from the molecule depends strongly on which part of the molecule is most reactive. The spatially-resolved reactivity of the molecule can be visualized by the Fukui function, $f(r)$, which is considered as a convoluted reactivity indicator [168].

The Fukui function ($f^+(r)$ or $f^-(r)$) is defined as the differential change in the electron density due to an infinitesimal change (increase or decrease) in

the number of electrons. When the molecule accepts electrons, the electrons tend to go to the part of the molecule where the Fukui function $f^+(r)$ is large, because at these locations the molecule is most capable of stabilizing additional electrons [168].

Figure 3.25 shows cross sections of $f^+(r)$ and $f^-(r)$ taken along the h–h and h–p bonds through the centre of the C_{60}, calculated using Dmol3 (Accelrys Materials Studio 4.3). The value of $f^+(r)$ (centre panel) is larger for the h–p bond with respect to the h–h bond, in agreement with previous calculations [168]. This indicates that the addition of electrons to C_{60} is more effective when an h–p bond of the molecule faces the $WO_2/W(110)$ surface and, due to the molecule's symmetry, the STM tip.
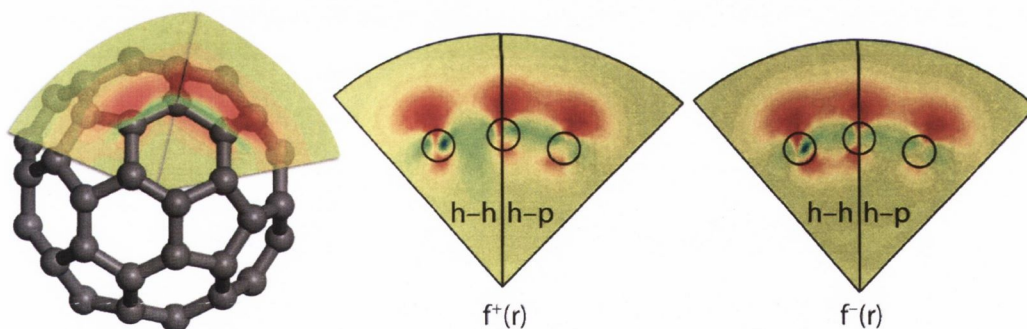
Figure 3.25: Cross sections of the Fukui functions $f^+(r)$ and $f^-(r)$ taken along the h–h and h–p bonds, through the centre of the C_{60}. The centre panel emphasises that $f^+(r)$ has a larger value for the h–p bond than the h–h bond, and the opposite is true for $f^-(r)$, right panel. Circles overlaid on the plots indicate the position of the carbon atoms.

In turn, the analysis of $f^-(r)$ (Figure 3.25) allows one to conclude that the removal of an electron occurs more effectively via h–h bonds. Thus a strong correlation between the charge state of the C_{60} molecule and its orientation on the surface observed in experiments can be explained in terms of charge

transfer efficiency. Electron acceptance by the molecule is facilitated through its rotation to achieve an h–p orientation, which is the most suitable for such charge transfer. In turn, electron loss is accompanied by the molecule's rotation back to an h–h orientation.

Combining all the findings, the following mechanism for the C$_{60}$ switching on the WO$_2$/W(110) surface can be proposed. When the molecule in the neutral state is facing the surface by an h–h bond, there are four h–p bonds in the lower (or upper) part of C$_{60}$ which are located in a symmetric way around this h–h bond. Due to thermal excitation of the molecule, one of these h–p bonds may come closer to the surface (or the STM tip) than the other three and accept an electron. This leaves the negatively charged molecule locked to the surface via this h–p bond. The ultrathin WO$_2$ layer reduces the coupling of the electronic states of the C$_{60}$ to the W(110) substrate, which allows the molecule to hold this charge for some time. However, each C$_{60}$ molecule that undergoes switching is surrounded by six neighbours in the monolayer, resulting in van der Waals interactions between them. This interaction may influence molecular movement and trigger the loss of the electron. This view is simplified to highlight the correlation between the charging of C$_{60}$ and its movement on the WO$_2$/W(110) surface. There can be additional complexities one may need to take into account. For example, our calculation of the Fukui function was done for an isolated C$_{60}$. The proximity of the molecule to the WO$_2$/W(110) surface and to an STM tip will alter the Fukui function.

3.7   Conclusions

In conclusion, time-resolved, variable temperature STM investigations of the C_{60} monolayer deposited on the $WO_2/W(110)$ surface reveal many interesting phenomena. The C_{60} molecules self-assemble into a well-ordered molecular layer in which they form a close-packed hexagonal structure with a unit cell parameter equal to 0.95 ± 0.05 nm. The nucleation of the C_{60} layer starts at the substrate's inner step edges.

By using the $WO_2/W(110)$ surface as a preformed nanostructured template, it was shown that the "dim" C_{60} molecules follow the oxide nanorows of the substrate, occupy the grooves between them, and, as a result, are situated slightly lower than the others ("bright" C_{60}).

At room temperature the molecules rotate faster than the time-resolution of the STM and so appear as featureless spheres, and at 78 K their orbital structure is frozen. Their movement is suppressed, but their orbital ordering depends on the cooling regime. When quickly quenched, the molecules' orbitals are randomly arranged with no correlation between their orientations; however after slow cooling the "stripes" of their orbitals are mostly aligned along or perpendicular to a close-packed direction of the monolayer, due to intermolecular interactions.

Between the two extremes of room temperature fast rotation and low temperature freezing, two separate phase transitions are demonstrated: a rotational phase transition at 259 K and a kinetic glassy transition at 220 K. The temperature of the rotational phase transition is identical to that of 3D

C_{60} crystals (259 K) and the temperature of the kinetic transition is substantially higher (220 K) than the bulk (90 K).

Different mechanisms of molecular nanomotion, such as rotation, spinning and switching between different orientations have been observed. The total energy of the molecular interaction in the film is 48 meV, as estimated from mean field theory. This was found to be approximately a factor of two greater than the energy level separation of an individual C_{60} molecule, as determined from time-resolved STM experiments.

The measurements of the phase transition temperature T_C in the film, combined with the argument of the reduced coordination number suggests a strong contribution from the interaction between the molecules and the substrate. The energy of such interactions was estimated to be 24 meV. The observation of a glassy transition at 220 K reveals a non-exponential relaxation in the C_{60} monolayer. The Kauzmann temperature was estimated to be 45 K.

Individual C_{60} molecules in the monolayer have also been observed to switch between neutral and negatively charged states. The charging of the C_{60} causes changes in the local density of electron states and consequently a variation in tunneling current. The negatively charged C_{60} state results from the acceptance of a tunneling electron from the STM tip or the substrate depending on the bias applied.

It was found that molecular movement accompanies the molecule's switching between these states. The results obtained shed light on the switching of C_{60} between different charge states and provide important information for

the further development of nanoscale molecular devices and molecular switch concepts.

These experiments have demonstrated the effectiveness of STM in the investigation of phase and kinetic transitions in the vicinity of critical temperatures. This is an unexpected result because, in general, the characteristic times of molecular and atomic motion are on the order of picoseconds and the characteristic frequency cut-off of an STM is much slower at 10 kHz ($\sim 100\,\mu s$). However, as the dynamics are highly temperature-dependent, one can find a temperature range where the fluctuations happen on a time scale able to be resolved by STM and thus the temperature of the kinetic transition can be extracted.

Chapter 4

NiDPP on Ag(111) and Ag/Si(111): the Effect of Surface Reactivity

The interplay between the role of intermolecular forces and molecule–surface interactions is a very fine balance. The relative strengths of these two factors determines how molecules self-assemble when placed on the surface.

The effect of the molecular/inorganic interface on possible future device performance cannot be overstated, as this will determine the charge injection and charge flow in such molecular devices [76–78].

In this chapter, using STM and LEED, the effect of the substrate on the self-assembly of a particular porphyrin molecule, (5,15-diphenylporphy-rinato)Ni(II) (NiDPP) is examined by depositing it onto two related – but different – surfaces, Ag(111) and Ag/Si(111)-$\sqrt{3} \times \sqrt{3}$ R30°.

When deposited onto the less-reactive noble Ag(111) surface, NiDPP is able to diffuse across the surface to the step edges and grow into close-packed monolayers. These monolayers are composed of a single domain which covers the entire sample surface.

In contrast, when deposited on the more reactive Ag/Si(111)-$\sqrt{3} \times \sqrt{3}$ R30° surface, the molecules adopt one of three preferential orientations, and bind to the middle of terraces. These initially-bound molecules act as nucleation sites for domains which grow across the terraces. Many domain boundaries are evident on the surface, with all three orientations present on a single terrace.

The results contained herein shed light on the complex interactions between adsorbates and surfaces, and show that the reactivity of the substrate plays a major role in molecular self-assembly.

4.1   Experimental details

The STM experiments were performed at room temperature in an ultra-high-vacuum system consisting of an analysis chamber (with a base pressure of 2×10^{-11} mbar) and a preparation chamber (5×10^{-11} mbar). An electro-chemically etched polycrystalline tungsten tip was used to record STM images in constant current mode. The voltage V_{sample} corresponds to the sample bias with respect to the tip. No drift corrections have been applied to any of the STM images presented herein.

The Si(111) substrate was p-type boron-doped with a resistivity in the range 0.1–1.0 Ω cm. The Si(111)-(7×7) surface was prepared by *in situ* direct

current heating to 1520 K after the sample was first degassed at 870 K for 12 hours. The Ag/Si(111)-$\sqrt{3} \times \sqrt{3}$ R30° surface was prepared by e-beam evaporation of silver (Goodfellow Metals, 5 N) from a molybdenum crucible onto the Si substrate, which was maintained at 770 K during the deposition. The Ag(111) crystal (Surface Preparation Laboratory) was cleaned in situ by repeated cycles of argon ion sputtering ($E_k = 0.8$ keV) and annealing at 820 K. The substrate cleanliness was verified by STM and LEED before deposition of the NiDPP.

NiDPP was synthesized according to a published procedure [169] by Dr Natalia Sergeeva in the School of Chemistry, TCD. The molecules were evaporated in a preparation chamber isolated from the STM chamber at a rate of about 0.2 ML per minute from a tantalum crucible in a homemade deposition cell operated at a temperature of approximately 600 K. The total pressure during porphyrin deposition was in the 10^{-10} mbar range. Before evaporation, the NiDPP powder was degassed for about 10 hours to remove water vapour.

4.2   Porphyrins

Due to their interesting physicochemical properties and conformational flexibility, porphyrins are widely used for the fabrication of complex supramolecular structures, which are utilized in many technological applications including light-harvesting arrays for solar energy generation, sensors, molecular optoelectronic gates, photo-inducible energy or electron transfer systems, nonlinear optics and oxidation catalysts [1, 14, 78, 170–174]. Furthermore, they

are essential to various natural biological processes as the main functional groups of haemoglobin and chlorophyll. To this end, porphyrin derivatives have been used to prepare a rich variety of molecular nanostructures such as clusters, wires and extended networks on different surfaces [1–13].

Such nanostructures offer a number of powerful approaches for the development of molecule-based devices [76–78]. The strength of the porphyrin-surface interaction is a vital parameter for the controlled assembly of these functional molecular species into ordered nanostructures [10, 80]. The nature of the bonding between porphyrins and the surface is reflected in the geometric configuration of molecules at the interface and their molecular charge distribution, and therefore can be probed by STM.

Since the porphyrin family comprises such a rich and diverse group of molecules, many moieties have been studied on many different substrates, from noble metals [8, 10, 11], to semiconductors [175, 176] and oxide surfaces [177, 178]. Several related classes of molecules are also well-studied on surfaces, such as phthalocyanine, porphyrazine, naphthalocyanine and anthrocyanine. Depending on the nature of the substrate and the structure of the porphyrin molecule, the supramolecular ordering can be vastly different, and the appearance of the molecules in STM is determined by the presence or absence of a metal centre.

On noble metal surfaces, such as Ag(111) and Au(111), molecule–molecule attraction tends to dominate over the relatively weak molecule–substrate interaction, and their self-assembly is largely determined by the side-groups present on the molecule.

Krasnikov *et al.* have shown the novel self-assembly of Ni-porphine (NiP) [10] and 5-((10,15,20-triphenylporphyrinato)Ni(II))$_2$ dimer (NiTPP-dimer, structure shown in Figure 4.3a) [11] molecules on the Ag(111) surface.

Despite the fact that the two molecules investigated are both nickel porphyrins, even when deposited on a similar substrate they exhibit different self-assembly and packing, as defined by their individual structures.

It was shown that the structure of NiP layers depends very strongly on their coverage on the Ag(111) surface. At a coverage of 1 monolayer (ML), NiP forms a close-packed, uniform layer, with two equivalent domains rotated by ± 6° with respect to the Ag substrate. This is an example of non-chiral molecules self-assembling into right- and left-handed two-dimensional chiral domains.
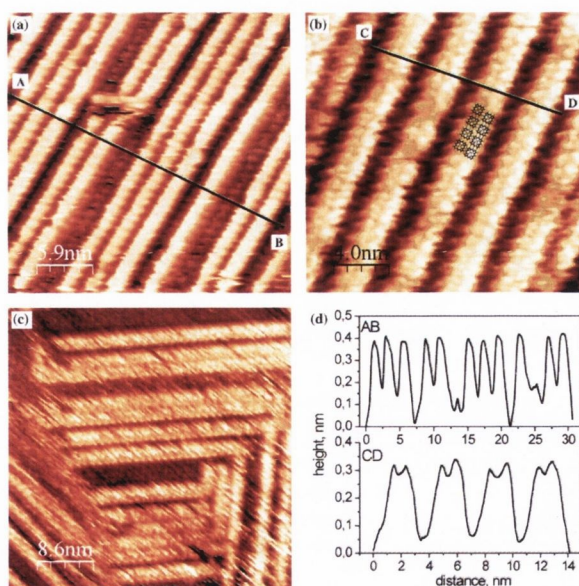
Figure 4.1: (**a–c**) STM of increasing NiP coverages on Ag(111), leading to nanolines one (**a**), two (**b**) and three (**c**) molecules wide, as shown by the line profiles in **d** [10].

At a coverage of approximately 1.5 ML, the second layer of NiP self-assembles into nanolines on top of the first molecular layer, as shown in Figure 4.1. These nanolines are very well-ordered and their length is limited only by the extent of the Ag substrate's terraces, with lengths of up to 50 nm observed. They are found to be between one and four molecules wide, depending on the total molecular coverage, and as they grow wider they begin to form a hexagonal structure with unit cell parameters similar to those obtained for the first molecular layer.
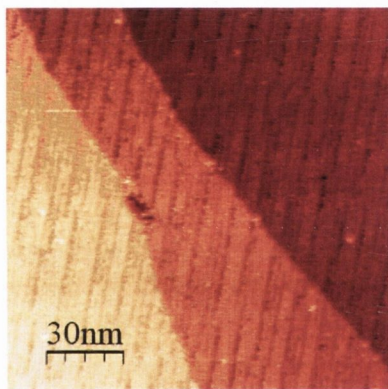
Figure 4.2: STM of approximately 1.8 ML coverage of NiP on Ag(111), showing single-molecular missing rows, separated by a periodicity of 5 nm [10].

As the coverage is further increased, the nanolines grow together laterally, and at 1.8 ML the molecules are seen to form lines with an average width of 5.0 ± 0.1 nm, with dark rows between them corresponding to a single missing molecular row (Figure 4.2). When the coverage finally reaches 2 ML, the closed hexagonal packing is restored, however the unit cell is approximately 4% larger than that of the first layer. This indicates that the molecule–substrate interaction experienced by the first layer is enough to accommodate this strain. Since it experiences less of an effect from the substrate, the

second layer undergoes a lateral relaxation compared to the first layer, and this relaxation causes some of the molecules to be displaced out of plane, resulting in a 5.0 nm modulation of the apparent height, corresponding to the filling of the missing rows in going from 1.8 ML to 2.0 ML.
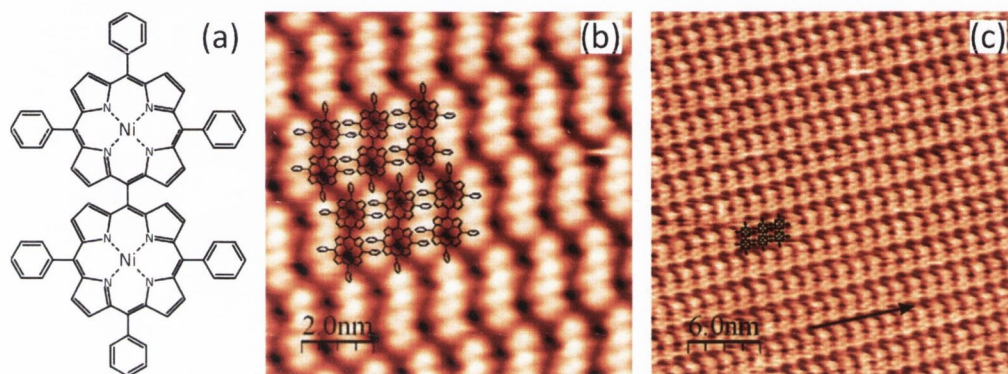
Figure 4.3: Schematic of the NiTPP-dimer molecule (a). STM of 1 ML of NiTPP-dimers on the Ag(111) surface acquired at $V_{sample} = -1.9$ V (a) and $V_{sample} = 0.65$ V (b). A negative bias allows electron tunneling from the phenyl rings, and positive bias allows tunneling into the porphyrin macrocycle [10].

In the case of the NiTPP-dimer also deposited on the Ag(111) surface, however, a different behaviour has been reported [11]. The NiTPP-dimer consists of two nickel porphyrin macrocycles connected through a single carbon–carbon bond, with phenyl rings occupying the rest of the meso-positions, as shown in Figure 4.3a. This more complex structure gives rise to an oblique close packing regime, and at a coverage of 0.5 ML, large compact islands are formed, the edges of which appear "blurry" due to tip-induced molecular movement. This, and the relatively low desorption temperature of 500 K implies that they form a weakly bonded, physisorbed system.

When the coverage is increased to 1 ML the molecules form oblique closed domains, with lattice parameters of $a = b = 2.7$ nm and $\gamma = 70°$, and aligned

along the main crystallographic directions of the Ag(111) surface. Figure 4.3b shows an STM image of such a monolayer, obtained at a bias voltage of $V_{sample} = -1.9\,\text{V}$, where the central macrocycles appear as dark areas and the phenyl rings are imaged as bright protrusions. It can be seen that the dimers are very closely packed, with the phenyl rings rotated by 50–60°, allowing them to interlock and form intermolecular bonds through π-electron stacking of the phenyl rings.

By performing STM at a negative sample bias, as in Figure 4.3b, the occupied molecular orbital states are probed, and when tunneling at a positive sample bias, as in Figure 4.3c, the unoccupied states are examined. The published electronic structure of nickel porphyrin indicates that the first unoccupied molecular orbitals are localised within the macrocycle, and the occupied molecular orbitals within the phenyl substituents.

In contrast to noble metal surfaces, when deposited on bare or lightly-passivated semiconductor surfaces, organic molecular mobility is severely restricted even at room temperature, and isolated molecules can be stably imaged [179, 180]. This allows the conformational effects of the substrate to be probed without interactions from the molecule's neighbours. On a highly boron-doped Si(111) surface, Cu-5,10,15,20-tetrakis(3,5-di-tert-butyl-phenyl) porphyrin (CuTBPP) strongly binds to the surface and undergoes some conformational adaptations due to the interaction with the substrate [180]. A similar pinning of the molecules is observed when phthalocyanines interact with defects on the H-passivated H:Si(001) surface [175, 176, 176].

On the passivated H:Si(001) and H:Si(111) surfaces, porphyrins and related organic molecules are free to migrate across the surface, similar to the noble metal surfaces, however when they encounter a defect they become strongly attached at the defect site [176, 181]. Voltage pulses from the STM tip can induce the formation of such defects by selectively removing H atoms, and in this way it has been hypothesised that nanoscale organic electronics can be designed [182, 183].

On oxidised surfaces such as Cu(110)-p(2×1)O, the inherently achiral free-base tetraphenyl porphyrin (H_2TPP) forms heterochiral domains upon interaction with the surface. Although the H_2TPP molecule is achiral, it consists of four phenyl rings which can be rotated in a "propeller" fashion with respect to the planar macrocycle either clockwise or anticlockwise, thus giving rise to chirality. The unit cell of the molecular monolayer on the oxide-reconstructed Cu surface consists of two molecules with opposite chirality. If the unit cell was square, this would lead to an overall-achiral monolayer, however on the Cu(110)-O surface, the commensurate unit cell is oblique, leading to the formation of mirror domains on adjacent terraces [78, 177].

As mentioned before, transition metal porphyrins possess many interesting properties, however in some cases their synthesis by traditional methods can be tricky, and some oxidation states are unstable in vitro. A solution to this is to directly metallate free-base porphyrin [184–186]. This versatile technique is employed most often by depositing a free-base porphyrin or phthalocyanine such as H_2TPP onto the relatively-inert Ag(111) surface, and dosing the surface with metal atoms (e.g. Fe atoms to create Fe-TPP), and has shown yields of up to 95%, with almost all molecules converted to

the metallated form [184, 185]. Conversely metal adatoms can be deposited on the surface before porphyrin deposition, and the metalation occurs in a similar way [186]. This novel on-surface synthesis can lead to the creation of organic molecules whose metal centres have oxidation states which are inaccessible to other synthesis methods, as they are stabilised through coordination by the surface.

4.3   Ag(111) and Ag/Si(111): similarities and differences

The crystal structure of silver is body-centred cubic (Figure 4.4a), and so the Ag(111) plane exhibits a close-packed, hexagonal structure (Figure 4.4b). Ag is a stable transition metal, and one of the few metals found abundantly in nature as a pure native element. This stability is due to its relative inertness, and the Ag(111) close-packed surface has the lowest energy of its high-symmetry surfaces.

As discussed in Section 4.2, molecules on Ag(111) tend to favour close-packed arrangements where possible. Its low surface energy allows molecules to easily diffuse until they encounter either a step edge (with a higher energy due to symmetry breaking), or another molecule (with whom the intermolecular interaction is stronger than the molecule–substrate interaction), giving rise to close-packed monolayers. The surface is not completely ignored by the deposited molecules however, with the choice of substrate playing a major role in the properties of NiDPP and MnClTPP (Chapter 5).
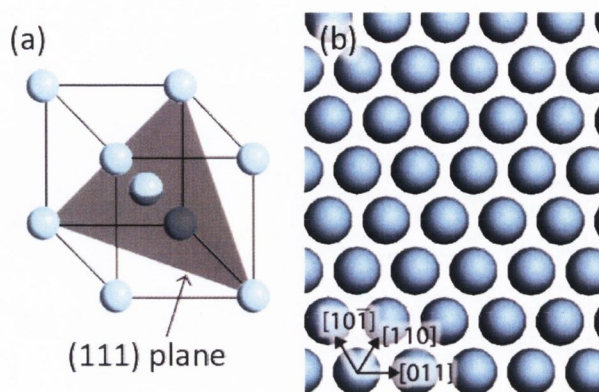
Figure 4.4: **(a)** Schematic model of the silver body-centred cubic structure, showing the (111) cleavage plane. **(b)** Model of the close-packed Ag(111) surface, with the principal directions indicated.

Ag/Si(111)-$\sqrt{3} \times \sqrt{3}$ R30° consists of the honeycomb-chain trimer structure. Cleaving the (111) surface of Si creates dangling bonds that point out of the surface into the vacuum. If it is not passivated, these bonds reconstruct into chains of dimers, however when Ag is deposited onto the Si(111) surface, it forms pseudo-hexagons on the surface, which cause the Si dangling bonds to reconstruct into trimers [187–189], as shown in Figure 4.5.

The Ag/Si(111)-$\sqrt{3} \times \sqrt{3}$ R30° surface was chosen as its reactivity is expected to be intermediate in strength between that of clean Si(111) and hydrogen-passivated Si(111) [190, 191]. On clean Si(111), porphyrin molecules form covalent bonds and are unable to diffuse or self-assemble into ordered structures at room temperature [161, 181], while on the H-passivated surface they diffuse freely and can form islands [181, 192]. The effect of the Ag(111) surface on the NiDPP self-assembly is expected to be minor, similar to that of H-passivated Si(111), however the Ag/Si(111)-$\sqrt{3} \times \sqrt{3}$ R30° surface's electron states have been shown to exhibit a resonance close to the energy of the d_{z^2} molecular orbital [193], leading to a stronger interaction with the surface,
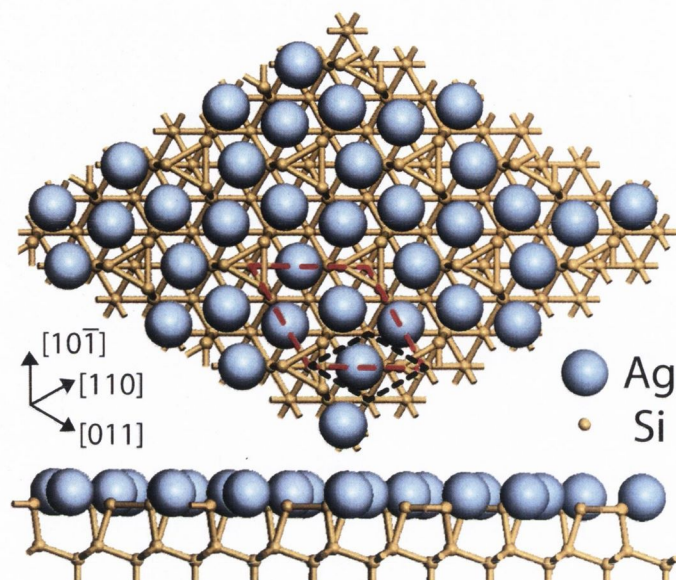
Figure 4.5: Top and side-view model of the Ag/Si(111)-$\sqrt{3} \times \sqrt{3}$ R30° surface. Ag atoms are represented by large blue spheres, and Si as small yellow spheres. When Ag is deposited on the Si(111) surface, it reconstructs to form the honeycomb-chain-trimer structure [189]. The unit cell of Si(111) is shown in black, with the $\sqrt{3} \times \sqrt{3}$ R30° reconstruction shown in red.

and the difference between the interactions with these two surfaces will be explored in this chapter.

4.4 Exploiting surface reactivity for NiDPP self-assembly

4.4.1 NiDPP: (5,15-diphenylporphyrinato)Ni(II)

The porphyrin studied in this chapter, (5,15-diphenylporphyrinato)Ni(II), consists of a central Ni-porphyrin macrocycle with two phenyl rings situated at the *meso*-positions, in the *trans* orientation, as shown in Figure 4.6.
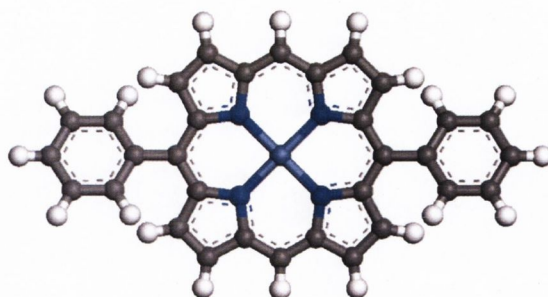
Figure 4.6: Molecular model of (5,15-diphenylporphyrinato)Ni(II), showing the porphyrin macrocycle, central Ni atom and the substituent phenyl rings.

Porphryins substituted with four phenyl rings have been extensively studied due in part to their relative ease of synthesis, and their self-assembly is well-known [194–198]. The self-assembly and axial ligand lability of a four-fold, *meso*-aryl substituted porphyrin will be described in detail in the next chapter (Chapter 5); however by investigating the self-assembly of a linear molecule such as NiDPP, interesting phenomena can arise due to its lower symmetry, such as stacking in a preferential direction, and the formation of wire-like structures.

4.4.2 NiDPP on Ag(111)

When deposited onto the Ag(111) surface, the NiDPP molecules self-assemble at room temperature into large well-ordered domains. At 1 ML coverage, each porphyrin macrocycle, which includes a central Ni atom, four surrounding pyrrole rings and four C atoms in the meso positions, has a flat orientation on the surface with the macrocycle plane lying parallel to the substrate. Figures 4.7a and 4.7b show typical occupied and unoccupied state STM images taken from the NiDPP monolayer, respectively.

Figure 4.7: STM images taken from 1 ML of the NiDPP on the Ag(111) surface: **(a)** $I_t = 0.1$ nA, $V_{sample} = 1.4$ V, 45 nm × 45 nm and **(b)** $I_t = 1.0$ nA, $V_{sample} = 1.2$ V, 13 nm × 13 nm. The unit cell of the NiDPP overlayer is shown in black. Schematic representation of the NiDPP overlayer on the Ag(111) surface **(c)**. (a) and (b) have been smoothed using a 3 × 3 matrix to remove mechanical noise.

In Figure 4.7a the phenyl substituents are seen as bright oval protrusions, while the porphyrin macrocycle appears dark. In turn, in Figure 4.7b the individual macrocycles appear as bright protrusions, each showing a four-fold symmetry and having dimensions on the order of 1 nm. Such a difference in molecular appearance in Figures 4.7a and 4.7b can be attributed to a difference in the electronic structure between the porphyrin macrocycle and the phenyl substituents and their geometry on the surface.

In Ni porphyrins, the first unoccupied molecular orbitals are localised within the macrocycle and include unoccupied Ni 3d states [199–201]. At a relatively small positive sample bias, electrons tunnel mainly into macrocycle states and not to phenyl rings, making the porphyrin core brighter than its substituents (Figure 4.7b). When tunneling occurs from a number of molecular orbitals localised within both the macrocycle and phenyl rings, the latter appear to be brighter (Figure 4.7a). This is due to the rotated position

of the phenyl rings, which makes them topographically higher than the flat porphyrin macrocycle. This simplified view does not take into account the interaction between the molecule and the substrate; however, it is assumed that this interaction is weak for the Ag(111) surface.

It is observed that each Ag(111) terrace is covered with a single molecular domain with terrace widths of up to 100 nm. The NiDPP overlayer has an oblique close-packed structure and consists of alternating molecular rows. The molecules along each row are aligned parallel to each other, while the molecules in adjacent rows are rotated by approximately 17° with respect to each other. This leads to the tilted-row pattern seen in Figure 4.7b, arising from pairs of phenyl rings aligned with one another.

The proposed model of the NiDPP monolayer on the Ag(111) surface is shown in Figure 4.7c. The unit cell of the NiDPP lattice has the following parameters: $a = 2.00 \pm 0.05$ nm, $b = 1.60 \pm 0.05$ nm, $\gamma = 85.0 \pm 0.5°$. The formation of ordered structures of this extent indicates a low diffusion barrier for the molecules on this surface at room temperature. Furthermore, a relatively weak (van der Waals) intermolecular interaction, involving the hydrogen atoms and phenyl rings of neighbouring NiDPP molecules dominates over a weaker bonding between the molecules and the Ag(111) substrate. It is noted that the molecules desorb from the surface at a temperature of approximately 430 K, which provides further evidence for a physisorbed system weakly bonded to the substrate.

As seen in Figure 4.8, the NiDPP molecular rows are oriented along the substrate step edges. The steps follow one of the close-packed directions of Ag(111), denoted here as [10$\bar{1}$], as derived from STM and LEED measured

from the clean substrate. This indicates that the overlayer growth starts from the Ag(111) step edges, which imparts a direction to the resulting molecular structure. This is a clear indication that, despite a weak molecule–substrate interaction, Ag(111) plays a crucial role in the adsorption and arrangement of the molecules.
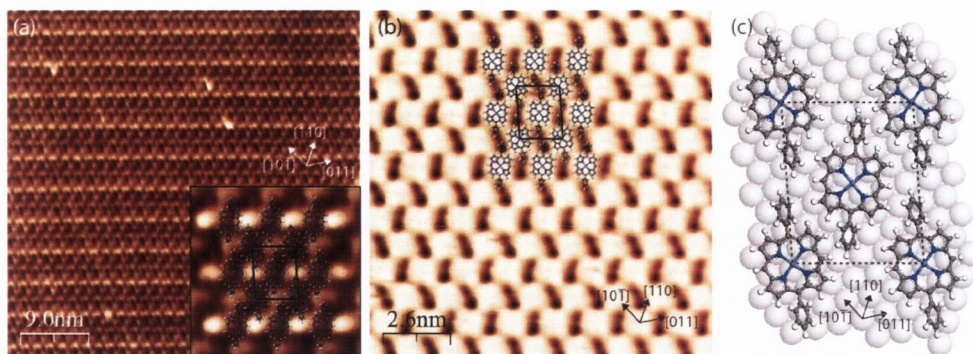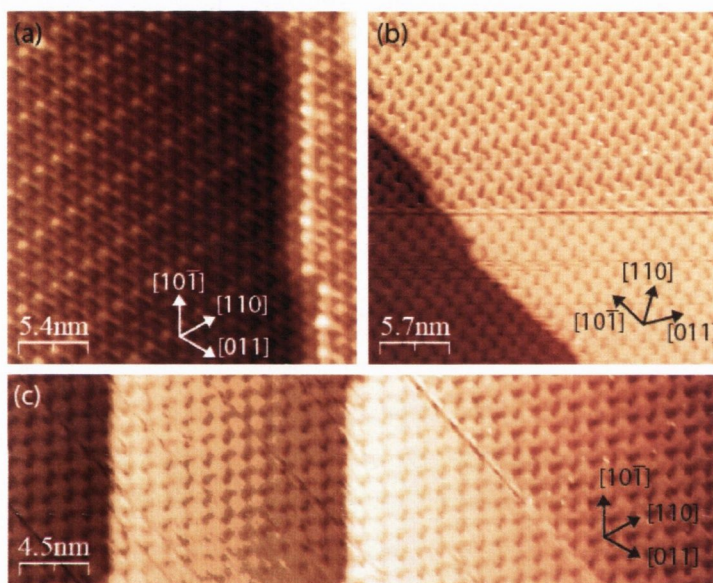

Figure 4.8: STM images taken from 1 ML of the NiDPP on the Ag(111) surface: **(a)** $I_t = 0.1$ nA, $V_{sample} = -1.4$ V, 27 nm × 27 nm, **(b)** $I_t = 1.0$ nA, $V_{sample} = 1.25$ V, 28 nm × 28 nm and **(c)** $I_t = 1.0$ nA, $V_{sample} = 1.25$ V, 50 nm × 12 nm. (b) has been flattened to correct the tip change which occurred approximately half-way up the scan and (c) has been rotated by approximately 45° to show the molecular alignment across multiple terraces, and the diagonal lines shown arise from tip instability during scanning.

A similar type of growth has been found for other molecular layers on surfaces with a relatively low reactivity [46, 202, 203]. As shown in the overlayer model in Figure 4.7c, the porphyrins and the substrate form an almost perfect 2:9 coincidence structure along the [10$\bar{1}$] direction of the Ag(111) surface, where every second molecule along this direction coincides with every

ninth silver atom. This direction coincides with the long diagonal of the NiDPP overlayer unit cell.

All STM images of NiDPP on the Ag(111) surface show the close-packed structure of the self-assembled layer with a relatively small separation between the molecules. This is a result of significant rotation of the phenyl rings, imaged as oval protrusions (Figures 4.7a and 4.8a). The plane of the phenyl rings is usually rotated by approximately 60° with respect to the macrocycle plane according to ab initio calculations, STM and X-ray absorption experiments [11, 192, 204, 205]. Such rotation allows the NiDPP molecules to approach each other on the surface in a specific manner and form an extended close-packed structure to minimize the surface energy.
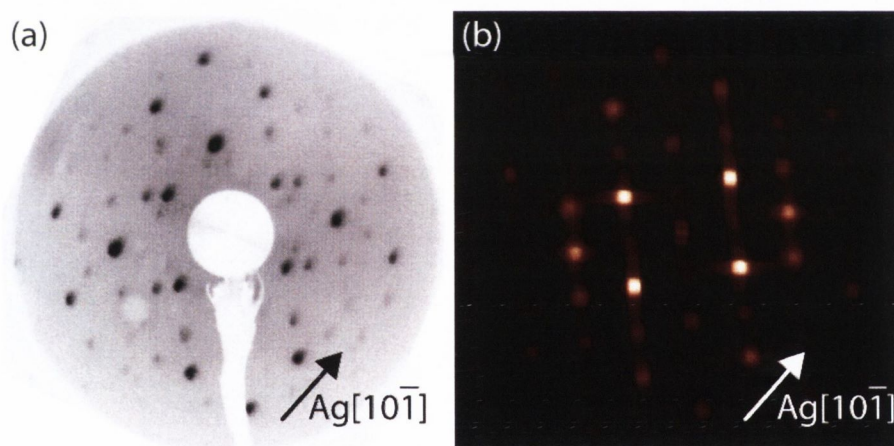
Figure 4.9: **(a)** LEED pattern from 1 ML of the NiDPP on the Ag(111) surface, acquired at a kinetic energy of 15 eV. **(b)** Two-dimensional fast Fourier transform calculated from the STM image shown in Figure 4.7a. The close-packed [10$\bar{1}$] substrate direction corresponding to the coincidence structure is indicated by an arrow.

Figure 4.9a shows a LEED pattern obtained from 1 ML of NiDPP deposited on the Ag(111) surface. This LEED pattern with an oblique unit cell

exhibits good agreement with the two-dimensional fast Fourier transform (2D-FFT) (Figure 4.9b) of the STM images. Note that although similar in concept, LEED and FFT will not agree perfectly, since LEED averages over a much larger area ($\sim$ µm) than the STM image from which the FFT is calculated ($\sim$ 10 nm), and that LEED can include contributions from the substrate and multiple scatterings. Nevertheless, this implies that the surface is covered by a single domain and that the STM images included are representative of the overlayer structure.

4.4.3   NiDPP on Ag/Si(111)

The silver-passivated Si(111) surface has a $\sqrt{3} \times \sqrt{3}$ R30° reconstruction and consists of the honeycomb-chain trimer structure, as explained in Section 4.3 [187, 188]. The reactivity of this surface lies between that of the Ag(111) and the clean Si(111). It is expected that the NiDPP interaction with the Ag/Si(111)-$\sqrt{3} \times \sqrt{3}$ R30° surface will be stronger than that of Ag(111).

Figure 4.10a shows a typical STM image of a monolayer of NiDPP molecules deposited on the Ag/Si(111)-$\sqrt{3} \times \sqrt{3}$ R30° surface. The NiDPP molecules form a close-packed structure of dimer rows on this surface. There are three domains, labelled A, B and C, observed on the same terrace in Figure 4.10a. All domains have a similar pseudo-hexagonal structure and are rotated by 120° relative to each other following the three-fold symmetry of the underlying substrate. The inset in Figure 4.10a shows in detail the close-packed structure of one domain (A).
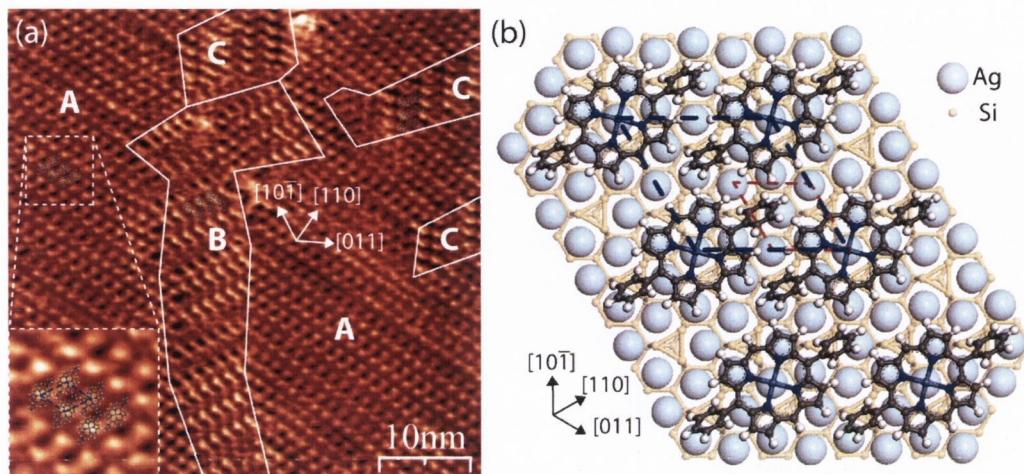
Figure 4.10: **(a)** STM image taken from 1 ML of the NiDPP on the Ag/Si(111)-$\sqrt{3} \times \sqrt{3}$ R30° surface: $I_t = 0.8$ nA, $V_{sample} = 1.35$ V, 50 nm × 50 nm. Three domains of dimer rows rotated by 120° to each other are present and are labelled A, B and C in the image. The inset shows the detailed structure of the domain A. **(b)** Schematic representation of one domain of the NiDPP overlayer on the Ag/Si(111)-$\sqrt{3} \times \sqrt{3}$ R30° surface. (a) has been smoothed using a 3 × 3 matrix to remove mechanical noise.

The existence of three different domain orientations on the same terrace of the Ag/Si(111)-$\sqrt{3} \times \sqrt{3}$ R30°, in contrast with single-domain terraces for Ag(111), implies a much stronger molecule–surface interaction, as expected for the more-reactive Ag-passivated Si(111) surface. When deposited at room temperature, the movement of the molecules on the surface is restricted, with preferential binding sites dictated by the pseudo-hexagonal structure of the underlying surface.

This results in an oblique (pseudo-hexagonal) unit cell with lattice parameters of 1.4 ± 0.1 nm × 1.3 ± 0.1 nm at an angle of 60 ± 2°. The proposed model of the NiDPP monolayer on the Ag/Si(111)-$\sqrt{3} \times \sqrt{3}$ R30° surface is shown in Figure 4.10b. It is noted that twice the distance between the Si trimers is equal to 1.33 nm. In order to minimize the number of non-

equivalent adsorption sites and the lattice mismatch, the NiDPP monolayer is stressed on this surface. This results in a slightly denser overlayer structure compared to the one observed on the less-reactive Ag(111) surface. The packing densities of the NiDPP overlayer on the Ag/Si(111)-$\sqrt{3} \times \sqrt{3}$ R30° and the Ag(111) surfaces, calculated from the proposed models, are equal to 0.67 and 0.63 molecules per nm^2, respectively.
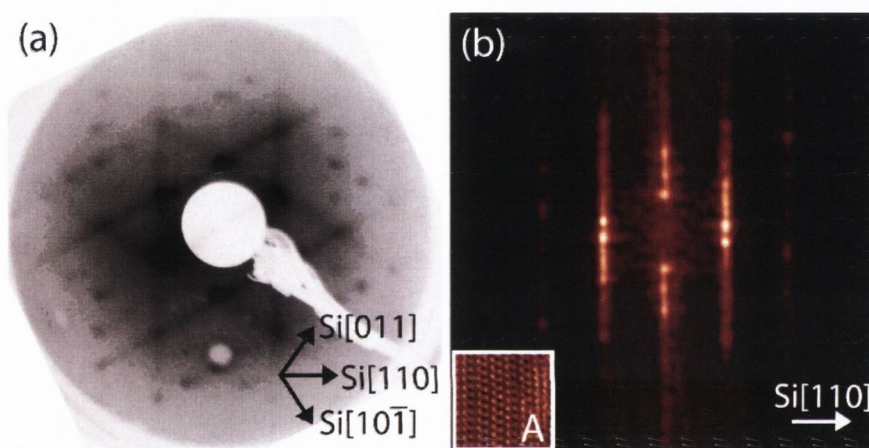
Figure 4.11: **(a)** LEED pattern from 1 ML of the NiDPP on the Ag/Si(111)-$\sqrt{3} \times \sqrt{3}$ R30° surface acquired at a kinetic energy of 25 eV. **(b)** Two-dimensional fast Fourier transform calculated from the STM image of one domain (A) shown in Figure 4.10a, indicated by the inset. The primary substrate directions are indicated by arrows, with only that of the A domain shown in (b).

Figure 4.11a shows a LEED pattern obtained from approximately 1 ML of NiDPP deposited on the Ag/Si(111)-$\sqrt{3} \times \sqrt{3}$ R30° surface. It has a pseudo-hexagonal structure confirming the presence of three domains of the molecular overlayer. By comparing the 2D-FFT calculated from the STM image of a single domain A (Figure 4.11b) with the experimental LEED pattern, it is clear that the dominant features arise from the three equivalent domains observed in Figure 4.10a, oriented at 120° to one another.

It is also evident from the symmetry that each orientation contributes equally to the LEED pattern, indicating that no one orientation is preferred over the others. This is in agreement with the STM data showing that the NiDPP overlayer structure consists of dimer rows growing in three equivalent directions, dictated by the hexagonal symmetry of the Ag/Si(111)-$\sqrt{3} \times \sqrt{3}$ R30° surface. The significant streaking of the LEED spots (Figure 4.11a), which are also visible in the 2D-FFT (Figure 4.11b), is a result of the dimer row structure observed in STM images. This streaking indicates the presence of disorder along the molecular rows and arises due to a variation in the lattice parameter of the molecular unit cell in the direction parallel to the molecular rows. This in turn is attributed to non-equivalent rotation and/or bending of the individual phenyl rings in order to minimize the lattice mismatch between the NiDPP overlayer and the substrate.

4.5   Conclusions

In summary, by using STM and LEED it has been demonstrated that the self-assembly of NiDPP molecules at room temperature depends greatly on the choice of substrate.

If deposited on the relatively-inert Ag(111) surface, molecule–molecule interactions dominate and the NiDPP molecules form a close-packed, single-domain monolayer, which starts to grow from the substrate step edges.

In contrast, on the more-reactive Ag/Si(111)-$\sqrt{3} \times \sqrt{3}$ R30° substrate, the molecule–substrate interaction is stronger than in former case, leading the deposited molecules to adopt one of three equivalent orientations on the sur-

face. These initial orientations act as nucleation sites for the three equivalent molecular domains distributed randomly over the substrate terraces.

By studying the self-assembly of a simple molecule such as NiDPP on a wide range of substrates, it becomes possible to make predictions as to the probable supramolecular ordering of more complex molecules on those surfaces. This kind of work is fundamental to our understanding of molecule-substrate interactions, and will form the basis of molecular electronics in the future.

Chapter 5

MnClTPP on Ag(111): Axial Ligand Transformations

3d transition metal porphyrins are ideal candidates for a large number of applications due to their rich coordination chemistry [206]. In particular, manganese-based porphyrin complexes have been shown to selectively catalyse the halogenation of C–H bonds [207] and are often used as catalysts for the chemical transformation of alkenes into epoxides [208, 209]. By using electronegative ligands, the metal atom can be oxidized from the +2 to the +3 oxidation state. Given the capabilities of porphyrins to bind and release gases and to act as an active center in catalytic reactions in biological systems, porphyrin-based films on surfaces are extremely appealing as chemical and gas sensors as well as nanoporous catalytic materials [210, 211].

In this chapter, STM, DFT calculations, XAS and XPS are used to study the reaction of molecular oxygen with the surface supported monolayer (ML) of (5,10,15,20-tetraphenylporphyrinato)Mn(III)Cl (MnClTPP).

When deposited onto the Ag(111) surface, MnClTPP form a close-packed square monolayer. The molecules adopt a saddle conformation, with the axial Cl-ligand pointing out of the plane into the vacuum.

Upon annealing at ~510 K, the Cl ligand desorbs from the MnClTPP molecule, however the (III) oxidation state of the central Mn ion is unchanged. This oxidation state is stabilised through ligation by the substrate. Exposure of the Mn(III)TPP layer to molecular oxygen oxidises the metal centre to the Mn(IV) state, and the molecule binds both oxygen atoms as a peroxide, to form Mn(IV)O$_2$TPP. Finally, this bidentate peroxide ligand can be removed by further annealing to ~445 K, refreshing the monolayer to the Mn(III)TPP/Ag(111) state.

5.1   Experimental details

The STM experiments were performed at 78 K in an ultra-high-vacuum system consisting of an analysis chamber (with a base pressure of 2×10^{-11} mbar) and a preparation chamber (5×10^{-11} mbar). An electrochemically etched polycrystalline tungsten tip was used to record STM images in constant current mode. The voltage V_{sample} corresponds to the sample bias with respect to the tip. No drift corrections have been applied to any of the STM images presented herein.

The Ag(111) crystal (Surface Preparation Laboratory) was cleaned in situ by repeated cycles of argon ion sputtering ($E_k = 0.8$ keV) and annealing at 820 K. The substrate cleanliness was verified by STM and LEED before deposition of the MnClTPP. MnClTPP was synthesized according to a published

procedure [212] by Dr Natalia Sergeeva in the School of Chemistry, TCD. The molecules were evaporated in a preparation chamber isolated from the STM chamber at a rate of about 0.2 ML per minute from a tantalum crucible in a homemade deposition cell operated at a temperature of approximately 600 K. The total pressure during porphyrin deposition was in the 10^{-10} mbar range. Before evaporation, the NiDPP powder was degassed for about 10 hours to remove water vapour.

XAS and XPS measurements were performed at the D1011 beamline at MAX II storage ring in Lund, Sweden by Dr Sergey Krasnikov and Dr Tony Cafolla, and their work and guidance are gratefully acknowledged. The XPS spectra were measured with a Scienta SES-200 electron energy analyzer. The kinetic energy resolution was set to 100 meV for the Cl 2p spectra. The photon energy resolution was set to 150 meV at the Mn L$_3$-edge ($\sim$640 eV). The XAS spectra were recorded in the partial electron yield mode ($U = -100$ V) by a multichannel plate detector and normalized to the background curves recorded from the clean substrate.

DFT calculations were performed under the guidance of Dr Olaf Lübben using the Vienna *Ab initio* Simulation Package (VASP) program. VASP implements a projected augmented basis set (PAW) [70] and periodic boundary conditions. The electron exchange and correlation was simulated by generalised gradient approximation (GGA) pseudopotentials with a Perdew-Burke-Ernzerhof (PBE) exchange-correlation density functional [62]. A single k-point (Γ) was used for all calculations to sample the Brillouin zone. The applied energy cut-off was 400 eV. The global break condition for the

electronic self-consistent loops was set to a total energy change of less than 1×10^{-4} eV, and all conformations were fully relaxed (forces < 0.01 eV/Å).

5.2 MnClTPP: (5,10,15,20-tetraphenylporphyrinato)-Mn(III)Cl

In nature, the cytochrome P450 (CYP) superfamily is a diverse group of enzymes for the oxidation of organic substances. CYPs are proteins based around a heme centre – an Fe(III)-containing porphyrin – and are utilised in many detoxification and biosynthesis pathways [213]. Learning from nature, many biomimetic systems containing Fe(III) or Mn(III) have been studied [214], and have been adapted for use in oxidation chemical reactions [210].

The chemical structure of the porphyrin (5,10,15,20-tetraphenylporphyrinato)Mn(III)Cl is shown in Figure 5.1a. It consists of a porphyrin macrocycle with a Mn core and four phenyl rings attached at the 5, 10, 15 and 20 *meso*-positions. The Mn ion is in the (III) oxidation state, and is bonded to a Cl ligand pointing out of the plane of the molecule [195]. Also shown in Figure 5.1b is the 3-dimensional model of the molecule on the Ag(111) surface. The molecule's conformation has been relaxed using DFT calculations and the final optimised atomic positions are shown.

Hulsken *et al.* have for the first time observed the real-time catalysis of an oxidation reaction by a related, MnCl-centred porphyrin (designated Mn1) using liquid-cell STM [211]. The molecule used was very similar to that in
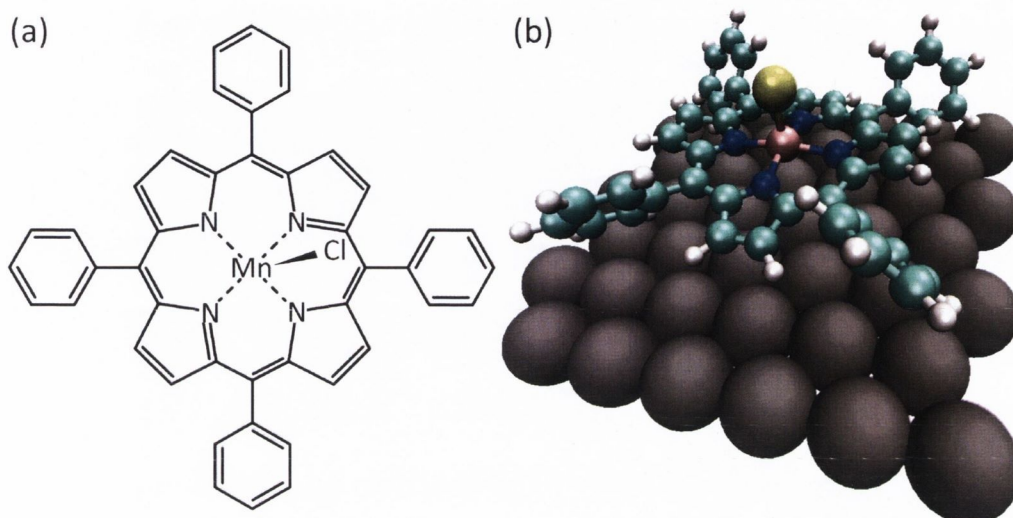
Figure 5.1: **(a)** The symbolic structural model of MnClTPP. The Mn–Cl bond points out of the plane of the molecule. **(b)** Relaxed ball-and-stick model of the MnClTPP molecule on the Ag(111) surface. The phenyl rings are rotated relative to the macrocycle, and the Cl atom points out into the vacuum.

Figure 5.1a, however the phenyl rings at the *meso*-positions are replaced by long, greasy $C_{11}H_{23}$ chains to increase its solubility, as shown in Figure 5.2a.

The Mn1 molecules adsorb onto the Au(111) surface in regular arrays, and most molecules exhibit a uniform height. However, in Figure 5.2c, a single molecule shows a larger apparent height. This was attributed to some residual O_2 contaminant in the solvent oxidising the Mn1 molecule. The authors note that due to the planar orientation on the surface, and the fact that the free-base porphyrin derivative of Mn1 does not adsorb at the same interface, it is likely that a Au atom of the surface is coordinated to the Mn centre [215].

Similarly, it was shown that O_2 did not react with the Mn1 compound in solution without the presence of the surface, indicating that the Au acts
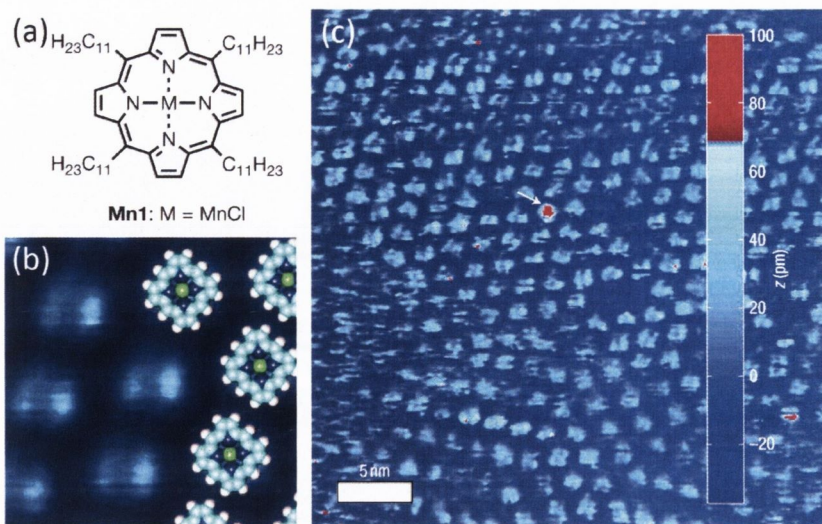
Figure 5.2: **(a)** Mn1 molecule with a MnCl centre, similar to that of Mn-ClTPP. **(b)**, **(c)** Liquid-cell STM images of Mn1 deposited onto an Au(111) surface grown on a mica substrate. The arrow in (c) points to a single molecule in the scan area which has been oxidised by residual oxygen. The solvent used was tetradecane and the experiments were performed in an argon atmosphere. $V_{sample} = 0.2\,V$ $I_t = 2\,pA$ [211].

as an electron-donating ligand [214]. In order to study the oxidation of the Mn1 monolayer, the authors purged the Ar atmosphere from their system by backfilling with O_2 gas, and a sharp increase in the "bright" molecules was observed, implying that these correspond to oxidised Mn1 complexes, as shown in Figure 5.3a.

The mechanism proposed consists of the surface Au atom coordinating to the Mn centre as an axial ligand and causing the Cl ligand to dissociate as a Cl radical, thus reducing the metal centre from Mn(III) to Mn(II). This then allows the reduced Mn1 to bind to an O_2 molecule and split it between its own metal centre and that of its neighbour, forming two Mn1=O complexes.

In order to test whether the oxidation of the Mn1 monolayer was random (i.e. each oxidation event is independent of its neighbouring molecules)
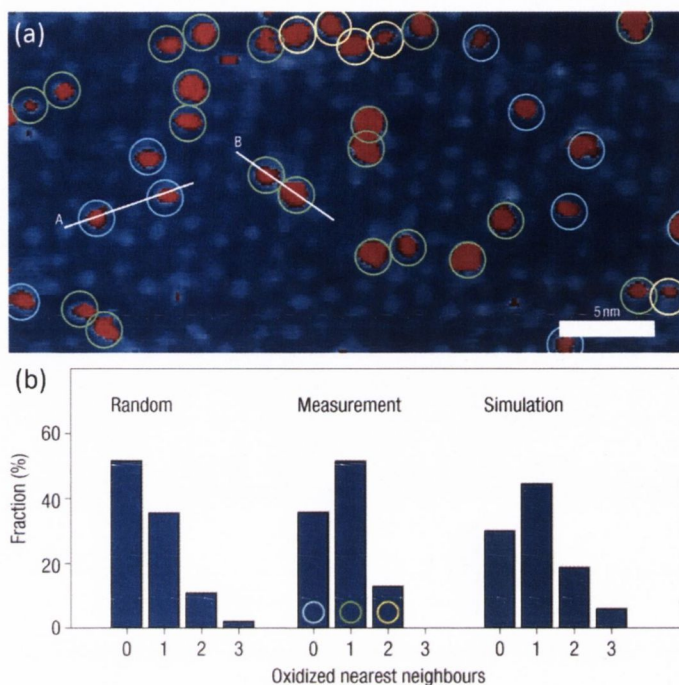
Figure 5.3: **(a)** STM image of the Mn1 monolayer after a large proportion of the molecules have been oxidised. **(b)** Histograms showing the number of oxidised neighbours surrounding an oxidised molecule, according to a random distribution, the experimental measurements, and a simulation assuming the splitting of O_2 by adjacent molecules [211].

or whether one O_2 molecule was capable of oxidising two Mn1 molecules, simulations were performed and the number of oxidised neighbours of each oxidised molecule was counted. The results are shown in Figure 5.3b, and it is clear that the distribution of oxidised molecules is not random, and instead a pairwise oxidation is favoured.

The final result of this work was the observation of an epoxidation reaction catalysed by the oxidised Mn1 layer, where a sharp decrease in the number of oxidised molecules accompanied the introduction of a precursor molecule, and subsequent analysis of the solution showed the expected epoxide reaction product. Although this seminal paper was conducted in solution,

many concepts are common to the present chapter, such as the dissociation of the Cl ligand from MnClTPP, the axial coordination of the dissociated Mn(III)TPP complex by the Ag(111) surface and the subsequent oxidation of the molecules. These results will be elucidated over the following pages.

5.3   MnClTPP self-assembly

Although the self-assembly of MnClTPP has been previously studied by Beggan *et al.* [195], the following high-resolution images reveal some new behaviour not reported by Beggan and colleagues.

When deposited onto the Ag(111) surface, the MnClTPP molecules self-assemble into close-packed structures (Figure 5.4). Although at low coverages the Ag step edges are decorated, the majority of the growth occurs in the middle of terraces, forming large, often rectangular islands, with a square packing geometry and two equal lattice parameters of $1.41 \pm 0.05\,$nm.

The supramolecular ordering of a deposited porphyrin overlayer has been shown to be mostly triggered by the molecule's side groups; indeed a similar packing scheme, with the same geometry has previously been reported for tetraphenyl-porphyrins (TPPs) with different metal centres on noble surfaces: Co- and Fe-TPP on Ag(111) [196, 197]; and Ni-, Cu- and Co-TPP on Au(111) [198], and the current data agree with those reported by Beggan *et al* [195].

LEED taken from 1 ML of MnClTPP on the Ag(111) surface, published by Beggan *et al*, shows a series of 12 spots arranged in a circle [195]. A similar LEED pattern was observed for our system (not shown). These 12
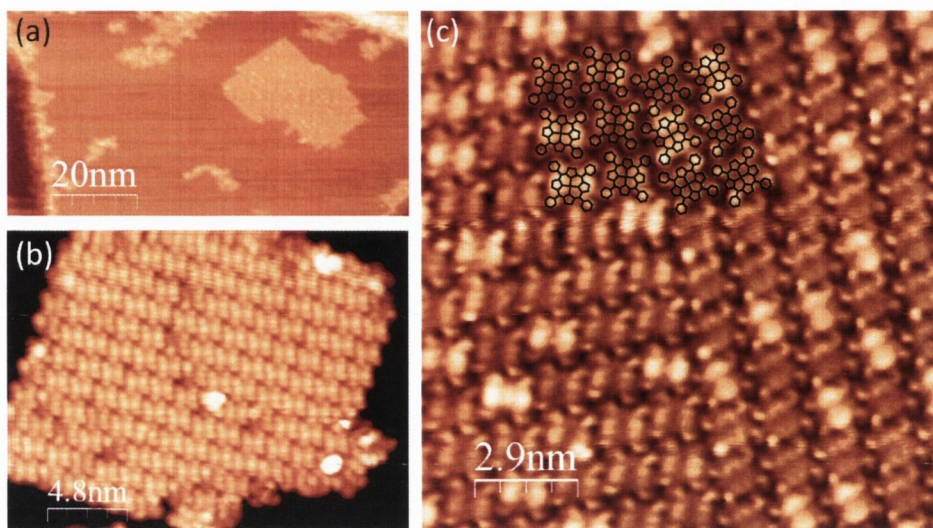
Figure 5.4: **(a, b)** STM images of ∼0.15 ML of MnClTPP. In contrast to the case of NiDPP (Chapter 4), the MnClTPP molecules self-assemble into close-packed islands. As can be seen in (a) the step edges are decorated by molecules, but the main growth occurs in the middle of the terrace as a rectangular island. **(c)** STM of a monolayer island, showing the chirality within the molecular overlayer. Inset shows a schematic model of the two chiral domains. (b) and (c) have been smoothed using a 3 × 3 matrix to remove mechanical noise.

spots are formed by 3 equivalent squares each rotated by 30°, corresponding to the three simple-cubic domains of the MnClTPP monolayer.

One side of each square lies parallel to one of the close-packed directions of the Ag(111) reciprocal unit cell, indicating that although the monolayer growth does not begin at the step edges, in contrast to the case of NiDPP, the substrate still plays a role in the self-assembly. Again, a similar arrangement has been observed for other TPPs on Ag(111), with the substrate imparting a direction to the overlayer primitive unit cell, and also one of the molecular axes lying parallel to a close-packed Ag(111) direction [196, 197].

Although LEED indicates that three rotational domains coexist on the surface, figure 5.4c shows the boundary between two domains in the Mn-ClTPP monolayer, with the same orientation of unit cells. It is evident that the two domains are nevertheless different from one another in that they cannot be transformed from one to the other by simple rotation or translation, only by a mirror operation, i.e. they are chiral enantiomers of one another.

It has previously been shown that achiral molecules deposited on an achiral surface can give rise to chirality in the adsorbed layer [78, 216–218]. Indeed, Buchner et al. have recently described the local organisational chirality of TPP monolayers in some detail, and a similar treatment is applicable here [194].

It is noted that in this study of MnClTPP, as in Buchner's work, the only domain boundaries observed within the closed monolayer were between chiral domains with the same unit cell orientation. Boundaries between any of the three orientational domains indicated by LEED were not observed together on the same terrace, but monolayers with the three different orientations were observed separately. This follows from Buchner's hypothesis that chiral domain boundaries, where the molecules are arranged in a "zipper" fashion are more energetically favourable than orientational domain boundaries, and that the activation energy for the rotation of an entire chiral domain to align with its neighbouring domain is less than that required to rotate all the individual molecules in a domain to give them the same chirality.

The molecules are rotated by $15 \pm 2°$ with respect to the close-packed directions of the monolayer. Again, a similar azimuthal rotation has been observed for Co- [194, 196], Fe- and free-base-TPP [194] on Ag(111), indicat-

ing that this rotation arises from interactions between the TPP peripheral groups.

Such a rotation allows the phenyl rings of adjacent molecules to interact in the so-called "T-shape" configuration, where the edge of one phenyl ring is directed toward the π-cloud on the face of its neighbouring phenyl ring [219]. This accounts for a strongly attractive interaction between molecules and plays a major role in their self-assembly, and has been noted to play a key role in both biological and chemical recognition and the interactions between the aromatic side-chains of proteins [220–222].

The molecules' phenyl rings have an axis of rotation around the single C–C bond joining them to the macrocycle. In order to match the molecular appearance from STM images, two of the phenyl rings were rotated in the opposite direction to the other two. We will refer to this as the "trans" conformation, shown in Figure 5.5a (bottom), distinct from the "cis" conformation where all four phenyl rings are rotated in the same direction, shown in Figure 5.5a (top).

This "counter-rotation" gives rise to some steric hindrance due to the phenyl rings' proximity to the porphyrin centre. In turn, the macrocycle adopts a saddle conformation, with the outer carbon and hydrogen atoms of the pyrrole rings being pushed into or out of the plane of the molecule.

As an aside, one might naïvely assume that meso-aryl substituted porphyrins in the gas phase would assume a conformation with the phenyl rings rotated by 90° to the porphyrin macrocycle in order to minimise steric hindrance. However, steric hindrance is only half of the story. Calculated structures comparing H_2P (free-base porphine), H_2TPP and their diacid analogues
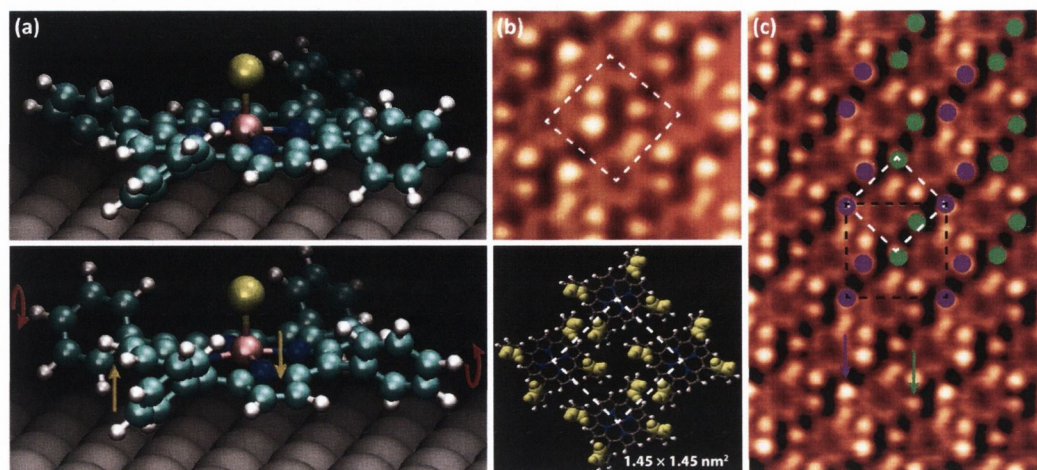
Figure 5.5: **(a)** Relaxed models of MnClTPP on Ag(111) showing the *cis* (top) and *trans* (bottom) arrangements of the phenyl rings. Yellow arrows in the bottom frame highlight the saddling of the macrocycle, and red arrows show the rotation of the phenyl rings. **(b)** STM (top) and model (bottom) of the primitive 1×1 unit cell of MnClTPP. The uppermost atoms of the phenyl rings are highlighted to show that these correspond to the brightest features in the STM image. **(c)** STM of 1 ML of MnClTPP, with a schematic showing the buckling in the monolayer overlayed. The white dotted line shows the primitive 1×1 unit cell, and the black dotted line shows the $\sqrt{2} \times \sqrt{2}$ R45° unit cell. The coloured dots and arrows highlight the "upper" phenyl rings (purple) and "lower" phenyl rings (green) of the molecules.

have shown that phenyl substituent rotation is frequently accompanied by pyrrole ring saddling in order to increase π-electron coupling between the phenyl rings and the porphyrin macrocycle, reducing the overall potential energy of the molecule [223].

Since the occupied state STM images of MnClTPP are dominated by the phenyl rings, these features are used to support the saddling hypothesis. It is clear from Figure 5.5b that the brightest (upper) portions of the phenyl rings are not evenly spaced around the periphery of the molecule, as they would be in the "*cis*" phenyl conformation. Instead, the bright protrusions are arranged at the corners of a rectangle, implying that the upper parts of

the phenyl rings are tilted towards one another along the short side of the rectangle. This conformation is supported by DFT, with the saddle-shaped molecule (Figure 5.5a, bottom) having a total energy 5 meV/atom lower than the planar conformation.

As shown in the schematic comparison between the upper STM image in Figure 5.5b and the model below, this *trans* conformation reproduces the packing of the molecules very well, with the upper-most parts of the phenyl rings highlighted as these are the brightest features on the STM image due to their proximity to the tip.

Such a saddling of the porphyrin molecule is generally accompanied by a difference in the apparent height of the pyrrole rings' features as observed by STM [194], however at the sample bias $V_{sample} = -1.4$ V, the macrocycle appears to have a mostly uniform height.

Also noted in STM images is some "buckling" in the monolayer. This is illustrated in Figure 5.5c. The purple and green arrows point to two phenyl rings with inequivalent heights within the same molecule.

This buckling of the monolayer can be described by a $\sqrt{2} \times \sqrt{2}$ R45° unit cell. This is shown in black in Figure 5.5c, and the two inequivalent "types" of phenyl rings are shown by purple and green circles.

A $\sqrt{2} \times \sqrt{2}$ R45° unit cell was also suggested by Beggan and colleagues in order for the molecular overlayer to lie commensurate to the Ag(111) surface, with the corner molecules situated directly above a substrate atom and the central molecule situated on a bridge site between two Ag atoms, however they did not observe buckling in the monolayer [195].

It is unclear whether this so-called "buckling" is caused by the plane of some molecules deviating from a parallel orientation with the surface, or by one phenyl ring of each molecule being tilted almost perpendicular to the molecular plane, however from previous studies of porphyrin complexes on noble metals [194, 196, 198], and the strength of the interaction between such molecules and the surface, it is suggested that the latter is the case.

The interaction between the π-system of the macrocycle and the substrate has already been mentioned, and its significance is seen in the fact that the molecular unit cell and the axes of the molecules themselves are aligned along close-packed directions of the surface. It is therefore clear that the strength of this interaction is much larger than the energy required to rotate one phenyl ring around a single C–C bond. This likely comes about in order to relieve some strain on the molecular layer and to facilitate a closer edge–face interaction between neighbouring phenyl rings.

5.3.1 Bias dependence of axial ligand resolution

Occupied-state STM images of the MnClTPP monolayer obtained at negative sample biases (Figure 5.6a) show the molecules as four bright protrusions, corresponding to the phenyl rings, surrounding the porphyrin core, which appears as a darker ring with a dark centre. This is consistent with previous studies of metallo-porphyrins showing that the occupied molecular orbitals are mostly localised within the phenyl rings [195, 199–201]. Similarly, it has been shown for Co-TBrPP that in the saddle conformation, the Co d_{z^2} orbital did not contribute to the HOMO of the molecule observed by STM [224],

resulting in a dark centre giving further evidence for the proposed MnClTPP

saddle conformation.
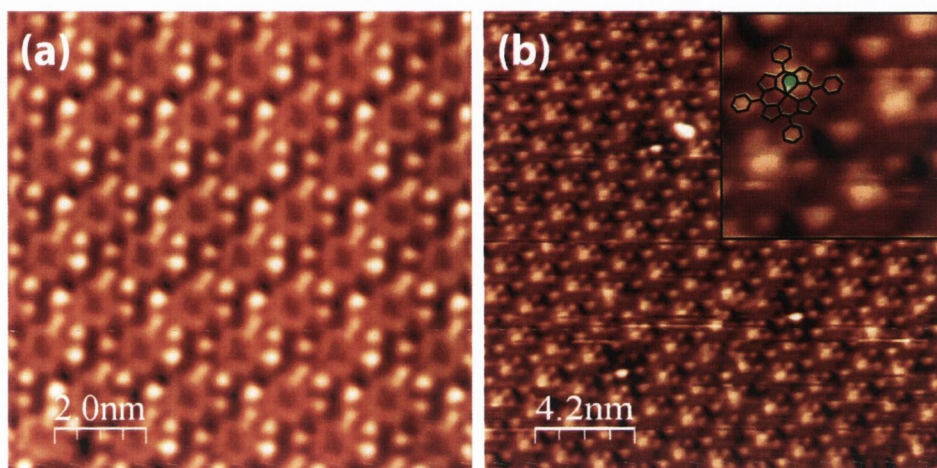
Figure 5.6: **(a, b)** STM images of 1 ML of MnClTPP. Depending on the bias chosen, the centre of the molecules appear dark (a, $V_{sample} = -1.4\,\mathrm{V}$, $I_t = 0.3\,\mathrm{nA}$), or they have a bright protrusion (b, $V_{sample} = 2.0\,\mathrm{V}$, $I_t = 0.2\,\mathrm{nA}$) corresponding to the central Cl ligand. Inset in (b) shows a zoom of several MnClTPP molecules with the molecular model overlaid. (b) has been smoothed using a 3×3 matrix to remove mechanical noise, and some horizontal scarring has been corrected.

In contrast, when the unoccupied states of the molecules are probed at

positive a sample bias (Figure 5.6b), the molecules show a bright protrusion

in the centre corresponding to the Cl-ligand pointing out of the surface (green

oval in inset). In the previous study of this system, the Cl-ligand was not

resolved, however it is noted here that only under the specific tunneling

conditions used in Figure 5.6b was it possible to observe the axial ligand.

Measurements were performed at 78 K, and so the thermal stability of the

molecules during the current experiments was greater than that of Beggan

and co-workers' room temperature work, also contributing to the ability to

image the axial ligand.

This is the first direct indication that the MnClTPP molecules arrive at the Ag(111) surface with the Cl-ligand intact, however Beggan and co-authors have shown that the chemical environment of the Cl atom is consistent with coordination to the central Mn atom, and not reacted with the Ag(111) surface [195]. They therefore propose that the Cl-ligand points out of the surface into the vacuum, and the current results are in agreement with this theory.

5.4   Axial ligand transformation

X-ray absorption spectroscopy (XAS) performed on the as-deposited Mn-ClTPP exhibits the characteristic shape of the Mn(III) oxidation state, as shown in Figure 5.7 (bottom spectrum).

The Mn $2p_{3/2}$ (L_3) XAS edge consists of three features, labelled A, B and C in Figure 5.7. These correspond to a convolution of the interactions between the core 2p electrons with the outer valence electrons, and have been shown to reflect the oxidation state of the Mn ion [225, 226]. However, the decomposition of such spectra is complex, involving up to 7 individual peaks [227], and so the main features will be treated as a "fingerprint" of the oxidation state here. When the Mn ion is in the (III) oxidation state, the B feature dominates, with a significant contribution from A and a lower shoulder at C, as shown in the initial and final spectra in Figure 5.7. In the Mn(IV) state, the contribution of the C feature dominates.

When the Mn(III)ClTPP ML is annealed at 510 K, the Cl ligand is removed but from the shape of the XAS (red curve) it is clear the oxidation
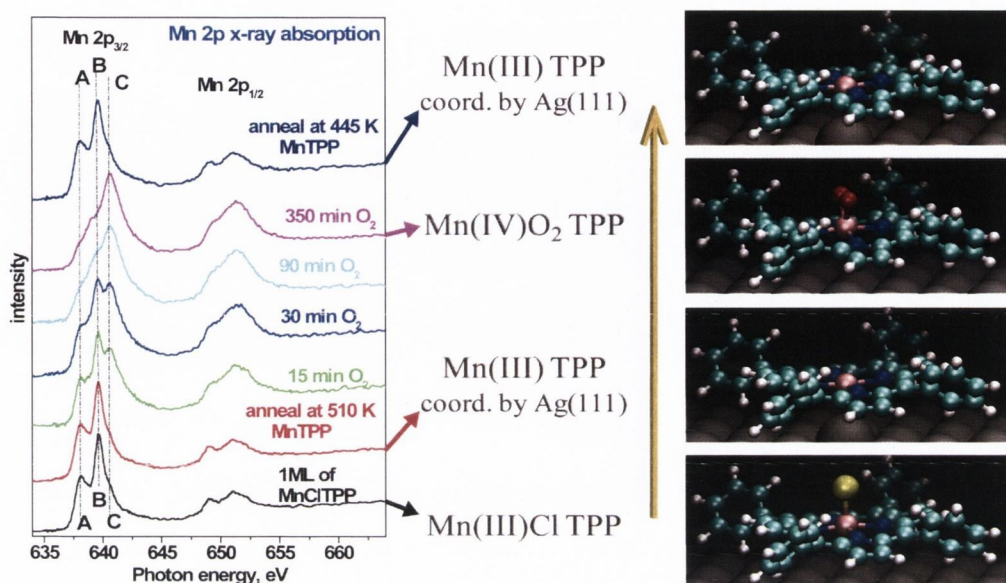
Figure 5.7: Mn 2p XAS spectra acquired during the anneal and oxygen exposure of the Mn(III)ClTPP monolayer. Initially the Mn L_2 and L_3 peaks have a shape characteristic of the Mn(III) oxidation state, which is preserved upon annealing at 510 K to yield Mn(III)TPP. Upon exposure to O_2, however, the central Mn shifts to the Mn(IV) oxidation state, and the O_2 binds to the molecule as a peroxide. The Mn(III)TPP state can then be regenerated by further annealing at 445 K. Relaxed models of the different molecules are shown beside each spectrum, and the yellow arrow indicates the order in which the experiment was performed.

state of the Mn ion is unchanged. Without the Cl ligand, the Mn(III) ion would be undercoordinated by only the porphryin macrocycle alone. It is suggested that the Mn is coordinated by the Ag(111) surface, which acts as a fifth ligand for the Mn ion, stabilising the (III) oxidation state. A similar hypothesis has been put forward for previous studies of axial ligand transformation [195, 211, 228], with an atom of the noble metal surface ligating to the transition metal core.

Upon subsequent exposure of the Mn(III)TPP/Ag(111) complex to O_2, the Mn 2p lineshape changes significantly. As oxidation time increases, the

relative contributions of the A and B features diminish, and the C peak grows to be the principal feature. This implies that exposure to oxygen causes the Mn ion to change from the III oxidation state to the IV. Also noted are clear changes in the Mn $2p_{1/2}$ peak, which are harder to quantify, but nevertheless support the oxidation of the Mn core.

It is postulated that the oxygen molecule binds to the Mn(IV) ion intact as the peroxide anion, O_2^{2-}, with the two O atoms sharing a single bond and the anion bound to the Mn centre, and this will be shown in detail in the following sections. The Mn oxidation is reversible however, and further annealing at 445 K removes the bidentate peroxide ligand, restoring the Mn(III) lineshape.

5.4.1 Removing the Cl-ligand

STM performed after the initial anneal step to remove the Cl-ligand is presented in Figure 5.8. The occupied-state appearance of MnTPP (Figure 5.8a) appears almost identical to that of MnClTPP prior to annealing.

The four phenyl rings are still visible and the centre of the macrocycle appears dark, as in Figure 5.6a, and the monolayer exhibits unchanged square lattice parameters of 1.41 ± 0.05 nm. The rectangular arrangement of the phenyl rings is also unchanged, implying that the removal of the axial ligand does not greatly affect the aryl-group substituents. However, when the unoccupied states are probed at a positive sample bias (Figure 5.8b), the molecules' appearance is strikingly different.

The central protrusion previously seen is gone, giving further evidence for the removal of the Cl-ligand. Instead, the molecules appear as four large
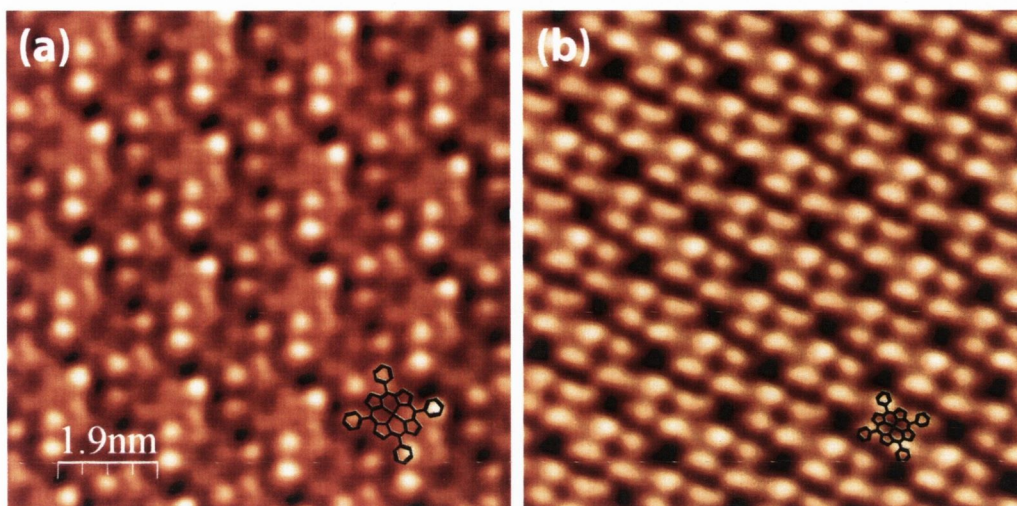
Figure 5.8: **(a, b)** STM images of 1 ML of MnTPP after annealing. The occupied state image (a, $V_{sample} = -1.4\,\text{V}$, $I_t = 0.3\,\text{nA}$) appears unchanged from the case of MnClTPP (Figure 5.6a), however when the unoccupied states are probed (b, $V_{sample} = 2.0\,\text{V}$, $I_t = 0.2\,\text{nA}$, $20\,\text{nm} \times 20\,\text{nm}$), the molecules now have dark centres, where the Cl-ligand was previously visible. These images have been smoothed using a 3×3 matrix to remove mechanical noise.

protrusions, corresponding to the positions of the phenyl substituents. The "buckling" described in a previous section is still visible in both the occupied and unoccupied state images, suggesting that it is topological in nature (i.e. a rotation of one phenyl ring out of the surface), however in the latter case it is less pronounced.

In order to examine the behaviour of the MnTPP molecules after the Cl-ligand is removed, Mn(III)TPP on Ag(111) was simulated using DFT, and the relaxed model is shown in Figure 5.9, along with the relaxed model of Mn(III)ClTPP. In the simulation, four layers of Ag were used, with the lower two constrained to simulate the bulk. The molecules were placed on top of the Ag(111) surface and allowed to relax along with the top two layers of Ag.

A vacuum slab of 10 Å was used to separate the system from its translational images.
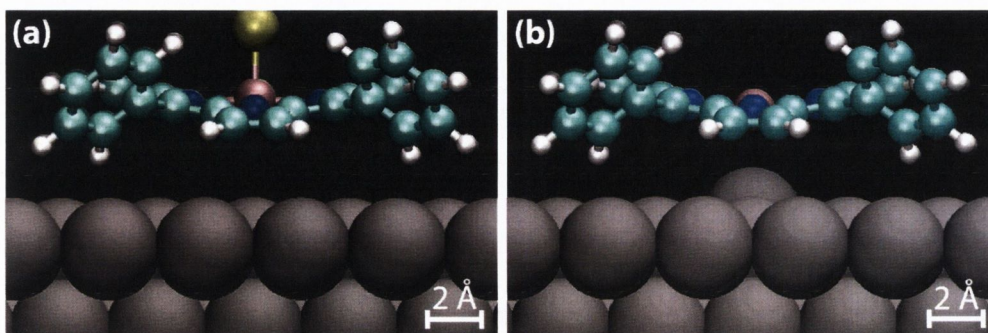
Figure 5.9:   Relaxed models calculated for Mn(III)ClTPP **(a)**, and Mn(III)TPP **(b)**, on Ag(111). After the Cl-ligand is removed, the central Mn ion is situated closer to the surface, and a Ag atom is pulled upwards towards the Mn, thus forming a fifth ligand for the transition metal, and stabilising its III oxidation state.

As can be seen from the side-views in Figure 5.9a and b, the removal of the Cl-ligand has little effect on the porphyrin macrocycle and its phenyl substituents, consistent with STM images.

The Mn centre in Mn(III)TPP, however, is situated 3.4 pm closer to the Ag(111) surface, and in turn the Ag atom directly below the Mn ion is pulled out of the surface towards the molecule by 8.7 pm. This supports the theory that the Ag(111) surface is indeed acting as a fifth ligand and stabilising the (III) oxidation state of the Mn ion centre.

In order to measure the activation energy required to trigger the desorption of the Cl-ligand, XPS was performed on the MnClTPP monolayer while it was annealed. The spectra obtained are presented in Figure 5.10a.
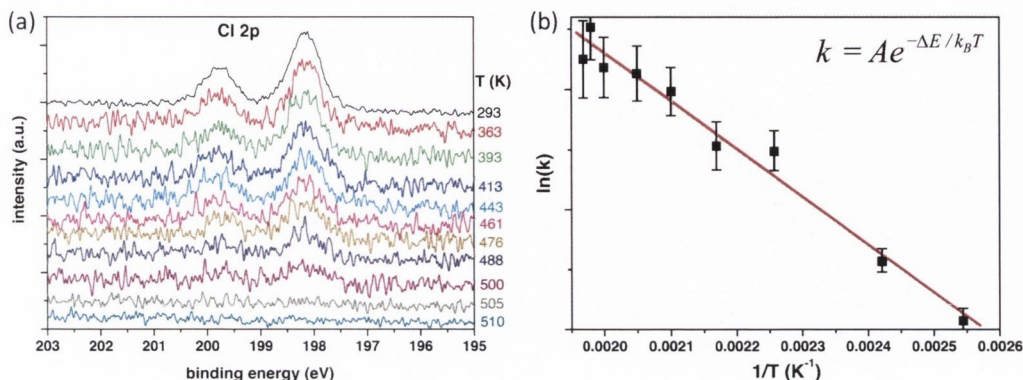
Figure 5.10: **(a)** Cl 2p XPS taken while annealing the MnClTPP molecules at varying temperatures (shown on right hand side of graph). The Cl 2p peaks are reduced to the level of the background at 510 K. **(b)** Arrhenius plot derived from the intensities taken from (a). The rate k was determined as the difference in area between two successive spectra. The slope of the fit line gives a value of $\Delta E_{Cl} = 0.35 \pm 0.02$ eV for the activation energy of the Cl-ligand desorption.

The spectra were measured while the temperature was increasing, with the temperature shown on the right of the plots. It is observed that at around 510 K, the Cl 2p peaks are reduced to the level of the background noise.

The Arrhenius rate equation (Equation 5.1) relates the rate of a reaction, k with its activation energy, ΔE and the temperature of the reaction, T.

$$k = Ae^{-\Delta E/k_B T} \qquad (5.1)$$

where k_B is the Boltzmann constant and A is the prefactor.

The two Cl 2p peaks were each fitted by a Gaussian, and the area of that fit peak was was used to calculate the rate of Cl removal, taking into account the deviation of the spectrum from the fit to calculate the uncertainties. Since the experiment was performed with a constant heating rate of 0.15 K/sec, the difference in area between two spectra can be used to derive the rate of the

desorption. $ln(k)$ vs. $1/T$ is plotted in Figure 5.10b, and the slope of the fit line gives a value for the activation energy of $\Delta E_{Cl} = 0.35 \pm 0.02\,\text{eV}$.

5.4.2   Reaction with O$_2$

After removing the Cl ligand from the MnClTPP molecules, they were exposed to oxygen gas for various lengths of time in order to study the effect of oxidation on the molecular layer.
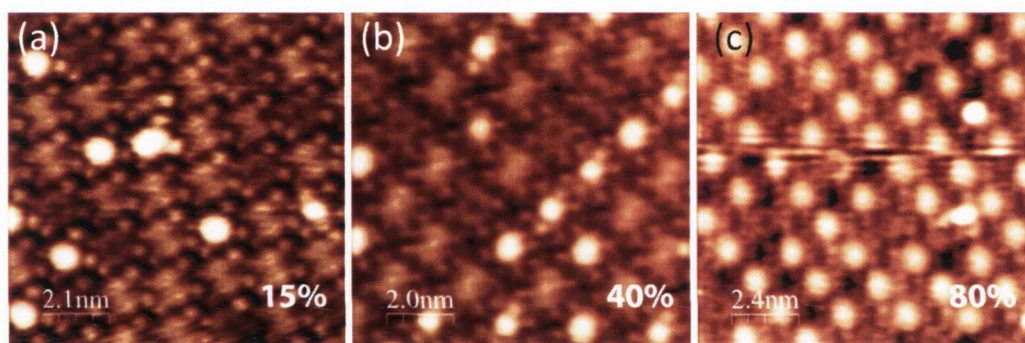
Figure 5.11: STM images of $1\,\text{ML Mn(IV)O}_2\text{TPP}$ after various oxygen exposures: **(a)** 15 minutes with ~15% of the molecules oxidised, **(b)** 30 minutes, ~40% oxidised, **(c)** 90 minutes, ~80% oxidised. $V_{sample} = -1.4\,\text{V}$ $I_t = 0.3\,\text{nA}$ in each case. (a) and (b) have been smoothed using a 3×3 matrix, and (c) by a Gaussian smooth to remove mechanical noise.

STM images recorded after 15, 30 and 90 minutes' oxygen exposure at a partial pressure of $2 \times 10^{-6}\,\text{mbar}$ are shown in Figure 5.11. It is observed that some molecules exhibit a very bright centre, and the number of these molecules increases with oxygen exposure, so it is reasonable to assume that this appearance corresponds to the $\text{Mn(IV)O}_2\text{TPP}$ complex. The lattice parameters of the ML are unchanged from those of MnClTPP and MnTPP, consistent with observations that the *meso*-aryl substituents are the main factors in supramolecular ordering [194].

The percentages shown on each image indicate the amount of Mn(III)TPP molecules that have been converted to the Mn(IV)O$_2$TPP state. The coverages correspond approximately to the XAS spectra shown in Figure 5.7, with the green spectrum showing ∼15% of the molecules oxidised, dark blue ∼40%, and light blue ∼80%.

After exposures of 90 minutes or more, approximately 80% of the molecules are converted to Mn(IV)O$_2$TPP, however at this point the extent of oxidation appears to saturate. The ∼20% unoxidised molecules are attributed to those molecules that lie on top of defects on the surface, or the very few that still have the Cl-ligand attached.

The MnO$_2$TPP molecule was also simulated using DFT. Identical constraints were applied as in the previous section. The relaxed structure is shown in Figure 5.12.

Figure 5.12a shows the side view of the molecule, showing the saddling of the molecule, similar to that of MnClTPP and MnTPP, although the view is rotated by 90° to Figure 5.10 in order to show the orientation of the O–O bond. Initially before relaxation, the bidentate peroxide ligand was positioned "diagonally" across the molecule, with the bond pointing along the line between two phenyl rings. It was first assumed that the O–O ligand would be repelled by the N atoms of the pyrrole rings, however when it was allowed to relax, the O–O bond rotated to lie along the convex slope of the saddle. Several starting positions were attempted, however the O–O bond consistently aligned itself parallel to the Mn–N bonds of the porphyrin, although the alignment along the convex slope (not shown) gave a higher
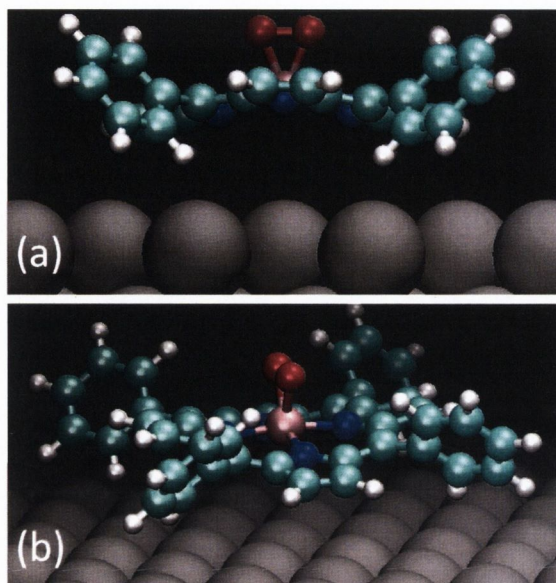
Figure 5.12: Relaxed model of the MnO_2TPP after oxidation. **(a)** Side view showing saddling in the macrocycle, and the O–O bond oriented along the convex slope of the saddle. **(b)** Isometric view illustrating the orientation of the O–O bond with respect to the phenyl rings.

total energy, and so it is assumed that the arrangement shown is the optimal structure.

It is unclear whether this relaxation is due to the O_2^{2-} anion avoiding the phenyl rings' steric hindrance [229], or due to an interaction between its electron lone-pairs and the π-electron system of the macrocycle, however hydrogen bonding between the anion and the phenyl rings can be ruled out, due to the former's preference to orient away from the latter, and the unaltered position of the phenyl rings after relaxation.

It was found that annealing the MnO_2TPP monolayer up to 445 K caused the desorption of the peroxide bound to the molecules without disturbing the structure of the monolayer, and STM images of Mn(III)TPP identical to those presented in the previous section were obtained (not shown).

In order to measure the activation energy for the desorption of O_2 from the molecules, XPS was performed while the monolayer was annealed, similar to the case of the Cl-ligand desorption. The O 1s spectra are presented in Figure 5.13a, with the temperature at which each spectrum was recorded shown at the right side. The same heating rate as for Cl-desorption of 0.15 K/sec was used.
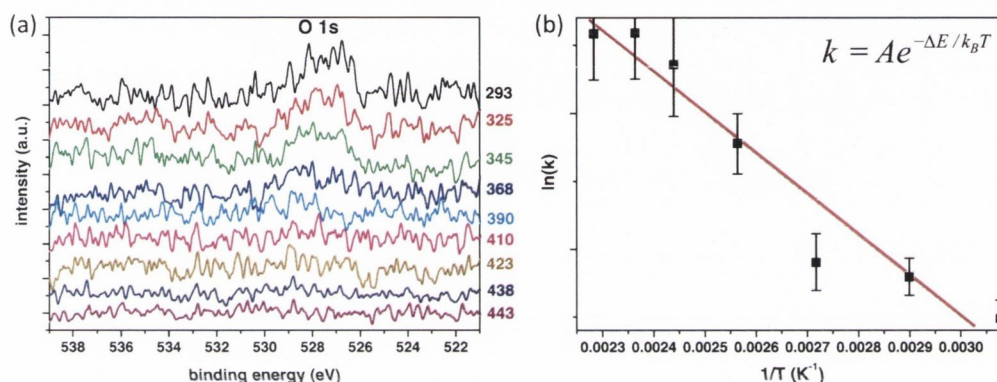
Figure 5.13: **(a)** O 1s XPS taken during the anneal of the Mn(IV)O_2TPP ML (temperature in K shown on right hand side). The O 1s peak diminishes until it completely disappears at 443 K. **(b)** Arrhenius plot of the logarithm of the O peak intensity vs the reciprocal of the temperature, giving an activation energy for the desorption of O_2 to be $\Delta E_{O_2} = 0.26 \pm 0.03$ eV. Again, the rate k was determined as the difference in area between two successive spectra.

The XPS data was treated similarly to the previous section describing the Cl desorption, and Figure 5.13b shows the Arrhenius plot for oxygen desorption.

In this case, the activation energy for the desorption of O_2 was found to be $\Delta E_{O_2} = 0.26 \pm 0.03$ eV. This value is lower than that for Cl desorption, indicating a weaker binding for the peroxide ligand than for the Cl ligand.

Interestingly it was noted that it was not possible to directly substitute O_2 for Cl at room temperature by exposing the MnClTPP monolayer to O_2

gas. This follows intuitively from the fact that the Cl ligand is more strongly bound to the Mn ion than the peroxide ligand, and so it is not energetically favourable for O_2 to displace the Cl ligand.

5.5   Conclusions

In summary, STM, XAS, core-level XPS and DFT were used to study the self-assembly and the central ligand transformation of the surface-supported monolayer of (5,10,15,20-tetraphenylporphyrinato)Mn(III)Cl (MnClTPP).

When deposited onto the Ag(111) surface, MnClTPP molecules self-assemble into large well-ordered molecular domains. Each molecule adopts a saddle conformation with the axial Cl-ligand pointing out of the plane of the molecule. One phenyl ring of each molecule is rotated slightly closer to the perpendicular, giving rise to a $\sqrt{2} \times \sqrt{2}R45°$ molecular Bravais unit cell.

Annealing the Mn(III)ClTPP layer up to 510 K causes the chlorine ligand to desorb from the porphyrin while leaving the supramolecular order unaffected. The Mn(III)TPP is stabilised by the Ag(111) surface acting as a fifth ligand for the metal centre.

When the Mn(III)TPP molecules are then exposed to molecular oxygen, the oxidation state of the central Mn changes from Mn(III) to Mn(IV), and O_2 is bound to the central Mn ion in peroxide form. Further annealing at 445 K reduces the Mn(IV)O_2TPP complex back to Mn(III)TPP/Ag(111). However, exposure of the MnClTPP layer to O_2 exhibits no direct substitution of the Cl ligand by O_2.

The activation energies for Cl and O_2 removal, derived from the XPS data, were found to be $0.35 \pm 0.02\,\text{eV}$ and $0.26 \pm 0.03\,\text{eV}$, respectively.

In conclusion, it has been shown that STM, together with spectroscopic surface science techniques such as XAS and XPS can shed light on the chemical make-up of single molecules and even oxidation states of individual atoms. When combined with DFT, structures observed by high-resolution STM can be explained with a high degree of confidence.

Chapter 6

Discussion & Conclusions

Although the primary technique used during the course of my studies was STM, it is clear from the preceding chapters that STM alone does not give a complete picture of the complexity of the organic molecule-substrate system. A combination of theory, modelling and DFT calculations, and ensemble-techniques such as LEED and spectroscopy complement the ultimate precision of STM.

In this work, the self-assembly and properties of three distinct organic molecules on a diverse range of surfaces, such as a conducting oxide (Chapter 3), a semiconductor (Chapter 4), and a noble metal (Chapters 4 and 5) have been demonstrated.

C_{60} fullerenes on the $WO_2/W(110)$ surface exhibit rich dynamic behaviours. It could instinctively be assumed that the time-resolution of STM would not be sufficient to observe the individual molecular switching seen, but with a careful choice of experimental parameters, single molecules gaining and losing charge have been observed. The rotational and kinetic transitions

159

observed also show the power of STM in measuring phase changes in the reduced-symmetry 2-dimensional monolayer. Phase transitions are vital for many biological and industrial reactions and the results obtained by STM reveal the nanoscale mechanisms driving them.

The molecule-substrate interface governs charge injection in molecular devices, so in order to study this, NiDPP has been used as a probe molecule to show the difference between its interaction with the noble surface of Ag(111) and the more-reactive Ag/Si(111)-$\sqrt{3}\times\sqrt{3}$ R30° surface. Large single-domain monolayers are observed on Ag(111), indicating that the substrate plays only a minor role in its self-assembly. In contrast, assembly on the Ag/Si(111)-$\sqrt{3}\times\sqrt{3}$ R30° surface results in the formation of randomly-oriented domains due to the higher strength of the molecule-substrate interaction.

In the design of a molecular device, control over the self-assembly of the molecular components will be key. If pristine long-range order is required it is likely that noble metals such as Ag(111) would represent suitable candidates for supporting substrates, however for more complex architecture it is likely that a template would be necessary. In this way, the Ag/Si(111)-$\sqrt{3}\times\sqrt{3}$ R30° surface with its strong molecular affinity directs the monolayer order by forcing the molecules to adopt one of three orientations, dictated by the substrate symmetry. Control over the balance between these two extremes by carefully choosing the adsorbate and substrate will be a key step in the development of molecular electronics and future devices.

The chemistry of industrially-relevant organic molecules such as the epoxidation-catalysing MnClTPP is of great importance to current and future technologies. By transforming the axial ligand attached to the metal centre

of the MnClTPP molecule, it is possible to control the oxidation state of the metal centre. The chemical and electronic structure information revealed by XPS and XAS and the structural details calculated using DFT allow complex STM images to be interpreted with high confidence.

Although recent studies [211, 228] make the case that liquid-STM is superior for the study of biologically relevant reactions, STM in UHV can provide more detail and allows for greater control over the condition of the molecules. Molecules in solution are inherently unstable due to interactions with dissolved substances; a property which is exploited in every biological and solution-phase chemical reaction, but which makes accurate characterisation of the molecular state difficult.

By performing a single reaction step at a time – cleaving the axial bond or adding a new axial ligand – the different stages of the reaction can be easily observed in UHV, as shown in this work. However, as with most aspects of surface science, there is no single technique which can provide all the information required, and so by combining detailed structural and electronic data measured in UHV with the dynamic behaviour measured *in situ*, a complete picture can be built up.

In summary, although organic molecules supported by surfaces have been widely studied for decades and show a lot of promise, there is still much unknown about their behaviour. In order to develop future devices, a clear picture of the kinetics, chemistry, charge injection and molecule-substrate interactions governing these interesting materials must first be built up through fundamental studies and quality surface science.

6.1   Future work

Through the course of this work, different molecules have been examined separately on several surfaces. This has been beneficial in understanding their individual behaviours, however the next step seems clear, to take this information and combine the molecules on the same surface.

Taking the dechlorinated Mn(III)TPP/Ag(111) system as the starting point, fullerenes can act as ligands in organometallic chemistry, and their size is comparable with that of the TPP molecule, so it is possible that the C_{60} may ligate to the undercoordinated Mn(III) centre. This would be an interesting result, as C_{60} has been shown to form a 1:1 mixture with octaethyl-porphyrins, but to completely replace the first layer of TPP on Ag(110) [230, 231].

Control over the orientation of a C_{60} molecule adsorbed on top of a CeTPP dyad has been shown using STM, with large changes in the conductance depending on the C_{60} orientation [232]. If the C_{60} was more strongly bound to the porphyrin however, as in the case of C_{60} ligating to MnTPP, it may not be possible to switch its orientation using the STM tip, but their relative orientation may determine charge injection through the system, and so it may be possible to distinguish between C_{60} orientations by their apparent height in STM even at room temperature.

On the Ag(111) surface, the number and size of substituent groups has been shown to determine the ordering of fullerene/porphyrin adlayers [8], and so it may be interesting to compare the small, linear NiDPP molecules' effect on the co-adsorption with the square MnClTPP molecules.

Another interesting avenue of exploration would be to test the effect of other gases on the Mn(III)TPP/Ag(111) system. If the central Mn(III) ion could be shown to bind selectively to other oxygen-containing gases such as CO, CO_2 or the oxides of nitrogen: combustion by-product NO; greenhouse gas N_2O; or pollutant and toxin NO_2; the molecule's sensitivity and selectivity as a gas sensor could be examined, which could have prospects for future applications.

Bibliography

[1] J. A. Elemans, R. van Hameren, R. J. Nolte, and A. E. Rowan. Molecular materials by self-assembly of porphyrins, phthalocyanines, and perylenes. *Advanced Materials*, 18(10):1251–1266, 2006.

[2] T. Yokoyama, S. Yokoyama, T. Kamikado, Y. Okuno, and S. Mashiko. Selective assembly on a surface of supramolecular aggregates with controlled size and shape. *Nature*, 413(6856):619–621, 2001.

[3] S. Stepanow, M. Lingenfelder, A. Dmitriev, H. Spillmann, E. Delvigne, N. Lin, X. Deng, C. Cai, J. V. Barth, and K. Kern. Steering molecular organization and host–guest interactions using two-dimensional nanoporous coordination systems. *Nature Materials*, 3(4):229–233, 2004.

[4] R. V. Hameren, P. Schön, A. M. V. Buul, J. Hoogboom, S. V. Lazarenko, J. W. Gerritsen, H. Engelkamp, P. C. Christianen, H. A. Heus, J. C. Maan, et al. Macroscopic hierarchical surface patterning of porphyrin trimers via self-assembly and dewetting. *Science*, 314(5804):1433–1436, 2006.

[5] H. Spillmann, A. Kiebele, M. Stöhr, T. A. Jung, D. Bonifazi, F. Cheng, and F. Diederich. A two-dimensional porphyrin-based porous network featuring communicating cavities for the templated complexation of fullerenes. *Advanced Materials*, 18(3):275–279, 2006.

[6] L. Grill, M. Dyer, L. Lafferentz, M. Persson, M. V. Peters, and S. Hecht. Nano-architectures by covalent assembly of molecular building blocks. *Nature Nanotechnology*, 2(11):687–691, 2007.

[7] F. Nishiyama, T. Yokoyama, T. Kamikado, S. Yokoyama, S. Mashiko, K. Sakaguchi, and K. Kikuchi. Interstitial accommodation of C_{60} in a surface-supported supramolecular network. *Advanced Materials*, 19(1):117–120, 2007.

[8] D. Bonifazi, A. Kiebele, M. Stöhr, F. Cheng, T. Jung, F. Diederich, and H. Spillmann. Supramolecular nanostructuring of silver surfaces via self-assembly of [60]fullerene and porphyrin modules. *Advanced Functional Materials*, 17(7):1051–1062, 2007.

[9] J. Beggan, S. Krasnikov, N. Sergeeva, M. Senge, and A. Cafolla. Self-assembly of Ni(II) porphine molecules on the Ag/Si(111)-$\sqrt{3} \times \sqrt{3}$ R30° surface studied by STM/STS and LEED. *Journal of Physics: Condensed Matter*, 20(1):015003, 2008.

[10] S. A. Krasnikov, J. P. Beggan, N. N. Sergeeva, M. O. Senge, and A. A. Cafolla. Ni(II) porphine nanolines grown on a Ag(111) surface at room temperature. *Nanotechnology*, 20(13):135301, 2009.

[11] S. A. Krasnikov, N. N. Sergeeva, Y. N. Sergeeva, M. O. Senge, and
A. A. Cafolla. Self-assembled rows of Ni porphyrin dimers on the Ag
(111) surface. *Physical Chemistry Chemical Physics*, 12(25):6666–6671,
2010.

[12] S. Haq, F. Hanke, M. S. Dyer, M. Persson, P. Iavicoli, D. B. Ama-
bilino, and R. Raval. Clean coupling of unfunctionalized porphyrins at
surfaces to give highly oriented organometallic oligomers. *Journal of
the American Chemical Society*, 133(31):12031–12039, 2011.

[13] S. A. Krasnikov, C. M. Doyle, N. N. Sergeeva, A. B. Preobrajenski,
N. A. Vinogradov, Y. N. Sergeeva, A. A. Zakharov, M. O. Senge, and
A. A. Cafolla. Formation of extended covalently bonded Ni porphyrin
networks on the Au(111) surface. *Nano Research*, 4(4):376–384, 2011.

[14] C. Joachim, J. Gimzewski, and A. Aviram. Electronics using hybrid-
molecular and mono-molecular devices. *Nature*, 408(6812):541–548,
2000.

[15] S. J. van der Molen and P. Liljeroth. Charge transport through molec-
ular switches. *Journal of Physics: Condensed Matter*, 22(13):133001,
2010.

[16] K. Moth-Poulsen and T. Bjørnholm. Molecular electronics with single
molecules in solid-state devices. *Nature Nanotechnology*, 4(9):551–556,
2009.

[17] C. B. Winkelmann, N. Roch, W. Wernsdorfer, V. Bouchiat, and F. Balestro. Superconductivity in a single-C_{60} transistor. *Nature Physics*, 5(12):876–879, 2009.

[18] G. Schulze, K. J. Franke, and J. I. Pascual. Resonant heating and substrate-mediated cooling of a single C_{60} molecule in a tunnel junction. *New Journal of Physics*, 10(6):065005, 2008.

[19] M. Novak, A. Ebel, T. Meyer-Friedrichsen, A. Jedaa, B. F. Vieweg, G. Yang, K. Voitchovsky, F. Stellacci, E. Spiecker, A. Hirsch, et al. Low-voltage p-and n-type organic self-assembled monolayer field effect transistors. *Nano Letters*, 11(1):156–159, 2010.

[20] H. Park, J. L. Park, K. L. Andrew, E. H. Anderson, A. P. Alivisatos, and P. L. McEuen. Nanomechanical oscillations in a single-C_{60} transistor. *Nature*, 407:57–60, 2000.

[21] L. J. A. Koster, V. D. Mihailetchi, and P. W. M. Blom. Ultimate efficiency of polymer/fullerene bulk heterojunction solar cells. *Applied Physics Letters*, 88(9):093511, 2006.

[22] M. Nakaya, S. Tsukamoto, Y. Kuwahara, M. Aono, and T. Nakayama. Molecular scale control of unbound and bound C_{60} for topochemical ultradense data storage in an ultrathin C_{60} film. *Advanced Materials*, 22(14):1622–1625, 2010.

[23] R. E. Smalley, H. Kroto, and J. Heath. C_{60}: Buckminsterfullerene. *Nature*, 318(6042):162–163, 1985.

[24] X. Zhang, L. Tang, and Q. Guo. Low-temperature growth of C_{60} mono-layers on Au(111): island orientation control with site-selective nucle-ation. *The Journal of Physical Chemistry C*, 114(14):6433–6439, 2010.

[25] J. A. Gardener, G. A. D. Briggs, and M. R. Castell. Scanning tunneling microscopy studies of C_{60} monolayers on Au(111). *Physical Review B*, 80(23):235434, December 2009.

[26] B. Diaconescu, T. Yang, S. Berber, M. Jazdzyk, G. P. Miller, D. Tománek, and K. Pohl. Molecular self-assembly of functionalized fullerenes on a metal surface. *Physical Review Letters*, 102(5):056102, 2009.

[27] H. Li, K. Franke, J. Pascual, L. Bruch, and R. Diehl. Origin of Moiré structures in C_{60} on Pb(111) and their effect on molecular energy levels. *Physical Review B*, 80(8):085415, 2009.

[28] X. Zhang, W. He, A. Zhao, H. Li, L. Chen, W. W. Pai, J. Hou, M. Loy, J. Yang, and X. Xiao. Geometric and electronic structure of a C_{60} monolayer on Ag(100). *Physical Review B*, 75(23):235444, 2007.

[29] C. Rogero, J. I. Pascual, J. Gómez-Herrero, and A. M. Baró. Resolution of site-specific bonding properties of C_{60} adsorbed on Au(111). *Journal Chem. Phys.*, 116:832–836, January 2002.

[30] M. Grobis, X. Lu, and M. F. Crommie. Local electronic proper-ties of a molecular monolayer: C_{60} on Ag(001). *Physical Review B*, 66(16):161408, October 2002.

[31] G. Schull, N. Néel, M. Becker, J. Kröger, and R. Berndt. Spatially resolved conductance of oriented C_{60}. *New Journal of Physics*, 10(6):065012, 2008.

[32] G. Schull and R. Berndt. Orientationally ordered (7×7) superstructure of C_{60} on Au(111). *Physical Review Letters*, 99(22):226105, 2007.

[33] W. W. Pai, C.-L. Hsu, M. Lin, K. Lin, and T. Tang. Structural relaxation of adlayers in the presence of adsorbate-induced reconstruction: C_{60}/Cu(111). *Physical Review B*, 69(12):125405, 2004.

[34] M. Abel, A. Dmitriev, R. Fasel, N. Lin, J. Barth, and K. Kern. Scanning tunneling microscopy and X-ray photoelectron diffraction investigation of C_{60} films on Cu(100). *Physical Review B*, 67(24):245407, 2003.

[35] C.-L. Hsu and W. W. Pai. Aperiodic incommensurate phase of a C_{60} monolayer on Ag(100). *Physical Review B*, 68(24):245414, December 2003.

[36] J. Weckesser, C. Cepek, R. Fasel, J. V. Barth, F. Baumberger, T. Greber, and K. Kern. Binding and ordering of C_{60} on Pd(110): Investigations at the local and mesoscopic scale. *The Journal of Chemical Physics*, 115(19):9001–9009, 2001.

[37] P. Murray, M. Pedersen, E. Lægsgaard, I. Stensgaard, and F. Besenbacher. Growth of C_{60} on Cu(110) and Ni(110) surfaces: C_{60}-induced interfacial roughening. *Physical Review B*, 55(15):9360, 1997.

[38] Y. Li, J. Patrin, M. Chander, J. Weaver, L. Chibante, and R. Smalley. Ordered overlayers of C_{60} on GaAs(110) studied with scanning tunneling microscopy. *Science*, 252(5005):547–548, 1991.

[39] Y. Li, M. Chander, J. Patrin, J. Weaver, L. Chibante, and R. Smalley. Order and disorder in C_{60} and $K_x C_{60}$ multilayers: Direct imaging with scanning tunneling microscopy. *Science*, 253(5018):429–433, 1991.

[40] J. Hou, J. Yang, H. Wang, Q. Li, C. Zeng, H. Lin, W. Bing, D. Chen, and Q. Zhu. Identifying molecular orientation of individual C_{60} on a Si(111)-(7×7) surface. *Physical Review Letters*, 83(15):3001, 1999.

[41] J. Pascual, J. Gómez-Herrero, C. Rogero, A. Baró, D. Sánchez-Portal, E. Artacho, P. Ordejón, and J. Soler. Seeing molecular orbitals. *Chemical Physics Letters*, 321(1):78–82, 2000.

[42] A. Dunn, E. Svensson, and C. Dekker. Scanning tunneling spectroscopy of C_{60} adsorbed on Si(100)-(2×1). *Surface Science*, 498(3):237–243, 2002.

[43] C. Lu, E. Zhu, Y. Liu, Z. Liu, Y. Lu, J. He, D. Yu, Y. Tian, and B. Xu. C_{60} on nanostructured Nb-doped $SrTiO_3$ (001) surfaces. *The Journal of Physical Chemistry C*, 114(8):3416–3421, 2010.

[44] F. Loske, R. Bechstein, J. Schütte, F. Ostendorf, M. Reichling, and A. Kühnle. Growth of ordered C_{60} islands on TiO_2(110). *Nanotechnology*, 20(6):065606, 2009.

[45] A. Carvalho and J. Ramalho. Molecular simulation of C_{60} adsorption onto a TiO_2 rutile (110) surface. *Applied Surface Science*, 256(17):5365–5369, 2010.

[46] S. A. Krasnikov, S. I. Bozhko, K. Radican, O. Lübben, B. E. Murphy, S.-R. Vadapoo, H.-C. Wu, M. Abid, V. N. Semenov, and I. V. Shvets. Self-assembly and ordering of C_{60} on the WO_2/W(110) surface. *Nano Research*, 4(2):194–203, 2011.

[47] S. I. Bozhko, S. A. Krasnikov, O. Lübben, B. E. Murphy, K. Radican, V. N. Semenov, H. C. Wu, B. Bulfin, and I. V. Shvets. Rotational transitions in a C_{60} monolayer on the WO_2/W(110) surface. *Physical Review B*, 84(19):195412, 2011.

[48] S. I. Bozhko, S. A. Krasnikov, O. Lübben, B. E. Murphy, K. Radican, V. N. Semenov, H.-C. Wu, E. A. Levchenko, A. N. Chaika, N. N. Sergeeva, et al. Correlation between charge-transfer and rotation of C_{60} on WO_2/W(110). *Nanoscale*, 5(8):3380–3386, 2013.

[49] J. S. Miller and A. J. Epstein. Organic and organometallic molecular magnetic materials–designer magnets. *Angewandte Chemie International Edition in English*, 33(4):385–415, 1994.

[50] B. Murphy, S. Krasnikov, A. Cafolla, N. Sergeeva, N. Vinogradov, J. Beggan, O. Lübben, M. Senge, and I. Shvets. Growth and ordering of Ni(II) diphenylporphyrin monolayers on Ag(111) and Ag/Si(111) studied by STM and LEED. *Journal of Physics: Condensed Matter*, 24(4):045005, 2012.

[51] L. Meitner. Über die Entstehung der β-Strahl-Spektren radioaktiver Substanzen. *Zeitschrift für Physik A Hadrons and Nuclei*, 9(1):131–144, 1922.

[52] P. Auger. Sur les rayons β secondaires produits dans un gaz par des rayons X. *Comptes Rendus de l'Académie des Sciences*, 177(3):169, 1923.

[53] C. Davisson and L. H. Germer. Diffraction of electrons by a crystal of nickel. *Physical Review*, 30(6):705, 1927.

[54] G. Binnig and H. Rohrer. Scanning tunneling microscopy – from birth to adolescence (Nobel Lecture). *Angewandte Chemie International Edition in English*, 26(7):606–614, 1987.

[55] C. Doyle. *An Investigation of the Structural and Electronic Properties of Covalently Bonded Molecular Networks on Metal Surfaces Formed Through Debromination Reactions*. PhD thesis, Dublin City University, 2013.

[56] I. Horcas, R. Fernandez, J. Gomez-Rodriguez, J. Colchero, J. Gómez-Herrero, and A. Baro. WSxM: a software for scanning probe microscopy and a tool for nanotechnology. *Review of Scientific Instruments*, 78:013705, 2007.

[57] M. Blank. Example XAS spectrum showing the three major data regions [http://en.wikipedia.org/wiki/File:XASFig.jpg], September 2013.

[58] E. Stern. Musings about the development of XAFS. *Journal of Synchrotron Radiation*, 8(2):49–54, 2001.

[59] A. Tenderholt. Diagram showing which transitions contribute to X-ray absorption edges [http://en.wikipedia.org/wiki/File:XASEdges.svg], September 2013.

[60] P. Hohenberg and W. Kohn. Inhomogeneous electron gas. *Physical Review*, 136(3B):B864, 1964.

[61] C. Huang and E. A. Carter. Nonlocal orbital-free kinetic energy density functional for semiconductors. *Physical Review B*, 81(4):045206, 2010.

[62] J. P. Perdew, K. Burke, and M. Ernzerhof. Generalized gradient approximation made simple. *Physical Review Letters*, 77(18):3865, 1996.

[63] S. Grimme. Density functional theory with London dispersion corrections. *Wiley Interdisciplinary Reviews: Computational Molecular Science*, 1(2):211–228, 2011.

[64] S. Grimme. Accurate description of van der Waals complexes by density functional theory including empirical corrections. *Journal of Computational Chemistry*, 25(12):1463–1473, 2004.

[65] U. Zimmerli, M. Parrinello, and P. Koumoutsakos. Dispersion corrections to density functionals for water aromatic interactions. *The Journal of Chemical Physics*, 120(6):2693–2699, 2004.

[66] S. Grimme.   Semiempirical hybrid density functional with pertur-
     bative second-order correlation.   *The Journal of Chemical Physics*,
     124(3):034108, 2006.

[67] A. Tkatchenko and M. Scheffler.   Accurate molecular van der Waals
     interactions from ground-state electron density and free-atom reference
     data. *Phys. Rev. Lett.*, 102:073005, Feb 2009.

[68] O. A. von Lilienfeld, I. Tavernelli, U. Rothlisberger, and D. Sebastiani.
     Optimization of effective atom centered potentials for London disper-
     sion forces in density functional theory. *Phys. Rev. Lett.*, 93:153004,
     Oct 2004.

[69] G. Román-Pérez and J. M. Soler. Efficient implementation of a van
     der Waals density functional: Application to double-wall carbon nan-
     otubes. *Phys. Rev. Lett.*, 103:096102, Aug 2009.

[70] G. Kresse and J. Furthmüller. Efficient iterative schemes for ab initio
     total-energy calculations using a plane-wave basis set. *Physical Review
     B*, 54(16):11169–11186, 1996.

[71] G. Kresse and J. Furthmüller. *VASP: the guide*, chapter 9.4 Partial
     occupancies, different methods. Technische Universität Wien, 1999.

[72] M. Methfessel and A. T. Paxton. High-precision sampling for Brillouin-
     zone integration in metals. *Physical Review B*, 40(6):3616–3621, August
     1989.

[73] A. N. Chaika, V. N. Semenov, V. G. Glebovskiy, and S. I. Bozhko. Scanning tunneling microscopy with single crystalline W(001) tips: High resolution studies of Si(557)5 × 5 surface. *Appl. Phys. Lett.*, 95(17):173107, 2009.

[74] A. Chaika, S. Nazin, V. Semenov, S. Bozhko, O. Lübben, S. Krasnikov, K. Radican, and I. Shvets. Selecting the tip electron orbital for scanning tunneling microscopy imaging with sub-Å lateral resolution. *Europhysics Letters*, 92(4):46003, 2010.

[75] D. M. Ceperley and B. J. Alder. Ground state of the electron gas by a stochastic method. *Phys. Rev. Lett.*, 45(7):566–569, 1980.

[76] J. V. Barth. Molecular architectonic on metal surfaces. *Annu. Rev. Phys. Chem.*, 58:375–407, 2007.

[77] J. V. Barth, G. Costantini, and K. Kern. Engineering atomic and molecular nanostructures at surfaces. *Nature*, 437(7059):671–679, 2005.

[78] S. M. Barlow and R. Raval. Complex organic molecules at metal surfaces: Bonding, organisation and chirality. *Surface Science Reports*, 50(68):201–341, 2003.

[79] F. Rosei, M. Schunack, Y. Naitoh, P. Jiang, A. Gourdon, E. Laegsgaard, I. Stensgaard, C. Joachim, and F. Besenbacher. Properties of large organic molecules on metal surfaces. *Progress in Surface Science*, 71(5):95–146, 2003.

[80] J. Schnadt, W. Xu, R. T. Vang, J. Knudsen, Z. Li, E. Lægsgaard, and F. Besenbacher. Interplay of adsorbate-adsorbate and adsorbate-substrate interactions in self-assembled molecular surface nanostructures. *Nano Research*, 3(7):459–471, 2010.

[81] H. Liang, Y. He, Y. Ye, X. Xu, F. Cheng, W. Sun, X. Shao, Y. Wang, J. Li, and K. Wu. Two-dimensional molecular porous networks constructed by surface assembling. *Coordination Chemistry Reviews*, 253(23):2959–2979, 2009.

[82] S. A. Krasnikov, C. J. Hanson, D. F. Brougham, and A. A. Cafolla. Dimer ordering of CuTtertBuPc molecules on the Ag/Si(111)-$\sqrt{3} \times \sqrt{3}$ R30° surface: A scanning tunnelling microscopy/spectroscopy study. *Journal of physics. Condensed matter*, 19(44), 2007.

[83] D. Fichou. Structural order in conjugated oligothiophenes and its implications on opto-electronic devices. *Journal of Materials Chemistry*, 10(3):571–588, 2000.

[84] D. Bonifazi, O. Enger, and F. Diederich. Supramolecular C_{60} fullerene chemistry on surfaces. *Chem. Soc. Rev.*, 36:390–414, 2007.

[85] E. Xenogiannopoulou, M. Medved, K. Iliopoulos, S. Couris, M. G. Papadopoulos, D. Bonifazi, C. Sooambar, A. Mateo-Alonso, and M. Prato. Nonlinear optical properties of ferrocene-and porphyrin–[60]fullerene dyads. *Chem. Phys. Chem.*, 8(7):1056–1064, 2007.

[86] A. Hebard, M. Rosseinky, R. Haddon, D. Murphy, S. Glarum, T. Palstra, A. Ramirez, and A. Karton. Potassium-doped C_{60}. *Nature*, 350:600–601, 1991.

[87] K. Tanigaki, T. Ebbesen, S. Saito, J. Mizuki, J. Tsai, Y. Kubo, and S. Kuroshima. Superconductivity at 33K in $Cs_xRb_yC_{60}$. *Nature*, 352(6332):222–223, 1991.

[88] R. C. Hiorns, E. Cloutet, E. Ibarboure, L. Vignau, N. Lemaitre, S. Guillerez, C. Absalon, and H. Cramail. Main-chain fullerene polymers for photovoltaic devices. *Macromolecules*, 42(10):3549–3558, 2009.

[89] M. Grobis, R. Yamachika, A. Wachowiak, X. Lu, and M. F. Crommie. Phase separation and charge transfer in a K-doped C_{60} monolayer on Ag(001). *Physical Review B*, 80(7):073410, August 2009.

[90] E. Fortunato, P. Barquinha, and R. Martins. Oxide semiconductor thin-film transistors: A review of recent advances. *Advanced Materials*, 24(22):2945–2986, 2012.

[91] J. Meyer, S. Hamwi, M. Kröger, W. Kowalsky, T. Riedl, and A. Kahn. Transition metal oxides for organic electronics: Energetics, device physics and applications. *Advanced Materials*, 24(40):5408–5427, 2012.

[92] M. T. Greiner and Z.-H. Lu. Thin-film metal oxides in organic semiconductor devices: their electronic structures, work functions and interfaces. *NPG Asia Materials*, 5(7):e55, 2013.

[93] H. Frenzel, A. Lajn, and M. Grundmann. One decade of fully transparent oxide thin-film transistors: fabrication, performance and stability. *physica status solidi (RRL)-Rapid Research Letters*, 7(9):605–615, 2013.

[94] K. Radican, S. I. Bozhko, S.-R. Vadapoo, S. Ulucan, H.-C. Wu, A. McCoy, and I. V. Shvets. Oxidation of W(110) studied by LEED and STM. *Surface Science*, 604(19-20):1548–1551, 2010.

[95] S. Krasnikov, S. Murphy, N. Berdunov, A. McCoy, K. Radican, and I. Shvets. Self-limited growth of triangular PtO_2 nanoclusters on the Pt(111) surface. *Nanotechnology*, 21(33):335301, 2010.

[96] K. Radican, N. Berdunov, and I. Shvets. Studies of the periodic faceting of epitaxial molybdenum oxide grown on Mo(110). *Physical Review B*, 77(8):085417, 2008.

[97] K. Radican, N. Berdunov, G. Manai, and I. V. Shvets. Epitaxial molybdenum oxide grown on Mo(110) : LEED, STM, and density functional theory calculations. *Physical Review B*, 75(15):155434, April 2007.

[98] L.-L. Wang and H.-P. Cheng. Rotation, translation, charge transfer, and electronic structure of C_{60} on cu(111) surface. *Physical Review B*, 69(4):045404, 2004.

[99] T. Hashizume, K. Motai, X. Wang, H. Shinohara, Y. Saito, Y. Maruyama, K. Ohno, Y. Kawazoe, Y. Nishina, H. Pickering, et al. Intramolecular structures of C_{60} molecules adsorbed on the Cu (111)-(1× 1) surface. *Physical review letters*, 71(18):2959, 1993.

[100] A. Fartash. Interfacially ordered C_{60} films on Cu(111) substrates. *Journal of applied physics*, 79(2):742–747, 1996.

[101] T. Sakurai, X. Wang, T. Hashizume, V. Yurov, H. Shinohara, and H. Pickering. Adsorption of fullerenes on Cu(111) and Ag(111) surfaces. *Applied surface science*, 87:405–413, 1995.

[102] T. Sakurai, X.-D. Wang, Q. Xue, Y. Hasegawa, T. Hashizume, and H. Shinohara. Scanning tunneling microscopy study of fullerenes. *Progress in surface science*, 51(4):263–408, 1996.

[103] K.-D. Tsuei and P. Johnson. Charge transfer and a new image state of C_{60} on Cu(111) surface studied by inverse photoemission. *Solid state communications*, 101(5):337–341, 1997.

[104] K.-D. Tsuei, J.-Y. Yuh, C.-T. Tzeng, R.-Y. Chu, S.-C. Chung, and K.-L. Tsang. Photoemission and photoabsorption study of C_{60} adsorption on Cu (111) surfaces. *Physical Review B*, 56(23):15412, 1997.

[105] A. Hebard, R. Ruel, and C. Eom. Charge transfer and surface scattering at Cu-C_{60} planar interfaces. *Physical Review B*, 54(19):14052, 1996.

[106] E. I. Altman and R. J. Colton. Determination of the orientation of C_{60} adsorbed on Au(111) and Ag(111). *Physical Review B*, 48(24):18244–18249, December 1993.

[107] E. I. Altman and R. J. Colton. The interaction of C_{60} with noble metal surfaces. *Surface Science*, 295(1):13–33, 1993.

[108] K. Pussi, H. Li, H. Shin, L. S. Loli, A. Shukla, J. Ledieu, V. Fournée, L. Wang, S. Su, K. Marino, et al. Elucidating the dynamical equilibrium of C_{60} molecules on Ag (111). *Physical Review B*, 86(20):205406, 2012.

[109] W. W. Pai, H. Jeng, C.-M. Cheng, C.-H. Lin, X. Xiao, A. Zhao, X. Zhang, G. Xu, X. Shi, M. Van Hove, et al. Optimal electron doping of a C_{60} monolayer on Cu (111) via interface reconstruction. *Physical review letters*, 104(3):036103, 2010.

[110] X.-Q. Shi, M. A. Van Hove, and R.-Q. Zhang. Adsorbate-induced reconstruction by C_{60} on close-packed metal surfaces: Mechanism for different types of reconstruction. *Physical Review B*, 85(7):075421, 2012.

[111] C. Cepek, A. Goldoni, and S. Modesti. Chemisorption and fragmentation of C_{60} on Pt (111) and Ni (110). *Physical Review B*, 53(11):7466, 1996.

[112] N. Swami, H. He, and B. E. Koel. Polymerization and decomposition of C_{60} on Pt(111) surfaces. *Physical Review B*, 59(12):8283, 1999.

[113] T. Orzali, D. Forrer, M. Sambi, A. Vittadini, M. Casarin, and E. Tondello. Temperature-dependent self-assemblies of C_{60} on (1×2)-Pt(110): A STM/DFT investigation. *The Journal of Physical Chemistry C*, 112(2):378–390, 2008.

[114] M. Hunt, S. Modesti, P. Rudolf, and R. Palmer. Charge transfer and structure in C_{60} adsorption on metal surfaces. *Physical Review B*, 51(15):10039, 1995.

[115] K. Sakamoto, D. Kondo, Y. Ushimi, M. Harada, A. Kimura, A. Kak-izaki, and S. Suto. Temperature dependence of the electronic structure of C_{60} films adsorbed on Si(001)-(2× 1) and Si(111)-(7× 7) surfaces. *Physical Review B*, 60(4):2579, 1999.

[116] D. Chen and D. Sarid. An STM study of C_{60} adsorption on Si(100)-(2× 1) surfaces: from physisorption to chemisorption. *Surface science*, 329(3):206–218, 1995.

[117] X. Yao, T. G. Ruskell, R. K. Workman, D. Sarid, and D. Chen. In-tramolecular features of individual C_{60} molecules on Si(100) observed by STM. *Surface science*, 367(3):L85–L90, 1996.

[118] E. Giudice, E. Magnano, S. Rusponi, C. Boragno, and U. Valbusa. Morphology of C_{60} thin films grown on Ag(001). *Surface Science*, 405(2-3):L561–L565, 1998.

[119] S. Tsukamoto, T. Nakayama, and M. Aono. Stable molecular orienta-tions of a C_{60} dimer in a photoinduced dimer row. *Carbon*, 45(6):1261–1266, 2007.

[120] M. Nakaya, Y. Kuwahara, M. Aono, and T. Nakayama. Reversibility-controlled single molecular level chemical reaction in a C_{60} monolayer via ionization induced by scanning transmission microscopy. *Small*, 4(5):538–541, 2008.

[121] J. Zhao, K. Tatani, and Y. Ozaki. Mechanism of thermal phase transi-tion of a ferroelectric liquid crystal with monotropic transition temper-

ature studied by infrared spectroscopy combined with principal component analysis and sample–sample two-dimensional correlation spectroscopy. *Appl. Spectrosc.*, 59(5):620–629, 2005.

[122] H. W. J. Blöte, W. Guo, and H. J. Hilhorst. Phase transition in a two-dimensional heisenberg model. *Phys. Rev. Lett.*, 88(4):047203, 2002.

[123] O. Lübben, L. Dudy, A. Krapf, C. Janowitz, and R. Manzke. Structural behavior of $Pb_yBi_{1.95-y}Sr_{1.49}La_{0.4}Cu_{1.15}O_{6+\delta}$ for $0 < y < 0.53$. *Physical Review B*, 81(17):174112, 2010.

[124] F. Delogu, G. Manai, and I. Shvets. The reversibility of phase transitions in Ti/Co core/shell nanometre-sized particles. *Nanotechnology*, 20(1):015702, 2009.

[125] S. Sarkar and S. C. Peter. Structural phase transitions in a new compound Eu_2AgGe_3. *Inorganic chemistry*, 52(17):9741–9748, 2013.

[126] H. Lüth. *Solid Surfaces, Interfaces and Thin Films*. Springer, 2001.

[127] P. V. L. Lyuksyutov I.F., Naumovets A.G. *Two-Dimensional Crystals*. Naukova Dumka, 1988.

[128] P. H. E. M. P. Papon, J. Leblond. *The Physics of Phase Transitions: Concepts and Applications*. Springer, 2006.

[129] J. M. Kosterlitz and D. J. Thouless. Ordering, metastability and phase transitions in two-dimensional systems. *J.Phys.C: Solid State Phys.*, 6:1181–1203, 1973.

[130] R. D. Johnson, C. S. Yannoni, H. C. Dorn, J. R. Salem, and D. S. Bethune. C_{60} rotation in the solid state: Dynamics of a faceted spherical top. *Science*, 255(5049):1235–1238, 1992.

[131] W. I. F. David, R. M. Ibberson, J. C. Matthewman, K. Prassides, T. J. S. Dennis, J. P. Hare, H. W. Kroto, R. Taylor, and D. R. M. Walton. Crystal structure and bonding of ordered C_{60}. *Nature*, 353(6340):147–149, 1991.

[132] W. I. F. David, R. M. Ibberson, T. J. S. Dennis, J. P. Hare, and K. Prassides. Structural phase transitions in the fullerene C_{60}. *Europhysics Letters*, 18(3):219, 1992.

[133] R. Moret. Structures, phase transitions and orientational properties of the C_{60} monomer and polymers. *Acta Crystallographica Section A*, 61(1):62–76, 2005.

[134] S. L. Chaplot, L. Pintschovius, M. Haluska, and H. Kuzmany. Orientational disorder in C_{60} below T_s: A diffuse-neutron-scattering study. *Physical Review B*, 51(23):17028–17034, 1995.

[135] W. Schranz, A. Fuith, P. Dolinar, H. Warhanek, M. Haluska, and H. Kuzmany. Low frequency elastic properties of the structural and freezing transitions in single-crystal C_{60}. *Phys. Rev. Lett.*, 71(10):1561–1564, 1993.

[136] F. Gugenberger, R. Heid, C. Meingast, P. Adelmann, M. Braun, H. Wühl, M. Haluska, and H. Kuzmany. Glass transition in single-

crystal C_{60} studied by high-resolution dilatometry. *Phys. Rev. Lett.*, 69(26):3774–3777, 1992.

[137] F. Yan, Y. N. Wang, and J. S. Liu. The non-exponential relaxation of the C_{60} crystal around glass transition temperature. *Europhysics Letters*, 48(6):662, 1999.

[138] J. P. Lu, X.-P. Li, and R. M. Martin. Ground state and phase transitions in solid C_{60}. *Phys. Rev. Lett.*, 68(10):1551–1554, 1992.

[139] T. Matsuo, H. Suga, W. I. F. David, R. M. Ibberson, P. Bernier, A. Zahab, C. Fabre, A. Rassat, and A. Dworkin. The heat capacity of solid C_{60}. *Solid State Communications*, 83(9):711–715, 1992.

[140] Y. Yoneda, K. Sakaue, and T. Terauchi. Phase transitions of C_{60} thin films grown by molecular beam epitaxy. *Journal of Physics: Condensed Matter*, 9(14):2851, 1997.

[141] D. Lamoen and K. H. Michel. Crystal field, orientational order, and lattice contraction in solid C_{60}. *J. Chem. Phys.*, 101(2):1435–1443, 1994.

[142] D. Passerone and E. Tosatti. Surface rotational disordering in crystalline C_{60}. *Surf. Rev. Lett.*, 4(5):859–861, 1997.

[143] C. Laforge, D. Passerone, A. B. Harris, P. Lambin, and E. Tosatti. Two-stage rotational disordering of a molecular crystal surface: C_{60}. *Phys. Rev. Lett.*, 87(8):085503, 2001.

[144] X. Lu, M. Grobis, K. H. Khoo, S. G. Louie, and M. F. Crommie. Charge transfer and screening in individual C_{60} molecules on metal substrates: A scanning tunneling spectroscopy and theoretical study. *Physical Review B*, 70(11):115418, 2004.

[145] J. A. Larsson, S. D. Elliott, J. C. Greer, J. Repp, G. Meyer, and R. Allenspach. Orientation of individual C_{60} molecules adsorbed on Cu(111): Low-temperature scanning tunneling microscopy and density functional calculations. *Physical Review B*, 77(11):115434, 2008.

[146] S. B. Trickey, F. Müller-Plathe, G. H. F. Diercksen, and J. C. Boettger. Interplanar binding and lattice relaxation in a graphite dilayer. *Physical Review B*, 45:4460–4468, 1992.

[147] S. Saito and A. Oshiyama. Cohesive mechanism and energy bands of solid C_{60}. *Phys. Rev. Lett.*, 66:2637–2640, 1991.

[148] S. Okada, S. Saito, and A. Oshiyama. Energetics and electronic structures of encapsulated C_{60} in a carbon nanotube. *Phys. Rev. Lett.*, 86:3835–3838, 2001.

[149] J.-C. Charlier, X. Gonze, and J.-P. Michenaud. Graphite interplanar bonding: Electronic delocalization and van der waals interaction. *Europhysics Letters*, 28(6):403, 1994.

[150] N. Troullier and J. L. Martins. Structural and electronic properties of C_{60}. *Physical Review B*, 46:1754–1765, 1992.

[151] J.-C. Charlier, X. Gonze, and J.-P. Michenaud. First-principles study of carbon nanotube solid-state packings. *Europhysics Letters*, 29(1):43, 1995.

[152] L. A. Girifalco and M. Hodak. Van der waals binding energies in graphitic structures. *Physical Review B*, 65:125404, 2002.

[153] M. Fujimoto. *The Physics of Structural Phase Transitions*, page 39. Springer, 2005.

[154] S. Savin, A. B. Harris, and T. Yildirim. Towards a microscopic approach to the intermolecular interaction in solid C_{60}. *Physical Review B*, 55(21):14182–14199, 1997.

[155] F. Tournus, J.-C. Charlier, and P. Mèlinon. Mutual orientation of two C_{60} molecules: An ab initio study. *J Chem Phys.*, 122(9):094315, 2005.

[156] A. Goldoni, C. Cepek, R. Larciprete, L. Sangaletti, S. Pagliara, G. Paolucci, and M. Sancrotti. Core level photoemission evidence of frustrated surface molecules: A germ of disorder at the (111) surface of C_{60} before the order-disorder surface phase transition. *Phys. Rev. Lett.*, 88(19):196102, 2002.

[157] A. Glebov, V. Senz, J. P. Toennies, and G. Gensterblum. Rotational-disordering phase transition of $C_{60}(111)$ epitaxial films grown on GeS(001). *Journal of Applied Physics*, 82(5):2329–2333, 1997.

[158] M. D. Ediger, C. A. Angell, and S. R. Nagel. Supercooled liquids and glasses. *The Journal of Physical Chemistry*, 100(31):13200–13212, 1996.

[159] F. H. Stillinger. A topographic view of supercooled liquids and glass formation. *Science*, 267(5206):1935–1939, 1995.

[160] R. G. Palmer, D. L. Stein, E. Abrahams, and P. W. Anderson. Models of hierarchically constrained dynamics for glassy relaxation. *Phys. Rev. Lett.*, 53(10):958–961, 1984.

[161] P. J. Moriarty. Fullerene adsorption on semiconductor surfaces. *Surface Science Reports*, 65(7):175–227, 2010.

[162] J. Repp, G. Meyer, F. E. Olsson, and M. Persson. Controlling the charge state of individual gold adatoms. *Science*, 305(5683):493–495, 2004.

[163] I. Swart, T. Sonnleitner, and J. Repp. Charge state control of molecules reveals modification of the tunneling barrier with intramolecular contrast. *Nano Letters*, 11(4):1580–1584, 2011.

[164] V. Weisskopf and E. Wigner. Berechnung der natürlichen Linienbreite auf Grund der Diracschen Lichttheorie. *Zeitschrift für Physik*, 63:54, 1930.

[165] C. J. Chen. *Introduction to scanning tunneling microscopy*, volume 227. Oxford University Press New York, 1993.

[166] A. N. Chaika, S. S. Nazin, V. N. Semenov, N. N. Orlova, S. I. Bozhko, O. Lübben, S. A. Krasnikov, K. Radican, and I. V. Shvets. High resolution STM imaging with oriented single crystalline tips. *Applied Surface Science*, 267(0):219–223, 2013. 11th International Conference on Atomically Controlled Surfaces, Interfaces and Nanostructures.

[167] R. Yamachika, M. Grobis, A. Wachowiak, and M. Crommie. Controlled atomic doping of a single C_{60} molecule. *Science*, 304(5668):281–284, 2004.

[168] R. Flores-Moreno. Symmetry conservation in Fukui functions. *Journal of Chemical Theory and Computation*, 6(1):48–54, 2009.

[169] C. Brueckner, J. J. Posakony, C. K. Johnson, R. W. Boyle, B. R. James, and D. Dolphin. Novel and improved syntheses of 5, 15-diphenylporphyrin and its dipyrrolic precursors. *Journal of Porphyrins and Phthalocyanines*, 2(6):455–465, 1998.

[170] M. O. Senge, M. Fazekas, E. G. Notaras, W. J. Blau, M. Zawadzka, O. B. Locos, and E. M. N. Mhuircheartaigh. Nonlinear optical properties of porphyrins. *Advanced Materials*, 19(19):2737–2774, 2007.

[171] V. Lin, S. G. DiMagno, and M. J. Therien. Highly conjugated, acetylenyl bridged porphyrins: New models for light-harvesting antenna systems. *Science*, 264(5162):1105–1111, 1994.

[172] J. Chen, M. Reed, A. Rawlett, and J. Tour. Large on-off ratios and negative differential resistance in a molecular electronic device. *Science*, 286(5444):1550–1552, 1999.

[173] A. Tsuda and A. Osuka. Fully conjugated porphyrin tapes with electronic absorption bands that reach into infrared. *Science*, 293(5527):79–82, 2001.

[174] O. Ikkala and G. ten Brinke. Functional materials based on self-assembly of polymeric supramolecules. *Science*, 295(5564):2407–2409, 2002.

[175] N. Papageorgiou, E. Salomon, T. Angot, J.-M. Layet, L. Giovanelli, and G. L. Lay. Physics of ultra-thin phthalocyanine films on semiconductors. *Progress in surface science*, 77(5):139–170, 2004.

[176] A. M. Sena, V. Brázdová, and D. R. Bowler. Density functional theory study of the iron-based porphyrin haem (b) on the Si(111):H surface. *Physical Review B*, 79(24):245404, 2009.

[177] M. Wagner, P. Puschnig, S. Berkebile, F. P. Netzer, and M. G. Ramsey. Alternating chirality in the monolayer H_2TPP on $Cu(110)$–$(2 \times 1)O$. *Physical Chemistry Chemical Physics*, 15(13):4691–4698, 2013.

[178] M. Lackinger, M. S. Janson, and W. Ho. Localized interaction of single porphyrin molecules with oxygen vacancies on $TiO_2(110)$. *The Journal of chemical physics*, 137(23):234707, 2012.

[179] P. A. Sloan and R. Palmer. Two-electron dissociation of single molecules by atomic manipulation at room temperature. *Nature*, 434(7031):367–371, 2005.

[180] M. El Garah, Y. Makoudi, F. Palmino, E. Duverger, P. Sonnet, L. Chaput, A. Gourdon, and F. Cherioux. STM and DFT investigations of isolated porphyrin on a silicon-based semiconductor at room temperature. *ChemPhysChem*, 10(18):3190–3193, 2009.

[181] Y. Suzuki, M. Hietschold, and D. R. Zahn. Growth of copper phthalocyanine on hydrogen passivated vicinal silicon (111) surfaces. *Applied Surface Science*, 252(15):5449–5452, 2006.

[182] T.-C. Shen, C. Wang, G. Abeln, J. Tucker, J. Lyding, P. Avouris, and R. Walkup. Atomic-scale desorption through electronic and vibrational excitation mechanisms. *Science*, 268(5217):1590–1592, 1995.

[183] M. Hersam, N. Guisinger, and J. Lyding. Silicon-based molecular nanotechnology. *Nanotechnology*, 11(2):70, 2000.

[184] Y. Bai, F. Buchner, M. T. Wendahl, I. Kellner, A. Bayer, H.-P. Steinrück, H. Marbach, and J. M. Gottfried. Direct metalation of a phthalocyanine monolayer on Ag(111) with coadsorbed iron atoms. *The Journal of Physical Chemistry C*, 112(15):6087–6092, 2008.

[185] F. Buchner, K. Flechtner, Y. Bai, E. Zillner, I. Kellner, H.-P. Steinrück, H. Marbach, and J. M. Gottfried. Coordination of iron atoms by tetraphenylporphyrin monolayers and multilayers on Ag (111) and formation of iron-tetraphenylporphyrin. *The Journal of Physical Chemistry C*, 112(39):15458–15465, 2008.

[186] J. V. Barth. Fresh perspectives for surface coordination chemistry. *Surface Science*, 603(10):1533–1541, 2009.

[187] R. Wilson and S. Chiang. Registration and nucleation of the Ag/Si(111)-$\sqrt{3} \times \sqrt{3}$ R30° structure by scanning tunneling microscopy. *Physical Review Letters*, 59(20):2329, 1987.

[188] E. van Loenen, J. Demuth, R. Tromp, and R. Hamers. Local electron states and surface geometry of Si(111)-$\sqrt{3} \times \sqrt{3}$ Ag. *Physical Review Letters*, 58:373–376, 1987.

[189] T. Takahashi and S. Nakatani. Refinement of the Si(111)$\sqrt{3} \times \sqrt{3}$-Ag structure by surface X-ray diffraction. *Surface Science*, 282(1-2):17–32, 1993.

[190] M. Upward, P. Beton, and P. Moriarty. Adsorption of cobalt phthalo-cyanine on Ag terminated Si(111). *Surface Science*, 441(1):21 – 25, 1999.

[191] P. Guaino, A. Cafolla, D. Carty, G. Sheerin, and G. Hughes. An STM investigation of the interaction and ordering of pentacene molecules on the Ag/Si(111)-$\sqrt{3} \times \sqrt{3}$ R30° surface. *Surface science*, 540(1):107–116, 2003.

[192] W. Auwärter, A. Weber-Bargioni, A. Riemann, A. Schiffrin, O. Gröning, R. Fasel, and J. Barth. Self-assembly and conformation of tetrapyridyl-porphyrin molecules on Ag(111). *Journal of Chemical Physics*, 124(19):194708–194708, 2006.

[193] W. Wang, Y. Ji, H. Zhang, A. Zhao, B. Wang, J. Yang, and J. G. Hou. Negative differential resistance in a hybrid silicon-molecular sys-

tem: Resonance between the intrinsic surface-states and the molecular orbital. *ACS Nano*, 6(8):7066–7076, 2012.

[194] F. Buchner, I. Kellner, W. Hieringer, A. Gorling, H.-P. Steinruck, and H. Marbach. Ordering aspects and intramolecular conformation of tetraphenylporphyrins on Ag(111). *Phys. Chem. Chem. Phys.*, 12:13082–13090, 2010.

[195] J. Beggan, S. Krasnikov, N. Sergeeva, M. Senge, and A. Cafolla. Control of the axial coordination of a surface-confined manganese (III) porphyrin complex. *Nanotechnology*, 23(23):235606, 2012.

[196] W. Auwärter, K. Seufert, F. Klappenberger, J. Reichert, A. Weber-Bargioni, A. Verdini, D. Cvetko, M. DellAngela, L. Floreano, A. Cossaro, et al. Site-specific electronic and geometric interface structure of Co-tetraphenyl-porphyrin layers on Ag (111). *Physical Review B*, 81(24):245403, 2010.

[197] K. Comanici, F. Buchner, K. Flechtner, T. Lukasczyk, J. M. Gottfried, H.-P. Steinrück, and H. Marbach. Understanding the contrast mechanism in scanning tunneling microscopy (STM) images of an intermixed tetraphenylporphyrin layer on Ag(111). *Langmuir*, 24(5):1897–1901, 2008.

[198] L. Scudiero, D. E. Barlow, and K. Hipps. Physical properties and metal ion specific scanning tunneling microscopy images of metal (II) tetraphenylporphyrins deposited from vapor onto gold (111). *The Journal of Physical Chemistry B*, 104(50):11899–11905, 2000.

[199] M.-S. Liao and S. Scheiner. Electronic structure and bonding in metal porphyrins, metal=Fe, Co, Ni, Cu, Zn. *Journal of Chemical Physics*, 117:205, 2002.

[200] S. A. Krasnikov, A. B. Preobrajenski, N. N. Sergeeva, M. M. Brzhezinskaya, M. A. Nesterov, A. A. Cafolla, M. O. Senge, and A. S. Vinogradov. Electronic structure of Ni(II) porphyrins and phthalocyanine studied by soft X-ray absorption spectroscopy. *Chemical Physics*, 332:318–324, February 2007.

[201] S. A. Krasnikov, N. N. Sergeeva, M. M. Brzhezinskaya, A. B. Preobrajenski, Y. N. Sergeeva, N. A. Vinogradov, A. A. Cafolla, M. O. Senge, and A. S. Vinogradov. An X-ray absorption and photoemission study of the electronic structure of Ni porphyrins and Ni N-confused porphyrin. *Journal of Physics: Condensed Matter*, 20(23):235207, 2008.

[202] M. Cuberes, R. Schlittler, and J. Gimzewski. Manipulation of C_{60} molecules on Cu(111) surfaces using a scanning tunneling microscope. *Applied Physics A: Materials Science & Processing*, 66:S669–S673, 1998.

[203] H. Tang, M. Cuberes, C. Joachim, and J. Gimzewski. Fundamental considerations in the manipulation of a single C_{60} molecule on a surface with an STM. *Surface Science*, 386(1):115–123, 1997.

[204] T. Yokoyama, S. Yokoyama, T. Kamikado, and S. Mashiko. Nonplanar adsorption and orientational ordering of porphyrin molecules on Au(111). *The Journal of Chemical Physics*, 115:3814, 2001.

[205] M. P. de Jong, R. Friedlein, S. Sorensen, G. Öhrwall, W. Osikowicz, C. Tengsted, S. Jönsson, M. Fahlman, and W. R. Salaneck. Orbital-specific dynamic charge transfer from Fe(II)-tetraphenylporphyrin molecules to molybdenum disulfide substrates. *Physical Review B*, 72(3):035448, 2005.

[206] K. M. Kadish, K. M. Smith, and R. Guilard. *The Porphyrin Handbook, Applications: Past, Present and Future*, volume 6. San Diego, CA: Academic, 2000.

[207] W. Liu and J. T. Groves. Manganese porphyrins catalyze selective C–H bond halogenations. *Journal of the American Chemical Society*, 132(37):12847–12849, 2010.

[208] J. T. Groves. Reactivity and mechanisms of metalloporphyrin-catalyzed oxidations. *Journal of Porphyrins and Phthalocyanines*, 4(4):350–352, 2000.

[209] J. T. Groves and T. E. Nemo. Epoxidation reactions catalyzed by iron porphyrins. Oxygen transfer from iodosylbenzene. *Journal of the American Chemical Society*, 105(18):5786–5791, 1983.

[210] B. Meunier. Metalloporphyrins as versatile catalysts for oxidation reactions and oxidative DNA cleavage. *Chemical Reviews*, 92(6):1411–1456, 1992.

[211] B. Hulsken, R. V. Hameren, J. W. Gerritsen, T. Khoury, P. Thordarson, M. J. Crossley, A. E. Rowan, R. J. Nolte, J. A. Elemans, and

S. Speller. Real-time single-molecule imaging of oxidation catalysis at a liquid–solid interface. *Nature Nanotechnology*, 2(5):285–289, 2007.

[212] A. D. Adler, F. R. Longo, F. Kampas, and J. Kim. On the preparation of metalloporphyrins. *Journal of Inorganic and Nuclear Chemistry*, 32(7):2443–2445, 1970.

[213] P. R. O. de Montellano. *Cytochrome P450: structure, mechanism, and biochemistry*. Springer, 2005.

[214] M. C. Feiters, A. E. Rowan, and R. J. Nolte. From simple to supramolecular cytochrome P450 mimics. *Chemical Society Reviews*, 29(6):375–384, 2000.

[215] B. Hulsken, R. V. Hameren, P. Thordarson, J. W. Gerritsen, R. J. Nolte, A. E. Rowan, M. J. Crossley, J. Elemans, and S. Speller. Scanning tunneling microscopy and spectroscopy studies of porphyrins at solid-liquid interfaces. *Japanese Journal of Applied Physics*, 45(3B):1953, 2006.

[216] M. Parschau, D. Passerone, K.-H. Rieder, H. Hug, and K.-H. Ernst. Switching the chirality of single adsorbate complexes. *Angewandte Chemie International Edition*, 48(22):4065–4068, 2009.

[217] R. Fasel, M. Parschau, and K.-H. Ernst. Amplification of chirality in two-dimensional enantiomorphous lattices. *Nature*, 439(7075):449–452, 2006.

[218] K.-H. Ernst. Supramolecular surface chirality. In *Supramolecular Chirality*, pages 209–252. Springer, 2006.

[219] W. B. Jennings, B. M. Farrell, and J. F. Malone. Attractive intramolecular edge-to-face aromatic interactions in flexible organic molecules. *Accounts of Chemical Research*, 34(11):885–894, 2001.

[220] J. Brede, M. Linares, S. Kuck, J. Schwoebel, A. Scarfato, S.-H. Chang, G. Hoffmann, R. Wiesendanger, R. Lensen, P. H. Kouwer, et al. Dynamics of molecular self-ordering in tetraphenyl porphyrin monolayers on metallic substrates. *Nanotechnology*, 20(27):275602, 2009.

[221] E. A. Meyer, R. K. Castellano, and F. Diederich. Interactions with aromatic rings in chemical and biological recognition. *Angewandte Chemie International Edition*, 42(11):1210–1250, 2003.

[222] S. Burley and G. Petsko. Aromatic-aromatic interaction: a mechanism of protein structure stabilization. *Science*, 229(4708):23–28, 1985.

[223] A. Rosa, G. Ricciardi, and E. J. Baerends. Synergism of porphyrin-core saddling and twisting of meso-aryl substituents. *The Journal of Physical Chemistry A*, 110(15):5180–5190, 2006.

[224] V. Iancu, A. Deshpande, and S.-W. Hla. Manipulating Kondo temperature via single molecule switching. *Nano Letters*, 6(4):820–823, 2006.

[225] R. Gupta and S. Sen. Calculation of multiplet structure of core p-vacancy levels. II. *Physical Review B*, 12(1):15, 1975.

[226] J.-S. Kang, G. Kim, H. Lee, D. Kim, H. Kim, J. Shim, S. Lee, H. Lee, J.-Y. Kim, B. Kim, et al. Soft X-ray absorption spectroscopy and magnetic circular dichroism study of the valence and spin states in spinel $MnFe_2O_4$. *Physical Review B*, 77(3):035121, 2008.

[227] H. Nesbitt and D. Banerjee. Interpretation of XPS Mn (2p) spectra of Mn oxyhydroxides and constraints on the mechanism of MnO_2 precipitation. *American Mineralogist*, 83(3):305–315, 1998.

[228] D. den Boer, M. Li, T. Habets, P. Iavicoli, A. E. Rowan, R. J. Nolte, S. Speller, D. B. Amabilino, S. D. Feyter, and J. A. Elemans. Detection of different oxidation states of individual manganese porphyrins during their reaction with oxygen at a solid/liquid interface. *Nature Chemistry*, 5(7):621–627, 2013.

[229] M. Momenteau, B. Loock, C. Tetreau, D. Lavalette, A. Croisy, C. Schaeffer, C. Huel, and J.-M. Lhoste. Synthesis and characterization of a new series of iron (II) single-face hindered porphyrins. Influence of central steric hindrance upon carbon monoxide and oxygen binding. *J. Chem. Soc., Perkin Trans. 2*, (2):249–257, 1987.

[230] F. Sedona, M. Di Marino, M. Sambi, T. Carofiglio, E. Lubian, M. Casarin, and E. Tondello. Fullerene/porphyrin multicomponent nanostructures on Ag(110): From supramolecular self-assembly to extended copolymers. *ACS Nano*, 4(9):5147–5154, 2010.

[231] S. Yoshimoto, S. Sugawara, and K. Itaya. Effect of underlying Ni(II) porphyrin adlayer on the formation of supramolecular assembly of

fullerenes on Au(111) in solution. *Electrochemistry Tokyo*, 74(2):175, 2006.

[232] S. Vijayaraghavan, D. Ecija, W. Auwarter, S. Joshi, K. Seufert, A. P. Seitsonen, K. Tashiro, and J. V. Barth. Selective supramolecular fullerene–porphyrin interactions and switching in surface-confined C_{60}–$Ce(TPP)_2$ Dyads. *Nano Letters*, 12(8):4077–4083, 2012.